

AVERAGE RESONANCE CAPTURE IN
COBALT AND MANGANESE USING
 B^{10} FILTER TECHNIQUE

AVERAGE RESONANCE CAPTURE IN
COBALT AND MANGANESE USING
 B^{10} FILTER TECHNIQUE

by

Armando Macaraeg Lopez B.Ap.Sc.

A Thesis

Submitted to the Faculty of Graduate Studies
in Partial Fulfilment of the Requirements

for the Degree
Doctor of Philosophy

McMaster University

May, 1973

Doctor of Philosophy (1973)

McMaster University
Hamilton, Ontario

Title: Average Resonance Capture in Cobalt and Manganese
Using B^{10} Filter Technique

Author: Armando Macaraeg Lopez

B.Ap.Sc. (Eng. Sci.) University of Toronto

Supervisor: Dr. W. V. Prestwich

No. of Pages: 155

Scope and Contents:

The high energy gamma rays from the radiative capture of B^{10} filtered neutrons in Mn^{55} and Co^{59} were measured and analyzed in terms of the statistical and direct capture model of nuclear reactions. A high resolution NaI(Tl)-Ge(Li) pair spectrometer was used to detect the gamma rays. Correlations between (n, γ) and (d,p) intensities were determined for these nuclei. The distributions of the reduced intensities were also studied and compared with the predictions of the statistical model. Finally an attempt was made to determine a direct capture component in the Co^{60} ground state partial cross-section. It was found that the ground state data could be explained with the resonance amplitudes alone. The following amplitudes were deduced: $\Gamma_{132}^{\frac{1}{2}} = +0.109 \pm .001 \text{ eV}^{\frac{1}{2}}$; $\Gamma_{4322}^{\frac{1}{2}} = +0.293 \pm .017 \text{ eV}^{\frac{1}{2}}$; $\Gamma_{10700}^{\frac{1}{2}} = +0.232 \pm .020 \text{ eV}^{\frac{1}{2}}$; $\Gamma_{16920}^{\frac{1}{2}} = -.001 \pm .010 \text{ eV}^{\frac{1}{2}}$.

TABLE OF CONTENTS

	<u>Page</u>
Chapter I - Introduction	
1. General Background	1
2. Research Motivation	6
Chapter II - Relevant Nuclear Theories	
1. Introduction	12
2. Bohr Compound Nucleus Reaction Theory	12
3. Lane and Lynn Theory	17
4. Correlation of (n, γ) and (d,p) Strengths	21
Chapter III - B ¹⁰ Filter Resonance Capture Method	
1. Introduction	25
2. Basis of the B ¹⁰ Filter Resonance Technique	26
a. Neutron Spectrum	26
b. Effect of B ¹⁰ as a Neutron Filter	27
i. Simplified Picture of the Filter	27
ii. Actual Captured Neutron Spectrum	29
iii. Effect of Multiple Scattering	32
Chapter IV - Instrumentation	
1. Neutron Source	37
2. Tangential Through-Tube Irradiation Facility	38
A. General Considerations	38
B. Through-Tube Design #1	42
C. Through-Tube Design #2	45
D. Through-Tube Design #3	47

	<u>Page</u>
3. Detecting System	
A. Introduction	51
B. Ge(Li) Detector	53
C. NaI(Tl)-Ge(Li) Pair Spectrometer	56
D. Electronic System	58
E. Experimental Procedure	67
Chapter V - Data Analysis	70
1. Determination of Gamma Ray Energy	
A. Method 1 - Gaussian Fit	71
B. Method 2	72
C. Method 3	72
2. Determination of Gamma Ray Intensity	73
3. Determination of Centroid Shift	76
Chapter VI - Experimental Data	
1. Experimental Conditions	83
2. Experimental Results	86
Chapter VII - Discussion of Results	
1. Background Information	104
2. Flux Model Calculation and Measured Activity	111
3. Statistical and Nuclear Structure Effects	111
4. Resonance Partial Widths and Direct Amplitude	120
Appendix 1 - E1 Transitions in Direct Capture and (d,p) Strengths	138
Appendix 2 - Correction for Multiple Scattering Using Response	143

	<u>Page</u>
Appendix 3 - Dependence of Error in Centroid Calculation on Resolution and Background Spectrums	145
Appendix 4 - Effective Degree of Freedom	147
References	152

Summary of Tables

<u>No.</u>	<u>Title</u>	<u>Page</u>
3.1	Summary of Definitions of Parameters Used in Geometrical Calculations	31
3.2	Fractional Contribution - Co.	33
3.3	Fractional Contribution - Mn.	34
3.4	Fractional Contribution of Co Resonances Including Scattering	36
6.1	Cobalt Sample - Experimental Conditions	84
6.2	Manganese - Experimental Conditions	85
6.3	High Energy Gamma Rays from $\text{Co}^{59}(n,\gamma)\text{Co}^{60}$	87
6.4	Observed Intensities of Transitions in the $\text{Co}^{59}(n,\gamma)\text{Co}^{60}$	89
6.5	Observed High Energy Gamma Rays in $\text{Mn}^{55}(n,\gamma)\text{Mn}^{56}$	92
6.6	Measured Intensities of Gamma Rays in $\text{Mn}^{55}(n,\gamma)\text{Mn}^{56}$	94
6.7	Peak Centroid Shifts in Cobalt Gamma Rays	98
6.8	Peak Centroid Shift in Manganese Lines	99
6.9	Nitrogen Calibration Lines	100
6.10	Activity of Co Samples	103
7.1	Final State Spin Assignments in Co^{60}	106
7.2	Spin and Parity - Low-lying Levels in Mn^{56}	108
7.3	Measured Activity of Cobalt Samples	112
7.4	Effective Degree of Freedom for Co^{60}	116
7.5	Statistical Properties Deduced from the Mn^{56} Lines	121
7.6	Comparison of the Deduced Resonance Parameters with the Time-of-Flight Data	131
7.7	Sensitivity of Best Fit Parameters to Geometrical Considerations	133
7.8	Variation of Cobalt Ground State Line Widths with Filter Thickness	135
7.9	Comparison of the Direct Amplitude with the Contribution of High Energy Resonances at Low Energy	136

FIGURE CAPTIONS

<u>NUMBER</u>	<u>TITLE</u>	<u>FOLLOWING PAGE</u>
3.1	Neutron Spectrum from a Water-Moderated Nuclear Reactor	26
3.2	Neutron Spectrum Obtained after Normal Incidence in a B10 Filter	28
3.3	Schematic Diagram of a Typical Sample Assembly	29
3.4	Neutron Spectrum Obtained with Actual Sample Geometry and Including Multiple Scattering Effects	35
4.1	General Layout of the Nuclear Reactor Facilities	37
4.2	General Arrangement for Through-Tube Design #2	45
4.3	Details of Through-Tube Design #2	45
4.4	Typical Sample Assembly for Through-Tube Design #3	47
4.5	Positioning of Sample Assembly on Through-Tube #3	48
4.6	Final Through-Tube Design #3	51
4.7	Comparison of Aluminum Background Obtained with TT #1 and TT #3	51
4.8	Schematic of the Ge(Li)-NaI Pair Spectrometer	53
4.9	Energy Dependence of the Photoelectric, Compton Effect and Pair Production Cross-Section in Germanium	55
4.10	Overall Schematic of the Detection System	58
4.11a	Schematic of the Single Channel Analyzer Used for Each Annular Quadrant	60
4.11b	Overall Schematic of the Electronic Logic Circuitry	60
4.12	Time Resolution Curve Between Two Opposite Quadrants	62
4.13	Typical Spectrum of the Single Channel Analyzer Window Obtained with Na ²² Source	62
4.14	Block Diagram of the Reference Pulser	64
5.1	Co ⁶⁰ Ground State Line Showing the Curve Obtained with Gaussian Fit (Solid Line)	71
5.2	Fitting a Doublet (line 11c) with Gaussian Curve	71

<u>NUMBER</u>	<u>TITLE</u>	<u>FOLLOWING PAGE</u>
5.3	Relative Efficiency Curve	77
5.4	Average Shift of Nitrogen Lines Obtained by Method of Cross-Correlation	78
5.5	Change in Gain and Zero as a Function of Time	79
5.6	Dependence of Gain and Zero Change with Count Rate	80
6.1 - 6.4	Co ⁶⁰ Spectra Obtained with Different Filter Thicknesses	86
6.5 - 6.8	Mn ⁵⁶ Spectra Obtained with Different Filter Thicknesses	86
6.9	Nitrogen Calibration Spectrum	97
6.10	Relative Efficiency Curve	97
7.1	Integral Probability Distribution of the Reduced Intensities of the Cobalt Lines	119
7.2	Integral Probability Distribution of the Reduced Intensities of the Mn ⁵⁶ Lines	120
7.3	Relative Intensity Variation of the Cobalt Doublet Lines #3, 4 with Filter Thickness	123
7.4	Intensity and Centroid Shift - Co ⁶⁰ Ground State Line	134
7.5	Comparison of the ratio $R = \sigma_{\text{int}} / \sigma_{\text{int}}$ Using the Best Fit Parameters with the Results of Wasson (Wa 68) and Auchampaugh (Au 68)	134

ACKNOWLEDGEMENTS

I would like to express my sincere thanks to my Research Director, Dr. W. V. Prestwich whose guidance, inspiration and invaluable assistance made the completion of this work doubly easier. The stimulating and instructive discussions with him have been a great factor in the understanding of difficult problems and the eventual generation of techniques used in their solution.

I would also like to thank the members of my Supervisory Committee, Dr. T. J. Kennett and Dr. K. Fritze for their help and guidance during the course of this research.

I appreciate very much the assistance of Mr. Andrew Robertson. I am indebted to him for his help during the experiment and during the data analysis. I also want to acknowledge the assistance of Mr. L. Lowe, Dr. H. Zamora and Mr. N. Ramanathan.

I would like to express my gratitude to the Reactor staff, in particular to Mr. K. Marshall and Mr. Frank Horvath of the Health Physics group.

I am grateful to my brother, Mario who prepared the excellent diagrams in this thesis.

The difficult and laborious task of typing the manuscript was accepted by Mrs. W. V. Prestwich. My appreciation goes to her efforts not only in pursuing this hard work, but also in preparing the "Saturday noon special" during which

Important matters were discussed can only exceed my capacity
for words.

3
Last, but not least, I would like to thank my wife
Elsie for her moral support during the course of this
study. I also appreciate her help in the preparation
of this manuscript.

CHAPTER I

INTRODUCTION

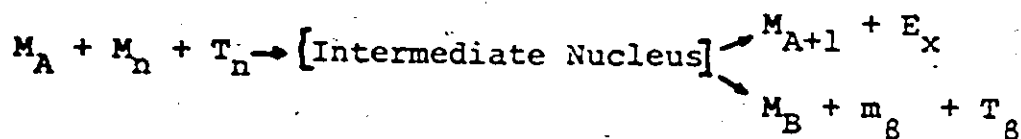
1. General Background

The study of the radiative capture of neutrons has always been an important part of nuclear physics. The results of the investigation of neutron capture gamma rays have contributed to our knowledge of various observable properties of the nucleus resulting in some understanding of the complexity of the nuclear structure. It has also led to some important concepts in nuclear reaction mechanisms, a subject which needs to be understood in order to be able to make an intelligent interpretation of the physical observables.

The use of the neutron as a projectile to probe the nucleus has the advantage that significant interaction rates occur even at a very low bombarding energy. This is due to the absence of a Coulomb barrier which hinders a charged particle in entering the internal region of a nucleus.

A nuclear reaction is typically represented by $A(\alpha, \beta)B$. A is the target nucleus, α is the incident particle, B is the residual nucleus and β is the particle which is emitted after the interaction with the incident projectile. In the case of neutron capture, α is represented by a neutron. Thus a neutron is captured resulting in a highly excited

intermediate nucleus. This highly excited nucleus then deexcites either by emitting a gamma ray or by emitting another particle such as a neutron or a proton. More explicitly, this can be written as



where M_A , M_n , M_{A+1} , M_B , m_β represent the masses of the target nucleus, the neutron, the residual nucleus formed if de-excitation occurs by gamma ray emission, the residual nucleus formed if a particle with mass m_β is emitted. The kinetic energy of the incident neutron and the emitted particle are T_n and T_β respectively, while E_x is the excitation energy that will be given off in the form of gamma radiation and nuclear recoil.

In the case of a radiative transition, the neutron separation energy is equal to $S_n = M_A + M_n - M_{A+1}$. From the previous equations $E_x = S_n + T_n$. In thermal capture $T_n = 0.025$ eV while S_n ranges from 2.227 MeV for the deuteron to 11.45 MeV for boron-11 with most values around 8 MeV. Therefore in thermal capture the excitation energy is approximately equal to the neutron separation energy.

The deexcitation process may involve the emission of a single gamma ray or it may result in several gamma rays comprising a particular cascade to the ground state. For a single gamma ray transition to the ground state

$$E_x = E_\gamma + \frac{E_\gamma^2}{2M_{A+1}c^2}$$

where E_γ is the gamma ray energy. The second term is the nuclear recoil energy necessary in order to conserve momentum during the emission process and c is the speed of light.

For a particular reaction induced by a flux of incident particles the cross-section is defined as

$$\sigma = \frac{\text{no. of particular events per unit time per nucleus}}{\text{no. of incoming particles passing through unit area normal to the beam direction per unit time.}}$$

It is related to the probability with which a given reaction will occur.

It has been observed that the total neutron capture cross-section exhibits fluctuations. In the low energy region these fluctuations take the form of narrow peaks at particular energies which are not uniformly spaced. These are called resonances. (Mo 36, Ra 36)

The widths and spacings of these peaks vary from mass number to mass number. In medium weight nuclei the resonance widths are of the order of electron volts to a few keV and the spacings are of the order of 5-10 keV. In heavier nuclei these spacings are substantially reduced and are of the order of eV. Generally speaking the number of resonances per unit energy increases with mass number and excitation and in the resonance region the width Γ is less than the level spacing D .

For a given nuclide the resonance width tends to increase with neutron energy. Eventually these widths become comparable with the spacing. At very high energies the widths become greater than the spacing so that overlapping occurs. In this continuum region the fine structure of the resonances is dissolved. The total cross-section exhibits broad maxima whose position depends smoothly on mass number.

For isolated resonances the total cross-section for the interaction of s-wave neutrons (i.e. with angular momentum relative to the target nucleus = 0) with non-fissionable nuclei is adequately fitted to the form.

$$\sigma_T = 4\pi R^2 + \frac{\sigma_0}{1+X^2} \left[\frac{\Gamma_n}{\Gamma} + \frac{2RX}{\lambda_0} \right] + \frac{\sigma_0}{1+X^2} \frac{\Gamma_Y}{\Gamma} \sqrt{\frac{E_0}{E}}$$

where

- Γ = full width at half maximum of resonance
- Γ_Y = partial radiative width
- Γ_n = partial neutron width
- R = effective radius of the target nucleus for neutrons
- λ_0 = de Broglie wavelength of the neutron at the resonance energy
- E_0 = resonance energy
- $\sigma_0 = 4\pi\lambda_0^2 g \frac{\Gamma_n}{\Gamma}$
- $X = 2(E-E_0)/\Gamma$
- $g = \frac{2J+1}{2(2I+1)}$ = spin statistical factor
- I = spin of target nucleus
- J = spin of the resonance

The first term is the potential scattering cross-section. The second term is the resonance scattering term which includes the interference between the resonance and potential scattering and the third term is the resonance capture cross-section. This equation is known as the Breit-Wigner formula.

The probability amplitude corresponding to the Breit-Wigner formula can be derived by taking the Fourier transform of an exponentially decaying state. Therefore a physical interpretation of the resonance behaviour at a given neutron energy may be associated with the formation of a long-lived state of the compound system comprised of the incident neutron and the target. The lifetime of this quasi-stationary state which decays by particle or gamma ray emission is related to the resonance width by means of the uncertainty principle $\Gamma\tau = \hbar$. Hence a virtual state 1 eV wide would have a mean life $\tau = 10^{-15}$ secs. This is very long compared to the nuclear transit time of 10^{-21} secs.

Where more than one resonance contributes significantly to the total cross-section two other terms have to be included. The first term is due to the interference between resonances in neutron scattering. This is given by the expression

$$\sigma_n(\text{int}) = \sum_{i \neq j} \theta_{nij}^2 \left[\sigma_{oi} \sigma_{oj} \frac{\Gamma_{ni}}{\Gamma_i} \frac{\Gamma_{nj}}{\Gamma_j} \right]^{\frac{1}{2}} \frac{1 + X_i X_j}{(1 + X_i^2)(1 + X_j^2)}$$

The sum is over all pairs of the same spin and θ_{nij} is the phase factor between the probability amplitudes of the i^{th} and j^{th} resonance. Because the elastic scattering entrance and exit channels are the same there are no random fluctuations in sign of the interference terms. The second interference is obtained in the radiative capture cross-section and is of the form (Vo 58, Ca 62)

$$\left[\sigma_{oi} \sigma_{oj} \sqrt{\frac{E_{oi} E_{oj}}{E}} \right]^{\frac{1}{2}} \frac{1 + X_i X_j}{(1 + X_i^2)(1 + X_j^2)} \left[\frac{\Gamma_{\gamma ki}}{\Gamma_i} \frac{\Gamma_{\gamma kj}}{\Gamma_j} \right]^{\frac{1}{2}}$$

where $\Gamma_{\gamma ki}$ is the partial radiative width of the transition from the i^{th} resonance to the k^{th} final state of the compound nucleus. Since the entrance and the exit channels are distinct in the radiative capture process the sign of the interference terms between resonances will fluctuate randomly. Therefore if enough resonances are included this term may be negligible. However if only a few resonances contribute this term may be significant, causing anomalously weak or strong transitions depending on whether the interference is destructive or constructive.

2. Research Motivation

As a result of the availability of a high neutron flux from nuclear reactors, extensive studies have been made on the thermal neutron capture spectra of several elements. From these experimental data three different kinds of

Information have been deduced namely, (1) the energies, spins and parities of the initial states, (2) the energies, spins and parities of the low-lying levels and (3) the mechanism of the radiative capture process.

The main interest in this research is to obtain more insight into the nuclear reaction mechanism in the radiative capture of slow neutrons. Presently there are two extremes of nuclear reaction models - the compound nucleus model and the direct reaction model. In the former a neutron is captured and forms a highly excited compound state. There is an intermediate sharing of the available energy by all the nucleons and then by purely statistical processes a neutron may acquire sufficient energy to be emitted. A competing mode of decay is the gamma radiation process. The total probability of decay of the capture state is $\frac{\Gamma}{\hbar} = \frac{\Gamma_n}{\hbar} + \frac{\Gamma_\gamma}{\hbar}$ where Γ is the total width, Γ_n is the neutron width and Γ_γ is the gamma ray width.

In the direct capture model similar deexcitation modes compete following neutron capture, however no intermediate compound nucleus is formed. The available energy is not shared by all the nucleons so that the probability of decay is not a statistical process but may depend on the nuclear structure. Theoretically the two mechanisms can be distinguished from each other by the characteristic reaction times. In the compound nucleus theory the reaction time is of the order of 10^{-14} secs compared to 10^{-22} secs in the direct capture model.

The experimental observations indicate that both compound nucleus and direct reactions occur in the radiative capture process at low energies. The available data that is used to support these observations are as follows.

For the compound nucleus the two most convincing observations are: (1) according to this model when a compound state of excitation E_x decays by photon emission the spectrum of primary E1 gamma rays is distributed as $E_\gamma^3 \rho(E_x - E_\gamma)$ where E_γ is the photon energy and $\rho(E_x - E_\gamma)$ is the level density of the residual nucleus with excitation energy equal to $E_x - E_\gamma$. This theoretical spectrum has a broad maximum around 2-3 MeV and then falls off at higher energies. Most data agree with this prediction and in fact there seems to be complete agreement at the low energy. (2) a consequence of this model is that the partial neutron and the partial gamma ray widths should be distributed according to a Porter-Thomas distribution. Again good agreement with experimental data has been observed for most nuclides. (Po 56)

The suggestion for a direct component has been based on observed discrepancies in some cases with the predictions of the compound nucleus theory. For some targets the photon distributions show an increase in intensity at high energies in contradiction to (1). These strong transitions at high energies are often referred to as "anomalous bumps". The transition strengths for these gamma rays appear to be correlated with the structure of the final state. Furthermore the occurrence of the "anomalous bumps" seems to depend on mass

number. Such dependences cannot be favored in the statistical model but could be due to the non-statistical effects of the nuclear structure. (Gr 58, Ba 53)

Several theories have been put forward to explain these observations. Presently the most rigorous one which is based on the formalism of the R-matrix theory is the Lane and Lynn theory. Accordingly the direct component arises from the contribution to the dipole integral from the "channel region". Physically this contribution comes from the transition of an incident s-wave neutron to a p-wave neutron orbital resulting in an E1 transition without forming a compound nucleus. (La 60)

The experimental data used to compare with the Lane and Lynn theory have been obtained mainly from thermal neutron capture. Unfortunately, these data do not represent a good average of the partial widths for two reasons, first the broad Porter-Thomas fluctuation which governs the partial widths and secondly interference between contributing resonances of the same spin.

A different approach, using a B^{10} filter to shape the incident neutron flux from a nuclear reactor is employed to investigate the extent of nuclear structure effects on radiative capture of slow neutrons. The elements being studied are cobalt and manganese. They are selected because they lie in the region where the s-wave neutron strength is maximum and the low lying levels are expected to contain a large component

of p-wave configuration. It is expected that in this region the nuclear structure effect should be most significant. The Lane and Lynn theory predicts a direct capture cross-section of the order of 12 mb at 1 eV.

Several studies in cobalt have been done previously. From the thermal neutron capture spectrum Prestwich et al (Pr 66) deduced that the average reduced intensity of gamma ray transitions, $\langle \Gamma / E^3 \rangle$ leading to final states which exhibit an $l_n = 1$ stripping pattern is five times more intense than for those transitions leading to final states for which an $l_n = 3$ stripping pattern is observed, a dependence expected from single particle effects. In another experiment, however involving individual resonance capture, Prestwich and Cote (Pr 67) were unable to obtain any significant correlation with the (d,p) strengths. The explanation is that the correlation between the radiative and the (d,p) strength is destroyed when the initial spin states do not contribute equally. The filter technique employed here tends to equalize the contributions of these initial states and therefore theoretically a significant correlation is expected.

Evidence was presented by Wasson et al (Wa 68) and Auchampaugh (Au 68) on the direct capture component of the ground state partial capture cross-section. The former quoted a direct capture cross-section of 9 mb while the latter 5.5 mb. Other relatively strong transitions were also investigated but no direct capture component could be detected.

In manganese Prestwich and Cote (Pr 57) observed positive correlation between the (n, γ) strength and the (d, p) strength even for the individual resonance capture results. When these spectra were averaged a large correlation coefficient, 85% was obtained. Comfort (Co 68) analyzed the $Mn^{55}(n, \gamma)Mn^{56}$ data by taking into account the $j-j$ coupling in the direct capture model of Bockelman (Bo 59). According to this treatment the ratio of (n, γ) to (d, p) reduced widths is proportional to $2j_n + 1$ where j_n is the total angular momentum of the neutron. This prediction was observed to be consistent with the measured values however it cannot be tested conclusively because of lack of knowledge of spins of many of the final states. Anchampaugh (Au 68) also tried to extract a direct capture cross-section in 9 strong lines of Mn using the direct-resonance interference method. However he was not able to determine a nonzero value.

In this experiment the primary high energy gamma rays of Co and Mn are analyzed as a function of filter thickness. Correlation between (n, γ) and (d, p) intensities are made. The distribution of the reduced intensities are compared with the expectation based on the statistical theory.

The next chapter is a discussion of the relevant nuclear theories. This is followed by a detailed analysis of the B^{10} filter technique which is also compared with other methods. The instrumentation and experimental procedures is described and is followed by the method of data analysis. Finally the experimental result, the observations and conclusions are presented and are interpreted in the light of the present nuclear theories.

CHAPTER II

RELEVANT NUCLEAR THEORIES

1. Introduction

The purpose of this chapter is to review the nuclear theories which are relevant to the aim of this research. Since detailed formulation of these theories are available from the literature, (La 60, Ly 68, Co 68), the treatment given is brief and simplified.

2. Bohr Compound Nucleus Reaction Theory

The earliest theory of nuclear reactions was formulated by Bethe (Be-35) who assumed that the incident projectile moved in an attractive real potential arising from its interaction with the nucleus. The positive energy levels correspond to the unbound or virtual levels while the bound levels inside the well constitute the negative energy resonances. For example, if one assumes a single square well potential then the s-wave resonances occur when $KR = (n + 1/2)\pi$ where $K^2 = 2\mu(E + V_0)/\hbar^2$, V_0 is the potential depth, E is the kinetic energy of the incident particle, μ is the reduced mass and R is the nuclear radius.

A consequence of the single particle model of nuclear reactions is that the level spacings are in the MeV range, in contradiction to the small spacings deduced from experimental data.

To explain the observed slow neutron cross-section Bohr (Bo 36) introduced the compound nucleus model of nuclear reactions. According to this theory the incident particle upon absorption by the nucleus interacts very strongly with the nucleons. The interaction is so strong that the energy of the absorbed neutron is immediately shared by all the nucleons. Thus many particles participate in the compound nucleus formation resulting in a large number of virtual states. Energy exchanges between all the nucleons follow the neutron absorption and then by purely statistical processes at a much later time compared to the nuclear transit time, one of the nucleons may acquire sufficient energy to be emitted. If the energy acquired by one particle is not sufficient for charged particle emission then the virtual state will decay by neutron emission or radiative deexcitation.

Because of the instantaneous participation of many nucleons following neutron capture the mode of decay is independent of the compound nucleus formation. The reaction cross-section can therefore be expressed as

$$\sigma(a,b) = \sigma_c(a)\sigma(b)$$

where $\sigma_c(a)$ represents the probability of forming a compound nucleus by capturing the incident particle a, and $\sigma(b)$ is the probability of decay by the emission of particle b. More generally the letters a and b refer to incident channel and exit channel respectively. A channel can be defined as the system configuration which includes all the particles involved with their respective properties such as spins, parities and angular momenta.

The cross-section for gamma ray emission following neutron capture is given by the Breit-Wigner formula quoted previously. It is related to the initial and final states through the partial width which is more explicitly expressed as $\Gamma_{\gamma if} = 2\pi |\langle f | 0 | i \rangle|^2 \rho_f$ where ρ_f is the density of final states of the system, and 0 may be either an electric or magnetic multipole operator. For E1 transitions which are of prime interest in this investigation, Blatt and Weisskopf, assuming a simple independent particle model, give the following expression (Bl 52)

$$\Gamma(E1) = 0.2A^{2/3} E_\gamma^3 D(E)/D_0$$

where A is the mass number

E_γ is the gamma ray energy

D(E) is the level spacing at energy level E

D_0 is the level spacing obtained from the independent particle model.

The concept of the compound nucleus is very closely associated with the statistical theory of nuclear reactions. In this model the details of the individual nuclear states are ignored. It is assumed that because of the complexity of the wave functions which describe the compound states, a simplified though incomplete description of the nuclear states can be obtained by means of statistical methods.

The statistical model starts by assuming that the nucleus can be represented by a collection of fermions which are in a potential well. This potential well is due to the

average interaction between all the nucleons. A sequence of single particle levels can be found in this well and when the lowest levels are occupied by the fermions the nucleus is in its ground state. At an excitation energy E_x above the ground state the density of levels regardless of spin is given as (Hu 67)

$$\rho(E_x) = \frac{\left[\frac{2}{3} \frac{g_n g_p}{g_n + g_p} \right]^{1/2}}{12} \frac{6^{1/4}}{12} \frac{e^{\frac{\pi^2}{6} g E_x}}{(g E_x)^{5/4}} \quad \text{where}$$

g_n, g_p refer to the average density of the neutron and proton levels respectively and $g = g_n + g_p$. For a particular spin J , the density of states is

$$\rho(J, E_x) = \frac{\sqrt{\pi}}{12} \frac{2(a E_x)^{1/2}}{a^{1/4} E_x^{5/4}} (2J+1) \frac{e^{-J(J+1)/2\sigma^2}}{2\sqrt{2\pi} \sigma^3}$$

where a is a constant and σ is the spin cut off factor which is a function of mass number and the excitation energy.

Therefore if we combine the expressions for the level density and the gamma ray partial width for E1 transitions we get the photon distribution $E_\gamma^3 \rho(E_x - E_\gamma)$ which predicts a spectrum with a broad maximum around 2-3 MeV and falling off at higher energies.

Perhaps the most significant evidence which supports the compound nucleus model of nuclear reactions is the present interpretation of the distribution that governs the partial widths of neutron resonances. In an extensive study of the fluctuation of nuclear reaction widths, Porter and Thomas (Po 56)

analyzed the reduced neutron widths (i.e. Γ_n/\sqrt{E}) of intermediate and heavy nuclei using a statistical procedure based on the method of maximum likelihood. The results show that the data is consistent with a chi-square distribution with one degree of freedom, a distribution of the form $x^{-1/2}e^{-x/2}$ where $x = \Gamma_n^0 / \langle \Gamma_n^0 \rangle$, sometimes called the Porter-Thomas distribution. This observation implies that the reduced width amplitudes for neutron emission from the compound nucleus follow a normal curve with mean equal to 0.

In terms of wavefunctions, the reduced width amplitude $\Gamma_n^{01/2} \propto \langle \psi_{cn} / \psi_n \rangle$ where ψ_{cn} is the wave function representing the state of the compound nucleus and ψ_n is the wave function describing the system comprised of the incident neutron and the target nucleus. According to the compound nucleus theory ψ_{cn} is very complex as a result of the strong nuclear interaction and the various states that make it up are essentially unrelated. If one regards this matrix element to be composed of contributions from many "cells" of the configuration space with each contributing cell independently assuming random sign and magnitude, then by the central limit theorem of statistics the probability distribution of the sum over cells is expected to be Gaussian with zero mean. This leads to the distribution of widths (i.e. the square of the probability amplitudes) as observed by Porter and Thomas.

However there are a few observations which cannot be explained in terms of the compound nucleus reaction theory of Bohr. The distribution of E1 primary gamma rays of some nuclides show some discrepancy with the theoretical result. Although there appears to be agreement at low gamma ray energies, there are numerous elements which exhibit "anomalously" strong high energy transitions. This observation occurs in reactions involving thermal and high energy neutrons. (Gr 58a, Ba 53, Lu 65, Be 62). The occurrence of these strong transitions at higher energies is often called an "anomalous bump".

It has been observed that the occurrence of "this anomalous bump" seems to be a function of mass number being prominent in the regions $40 < A < 70$ and $170 < A < 208$. If one investigates the level structure of these nuclei one finds that the low energy levels contain configurations where large components of the p-wave orbitals are expected. Thus these enhanced high energy E1 transitions seem to be correlated with the p-wave content of the low-lying level configurations. Furthermore some indication of selection rules seem to apply (Sh 56, Ki 54).

3. Lane and Lynn Theory (La 60, Ly 68)

The Lane and Lynn theory of radiative capture in the resonance region attempts to explain the above experimental observations. The "anomalous bumps" and the transitions

which suggest dependence on the nuclear structure arise due to some kind of direct capture mechanism in the radiative capture process at low energies. This direct mechanism is expected to be significant in transitions to final states with large single particle character. In the (n,γ) process the neutron undergoes a transition to a low-lying single particle p-orbital, emitting an electric dipole radiation without forming a compound nucleus.

This theory is derived using the R-matrix formalism. The basic idea is to express the cross-section for this particular reaction in terms of the wave functions which describe the initial and the final configurations.

Assuming a total of A nucleons involved in the nuclear reaction then the configuration space has $3A$ dimensions. This is divided into an interior region and a channel region. In the interior region all the nucleons are in close proximity and are bounded by a channel or interaction radius, r_c . A channel region represents a possible mode of formation (entrance channel) or decay (exit channel) and is physically represented by at least a pair of nuclear systems separated by a distance greater than r_c . A channel description contains all the information necessary to define a particular configuration of the interacting particles such as spins, parities, angular momenta, types of particles and state of excitation.

The cross-section for the radiative capture of a neutron by a target A is given by

$$\sigma_{nAyf} = \frac{\pi}{k^2} \sum_J \frac{2J+1}{(2i_n+1)(2i_A+1)} \sum_{s1} |U_{Yfc}^J|^2$$

where J is the total angular momentum obtained after coupling the intrinsic spins i_n and i_A of the neutron and the target respectively with the relative angular momentum l. The collision function U_{Yfc} relates the transition from the initial wave function to the final wave function and is more explicitly given by

$$U_{Yfc}^J = \left(\frac{16\pi}{9h} \right)^{1/2} k_Y^{3/2} \langle \psi_f || H^{(1)} || \psi_{EJ} \rangle$$

where k_Y is the photon wave number, ψ_f is the final wave function, ψ_{EJ} is the entrance channel wave function, $H^{(1)}$ is the dipole operator and k is the neutron wave number.

By considering the proper exit channel wave function and the contribution of the entrance channel in the interior and exterior regions of the configuration space Lynn and Lane showed that the collision function can be written as a sum of three parts namely:

$$U_{Yfc}^J(\text{total}) = U_{Yfc}^J(\text{direct}) + U_{Yfc}^J(\text{ch-res}) + U_{Yfc}^J(\text{int-res})$$

The first term $U_{Yfc}^J(\text{direct})$ describes the process by which an incident s-wave neutron makes a transition from an s-state

to a p-state accompanied by the emission of an E1 gamma ray without forming a compound nucleus. It also contains the effect of potential scattering. The terms $U_{\gamma fc}^J$ (ch res) and $U_{\gamma fc}^J$ (int res) are both resonance terms whose effects are indistinguishable. However where a large channel contribution is present a correlation between the partial width $\Gamma_{\lambda \gamma f}$ and the reduced neutron amplitude $\theta_{\lambda c}$ will be observed. Since the direct amplitude has a non-resonant behaviour its contribution may be observed by the dependence of the transition strengths to certain final states. Qualitatively then, the results of the above formalism can explain the experimental observation of the "anomalous bump" or the transitions which suggest final state dependence.

Further consideration of the matrix elements for a dipole operator yields the following conclusions (Au 68)

- $U_{\gamma fc}^J$ (direct) is negative and purely imaginary
- As long as $k\gamma_c \ll k_f\gamma_c$, $U_{\gamma fc}^J$ (ch. res) is negative and purely imaginary
- $U_{\gamma fc}^J$ (int-res) is imaginary and may be either positive or negative.

These observations imply that the collision function can be rewritten more conveniently in the following form

$$U_{\gamma fc}^J = -i \left\{ D_{c_f}^J + \sum_{\lambda} \frac{\Gamma_{\lambda c}^{1/2}}{E_{\lambda} - E - \frac{-i\Gamma_{\lambda}}{2}} \left[\Gamma_{\lambda \gamma f}^{1/2}(\text{ch}) + \Gamma_{\lambda \gamma f}^{1/2}(\text{int}) \right] \right\}$$

If this expression is substituted in the expression for the partial cross-section the result is

$$\sigma_{n\gamma f} = \pi\lambda^2 \sum_J \frac{2J+1}{2(2I+1)} \left| D_{cf}^{J\sim} + \sum_{\lambda} \frac{\Gamma_{\lambda n}^{1/2} \Gamma_{\lambda\gamma f}^{1/2}}{E_{\lambda} - E - i\Gamma_{\lambda/2}} \right|^2$$

where the channel and interior resonance amplitudes are combined to $\Gamma_{\lambda\gamma f}^{1/2}$ and where s-wave neutron capture by a target nucleus of spin I is also assumed.

4. Correlation of (n, γ) and (d,p) Strengths

The reaction $A(d,p)B$ is another process by which a neutron is captured by the target nucleus. Thus the residual nuclei in the (n, γ) and (d,p) reaction are identical. However the (d,p) reaction mechanism is strictly a direct process and is characterized by short reaction times and a forward peaked distribution of the reaction products.

The picture associated with deuteron stripping is that a neutron is transferred into a shell-model orbital of the target nucleus. Ignoring spin factors the transition probability is given by (Co 68a)

$$T = J \int d\vec{r}_p \frac{d\vec{R}}{d\vec{r}_n} \psi_p^{(-)*} \langle \psi_{J_f M_f} | V_{np} | \psi_{d_n} \psi_{J_i M_i} \rangle \psi_d^{(+)}$$

where J = Jacobian of the transformation from the neutron and proton coordinates \vec{r}_n, \vec{r}_p to \vec{R}, \vec{r}_p .

$\psi_{J_f M_f}$ = final state wave function

$\psi_{d,m}$ = deuteron wave function

$\psi_{J_i M_i}$ = initial state wave function of target nucleus

V_{np} = neutron-proton interaction in deuteron

$\psi_p^{(-)}$, $\psi_d^{(+)}$ = deuteron scattering wave functions

The final state wave function is now expanded into the initial wave functions yielding a theoretical expression for the differential cross-section. Because the assumption of the neutron going into a shell-model state is not strictly true in general the experimental differential cross-section can be written as $\left(\frac{d\sigma}{d\omega}\right)_{EXP} = S \left(\frac{d\sigma}{d\omega}\right)_{th}$ where S is the spectroscopic factor and $\left(\frac{d\sigma}{d\omega}\right)_{th}$ is the theoretical result (En 66).

Of special interest is the spectroscopic factor S. It expresses the degree to which the final state is composed of the target state $\psi_{J_i M_i}$ with a neutron bound in an orbit with quantum numbers l, j . It is a measure of the reduced neutron width of the initial state.

In the Lane and Lynn theory the direct component of radiative transition may dominate if the final state has a large p-orbit single particle component. The dependence of the direct component on the single particle reduced width is identical to the dependence of the (d,p) strength on the spectroscopic factor. Furthermore for s-wave neutron capture followed by E1 decay the final states that will be preferentially populated will be the same as the final states

for which $l_n = 1$ in the (d,p) reaction. It is therefore expected that in these situations a significant correlation can be expected between the (n, γ) and the (d,p) strengths.

A simplified treatment in terms of the initial and final states can be given as follows. Consider an s-wave neutron incident on a target with spin J_t . The initial wave function can be written as $|S J_t\rangle$. If the final state wave function is $|J_f\rangle$ then the matrix element for the emission of an E1 gamma ray is $\langle J_f | E1 | S J_t \rangle$. In the case where no compound nucleus is formed $|J_t\rangle$ is undisturbed, hence $\langle J_f | E1 | S J_t \rangle = \langle J_f | p | J_t \rangle$. Since the matrix element is large where there is an appreciable overlap between the initial and final states then its value is dependent on the amount of p-state in the final state configuration. This dependence is the same as in the (d,p) reaction and therefore correlation between (n- γ) and (d,p) strengths is expected when the proper final states are populated.

A more accurate result is provided by Clement^(Pr 67).

For a radiative transition to a final state of spin J_f following neutron capture in a target of spin J_i , the strength is

$$(2J_f+1) \sum_{J_r=J_i+1/2} \lambda_r (2J_r+1) \left[2 \begin{Bmatrix} \frac{3}{2} & \frac{1}{2} & 1 \\ J_r & J_f & J_i \end{Bmatrix} S_{3/2} - \sqrt{2} \begin{Bmatrix} \frac{1}{2} & \frac{1}{2} & 1 \\ J_r & J_f & J_i \end{Bmatrix} S_{1/2} \right]^2$$

where J_r = spin of the capture state

$S_{1/2}, S_{3/2}$ = stripping amplitudes for the $p_{1/2}$ and $p_{3/2}$ components of the final state

λ_I = relative contribution from each intermediate spin state.

This expression reduces to the (d,p) strength $(2J_f + 1) \times [S_{3/2}^2 + S_{1/2}^2]$ if $\lambda_{J_i - 1/2} = \lambda_{J_i + 1/2}$. Therefore unless

the intermediate spin contributions are equal the measured correlation coefficient between the (n, γ) and (d,p) strength may not be significant even though a direct component in the radiative cross-section may be dominant.

A detailed derivation of this formula is shown in Appendix 1.

CHAPTER III

B¹⁰ FILTER RESONANCE CAPTURE METHOD

1. Introduction

As mentioned previously most of the available radiative capture data were obtained from thermal (n, γ) reactions. Because of the arbitrary point of capture relative to the resonance structure, interpretation of the thermal capture data is usually difficult. Besides the Porter-Thomas fluctuation, there is the effect of level-level interference which would yield anomalously weak or strong intensities.

An alternative method used is the individual resonance capture technique. In this arrangement the gamma ray spectra are studied as a function of incident neutron energies usually in the resonance region. The neutron energies are measured by time-of-flight techniques and are simultaneously recorded with the corresponding emitted gamma rays. Thus precise knowledge of the neutron energies clearly defines a specific capture state and therefore makes the interpretation of the resulting spectrum more straightforward. There is no level-level effect and fluctuation of the intensities is mainly due to the random variation of partial widths. In principle a good approximation to the average partial width can be obtained by including several resonances. This method however has the disadvantage of low neutron intensity because of the limitation on the duty cycle of the pulsed neutrons and enforced external geometry resulting in spectra of poor technical quality.

Basis of the B^{10} Filter Resonance Technique

The feasibility of the B^{10} filter resonance technique is based on two factors namely (1) the basic shape of the neutron spectrum from a moderated nuclear reactor and (2) the $1/E$ dependence of the B^{10} (n, γ) reaction cross-section.

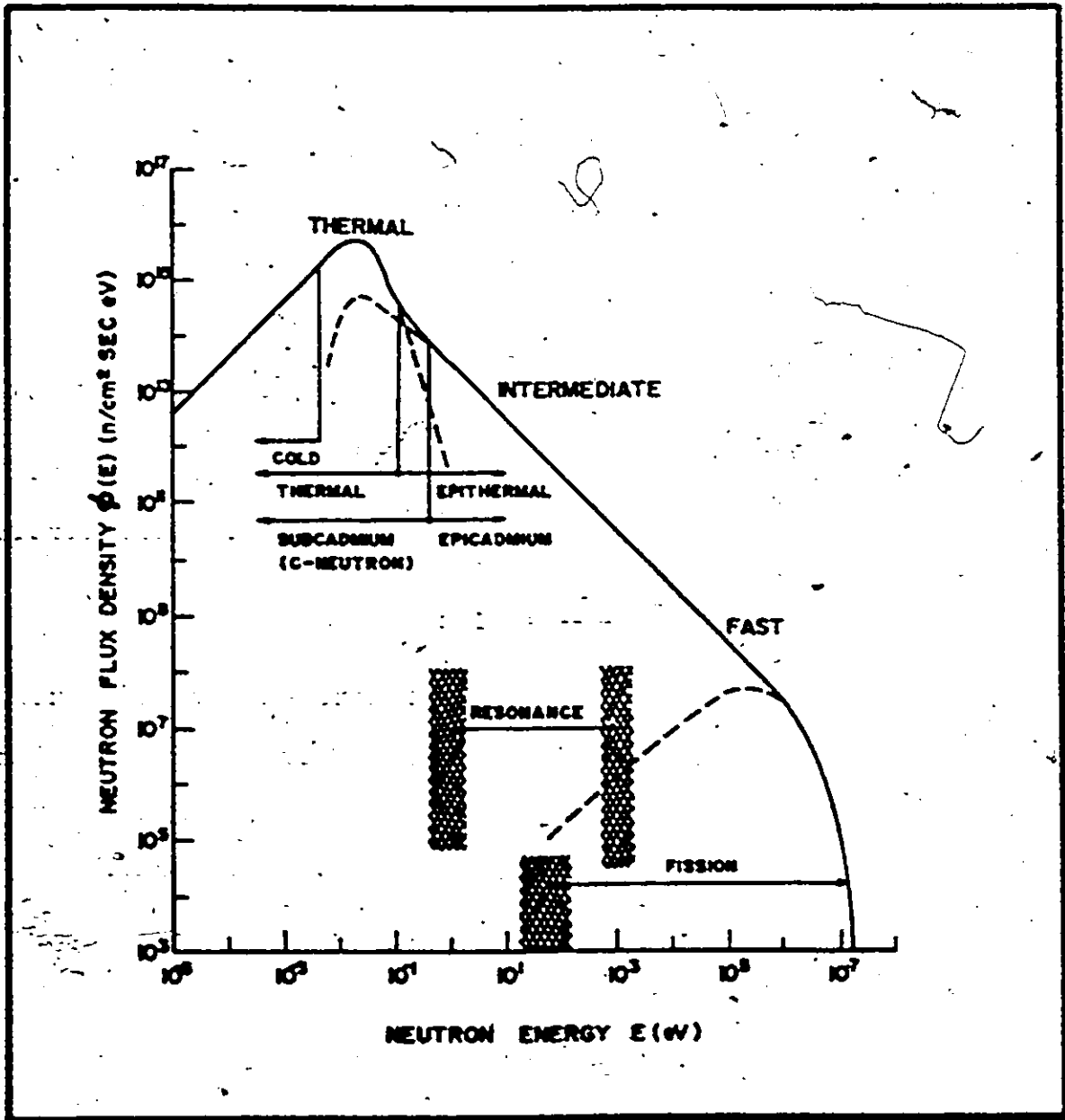
a. Neutron Spectrum

In the fission process energetic neutrons are produced whose spectrum is adequately fitted to the equation $S(E) = 4e^{-E} \sinh \sqrt{2E}$ and whose average energy is 2 MeV. These neutrons undergo elastic collisions with the moderator atoms and are slowed down until they are in thermal equilibrium with the moderator atoms. The resulting neutron spectrum is shown in Fig. 3.1 (Ia 70) and extends from a fraction of an eV to MeV. Mainly for convenience the neutron spectrum is divided into three regions namely fast, intermediate and thermal. The fast neutrons refer to those produced in the fission process (shown as dotted lines in Fig. 3.1) before undergoing any interaction with the moderator atoms.

In the intermediate region the energy dependence of the neutron flux $\phi(E)$ can be established as follows. If N is the atomic density of the moderator and σ_s the scattering cross-section then the number of collisions per sec per cm^3 at E is $C(E) = N\sigma_s \phi(E)$. Then if $\langle \Delta E \rangle$ is the average energy

Figure 3.1

Neutron Spectrum from a Water-Moderated Nuclear Reactor



loss per collision, the number of neutrons slowing down past energy E per second per unit volume is $q(E) = C(E) \langle \Delta E \rangle$. For neutrons with energies above thermal the fractional change in energy is constant (IAEA-70) i.e. $\epsilon = \frac{\langle \Delta E \rangle}{E}$. Hence $q(E) = \epsilon EC(E) = \epsilon EN \sigma_s \phi(E)$. Assuming negligible absorption in the moderator then the source density must equal $q(E)$.

Therefore

$$q = q(E) = \epsilon EN \sigma_s \phi(E)$$

$$\phi(E) = \frac{q_0}{\epsilon N \sigma_s E} = \frac{\text{constant}}{E}$$

In the thermal region the energy of the neutron is dependent on the energy distribution of the moderator atoms which is determined by the temperature. The flux energy distribution is described by the equation

$$\phi(E) = \frac{E}{kT^2} e^{-E/kT}$$

where E is the neutron energy, T is the moderator temperature and k is the Boltzmann constant. The most probable velocity is $V_0 = \left(\frac{2kT}{m}\right)^{1/2}$ and this is usually taken to be 2200 m/sec which corresponds to an energy of .025 eV.

As far as intensity is concerned, the thermal region is dominant. The $1/E$ neutron flux starts in the neighborhood of 1 eV and extends towards the fast region.

b. Effect of B^{10} as a Neutron Filter

1. Simplified Picture of the Filter

The dominant neutron capture reaction in B^{10}

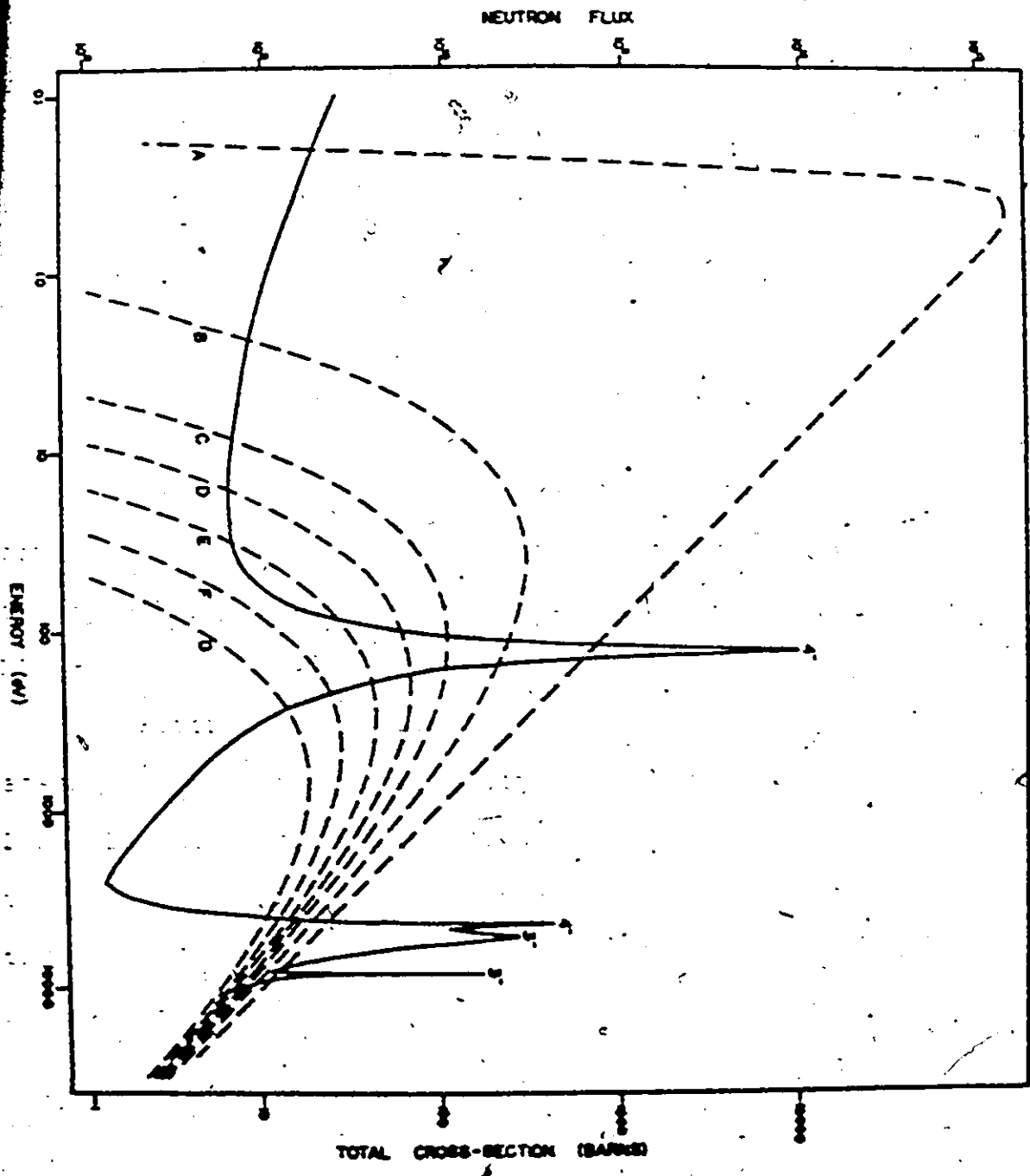
is $B^{10}(n,\alpha)Li^7$. The dependence of the cross-section on the neutron energy is given by $\sigma(E) = \frac{611}{\sqrt{E}}$ barns where E is in eV.

Since the thermal neutrons are removed by a cadmium filter, the main neutron spectrum incident on the B^{10} filter is assumed to follow the $1/E$ dependence of the intermediate region. For simplicity, consider a B^{10} filter of thickness n atoms/barn upon which a neutron flux $\phi(E) = k/E$ is incident normally. Then the flux passing through the filter is $\phi'(E) = \phi(E)e^{-n\sigma(E)} = \frac{k}{E} e^{-n611/\sqrt{E}} = \frac{k}{E} e^{-a/\sqrt{E}}$. Thus the effect of the filter is to reshape the $1/E$ spectrum. It cuts off the low energy neutrons and although it does not have much effect on the high energy neutrons, the $1/E$ dependence causes this region to fall off in intensity. This can be seen in Fig. 3.2 which shows the effect of different filter thicknesses actually used in the cobalt experiments.

The dependence of the position of the maximum of the filtered neutron spectrum on the filter thickness is given by $E_c = 1/4 a^2$. It can also be shown that the FWHM of the filtered neutron spectrum varies as the square of the filter thickness. This implies that to include as many resonances as possible one must use a thick filter. The main limitation is that the neutron intensity falls off with filter thickness and hence one must choose the filter size to obtain reasonable neutron flux.

Figure 3.2

Neutron Spectrum Obtained after Normal Incidence in a B^{10} Filter



In these experiments the B^{10} filter is used to vary the shape of the neutron spectrum permitting one to change the contribution of the different resonances of the sample under investigation. The resulting gamma ray spectrum is therefore a weighted contribution mainly from all the resonances which fall under the broad energy band of filtered neutrons.

ii. Actual Captured Neutron Spectrum

The calculation of the filtered neutron spectrum $\phi'(E)$ derived very simply above to illustrate the filtering process is complicated by geometrical complications in the sample configuration. All the cobalt and manganese samples are cylindrically shaped and are surrounded uniformly with B^{10} .

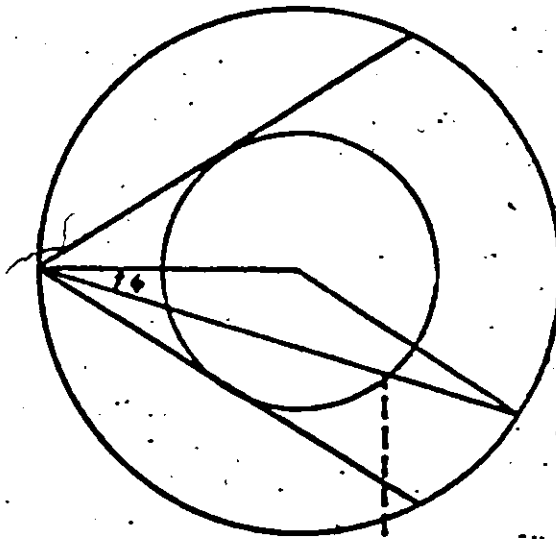
Referring to a schematic representation of a sample assembly shown in Fig. 3.3, consider a point of entry at $z < h$. Depending on θ and ϕ possible paths would be (a) through the filter and then through the upper end face of the sample (b) through the filter and then through two sides of the sample and (c) through the filter and then through the lower end face of the sample. Similar possibilities occur for $z > h$.

The path length travelled by a neutron through the filter and through the sample is a function of θ , ϕ , and z . Thus the neutron capture spectrum for neutrons of

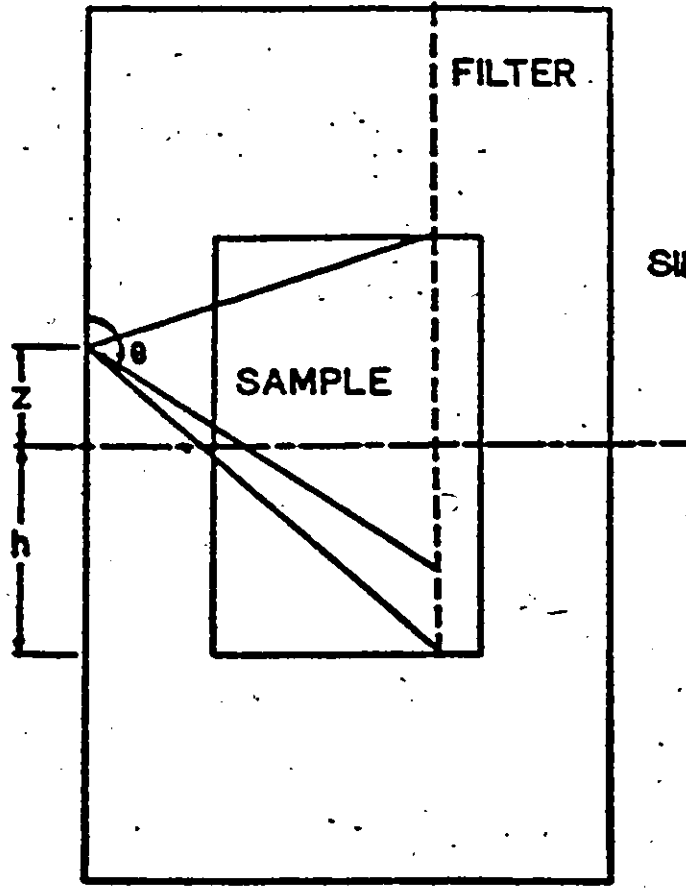
Figure 3.3

Schematic Diagram of a Typical Sample Assembly

SAMPLE GEOMETRY SCHEMATIC



TOP VIEW



SIDE VIEW

energy E can generally be expressed as

$$C_n(E) = \frac{\int \int \int e^{-\mu_B(E)l_B(\theta\phi Z)} \left[1 - e^{-\mu_s(E)l_s(\theta\phi Z)} \right] \frac{\sigma_Y(E)}{\sigma_t(E)} \sin^2\theta \cos\phi d\theta d\phi dZ}{\int \int \int \sin^2\theta \cos\phi d\theta d\phi dZ}$$

where $\mu_B(E)$ is the attenuation coefficient of B^{10} neutrons of energy E

$\mu_s(E)$ is the attenuation coefficient of the sample

$l_B(\theta\phi Z)$ is the path length traversed by the neutrons in the filter

$l_s(\theta\phi Z)$ is the path length traversed by the neutrons in the sample

$\phi(E)$ is the neutron flux at energy E

$\sigma_Y(E)$ is the capture cross-section of the sample at energy E

$\sigma_t(E)$ is the total cross-section of the sample at energy E

The results obtained for $l_B(\theta\phi Z)$, $l_s(\theta\phi Z)$ and the integration limits are summarized in Table 3.1 for all the possible cases. The contribution for $Z > h$ has been ignored because neutrons coming from this direction are attenuated by the cylindrical boron shield.

The total neutron capture over the whole energy range can now be written as $C_T = \int C_n(E) dE$. The fractional

TABLE 3.1

PATH LENGTHS AND INTEGRATION LIMITS FOR CYLINDRICAL FILTER GEOMETRY

Case	$l_B(\theta\phi)$	$l_B(\theta\phi)$	$\theta_1(\phi, \epsilon)$	$\theta_2(\phi, \epsilon)$
a	$(B-C)/\sin\theta$	$A/\cos\theta - l_B(\theta\phi)$	$\tan^{-1}((B-C)/A)$	$\tan^{-1}((B+C)/A)$
b	$(B-C)/\sin\theta$	$2C/\sin\theta$	$\tan^{-1}((B+C)/A)$	$\tan^{-1}(-(B+C)/D)$
c	$(B-C)/\sin\theta$	$-D/\cos\theta - l_B(\theta\phi)$	$\tan^{-1}(-(B+C)/D)$	$\tan^{-1}(-(B-C)/D)$
a	$A/\cos\theta$	$(B+C)/\sin\theta - l_B(\theta\phi)$	$\tan^{-1}((B+C)/A)$	$\tan^{-1}(-(B-C)/A)$
b	$(B-C)/\sin\theta$	$2C/\sin\theta$	$\tan^{-1}((B-C)/A)$	$\tan^{-1}(-(B+C)/D)$
c	$(B-C)/\sin\theta$	$-D/\cos\theta - l_B(\theta\phi)$	$\tan^{-1}(-(B+C)/D)$	$\tan^{-1}(-(B-C)/D)$

R = radius of the boron filter

r = radius of the sample

A = h - s

B = R cos φ

C = R² cos² φ - (R² - r²)

D = h + s

contribution of the i^{th} resonance is given by

$$f_i = \frac{\int_E C_R(E) \frac{\sigma_{\gamma i}(E)}{\sigma_{\gamma}(E)} dE}{C_T}$$

The results obtained for the expected contributing resonances are given in Table 3.2 for cobalt and Table 3.3 for manganese.

iii. Effect of Multiple Scattering

It is important to consider the effects of multiple scattering within the B^{10} filter and the samples.

For the B^{10} , the scattering cross-section is negligible compared to the (n, α) reaction. Furthermore because of its low mass number, neutrons can be easily scattered to lower energies and be readily absorbed. Hence its effect on the shape of the neutron spectrum incident on the sample may be ignored.

For the sample the effect of multiple scattering can be seen as follows. A neutron of initial energy E will have a lower energy E' due to collision with the sample nuclei in the following manner: $E' = E/2 \left[(1+a) + (1-a) \cos \psi \right]$ where $a = \left(\frac{A-1}{A+1} \right)^2$ and ψ is the angular direction of the scattered neutron. The average energy loss per collision for a neutron of energy E can be shown to be $\langle \Delta E \rangle = \frac{1}{2}(1-a)E$. Assuming the probability for loss of the scattered neutron to be equal to $1-P$ it is shown in Appendix 2 that the proper scattering response function is $R(E_0, E) = (\gamma+1) \frac{E^\gamma}{E_0^{\gamma+1}}$ where E_0 is the initial neutron energy, E is the energy after

TABLE 3.2

FRACTIONAL CONTRIBUTION OF CO RESONANCES (%)

Resonance Energy	Spin	Nominal Filter Thickness (Inch)							
		0'	1/8	3/16	1/4	3/8	1/2	5/8	
-268	3	19.653	4.594	3.653	3.453	3.359	3.232	2.935	
5015	3	1.812	3.902	7.005	9.890	13.908	19.082	24.507	
8050	3	0.018	0.400	0.866	1.335	2.043	3.057	4.283	
13280	3	0.016	0.515	1.148	1.803	2.821	4.331	6.250	
15640	3	0.012	0.254	0.567	0.893	1.404	2.167	3.148	
21950	3	0.025	0.173	0.376	0.580	0.921	1.422	2.076	
132	4	78.105	87.987	81.941	75.366	65.574	52.142	36.843	
4322	4	0.309	1.286	2.491	3.625	5.230	7.336	9.588	
10700	4	0.034	0.624	1.365	2.123	3.286	4.984	7.098	
16920	4	0.018	0.265	0.588	0.926	1.455	2.248	3.271	

TABLE 3.3

FRACTIONAL CONTRIBUTION OF Mn RESONANCES (%)

Resonance Energy	Spin	Nominal Filter Thickness (Inch)							
		0	1/8	3/16	1/4	5/16	7/16	1/2	
2830	2	3.290	0.649	0.450	0.416	0.386	0.366	0.361	
335.5	2	62.493	68.974	60.824	57.228	52.088	44.647	40.918	
7110.0	2	0.570	1.145	1.787	2.108	2.623	3.509	4.029	
-76	3	18.264	0.915	0.309	0.221	0.148	0.091	0.074	
1098	3	3.699	18.372	23.925	25.948	28.572	31.863	33.279	
2355	3	11.224	8.945	11.110	12.182	13.799	16.290	17.600	
8740	3	0.453	1.000	1.595	1.896	2.384	3.234	3.740	

collision and $\gamma = \ln F / \ln(1 + \frac{\alpha}{2})$. If the initial incident spectrum is $\phi_{in}(E_0)$, the effective spectrum is

$$\phi(E) = \int_E R(E_0, E) \phi_{in}(E_0) dE.$$

Whereas the effect of the geometrical considerations is to increase the effective filter thickness, the effect of multiple scattering is to decrease it. The final result for cobalt which includes both geometry and scattering is shown in Fig. 3.4. The percentage contribution for the cobalt resonances including the effects of geometry and scattering is shown in Table 3.4.

Figure 3.4

Neutron Spectrum Obtained with Actual Sample Geometry and
Including Multiple Scattering Effects

CALCULATED NEUTRON FLUX
(SAMPLE GEOMETRY AND MULTIPLE SCATTERING
INCLUDED)

NEUTRON FLUX ($n/cm^2-sec.$)

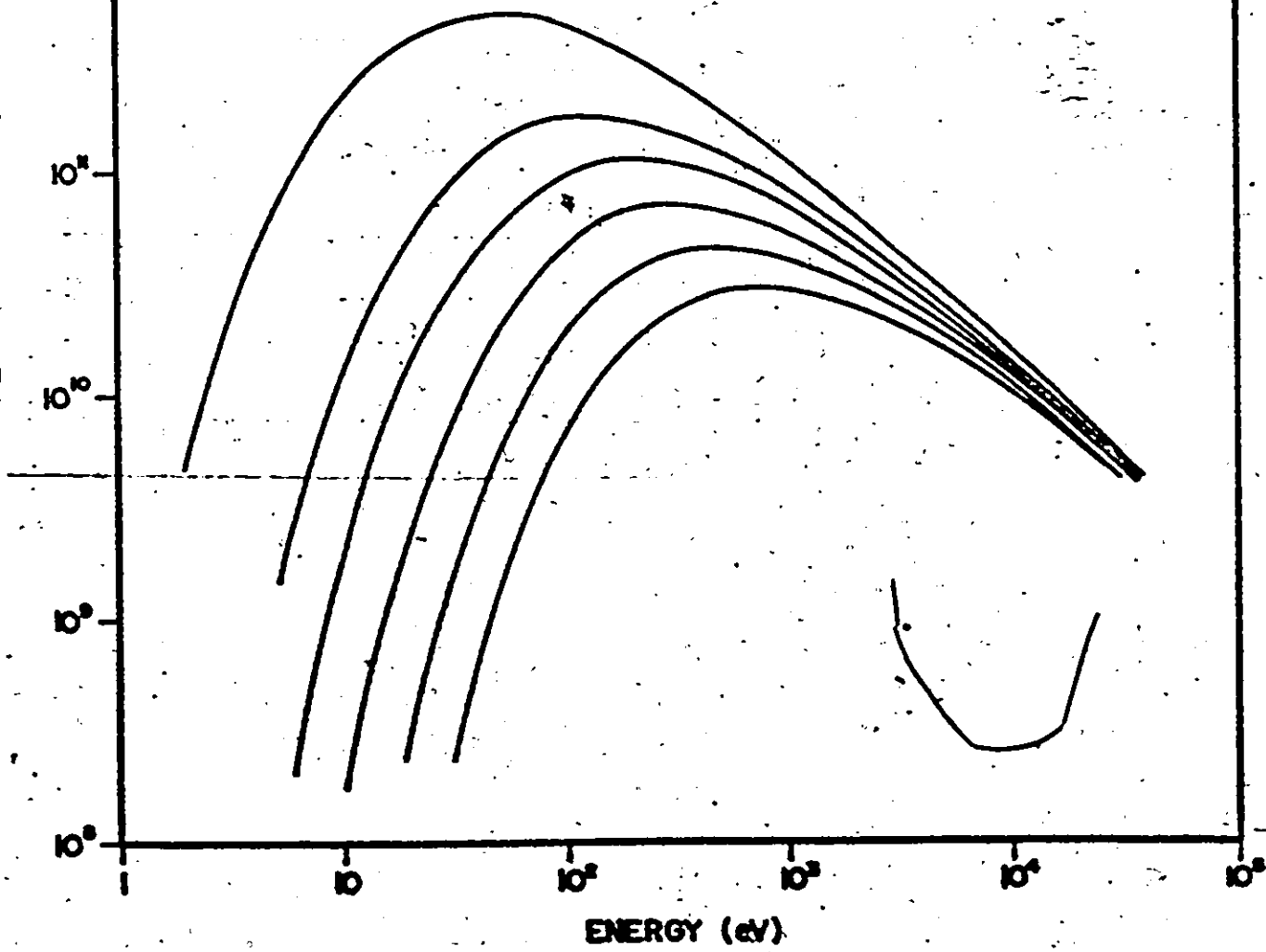


TABLE 3.4

Percentage Contributions - Scattering and
Geometry Included

Resonance Energy	Nominal Filter Thickness (Inch)						
	0	1/8	3/16	1/4	3/8	1/2	5/8
-268	17.0	4.81	3.76	3.56	3.50	3.44	3.24
5015	1.77	3.69	6.52	9.18	13.0	18.1	23.8
8050	0.031	.37	.78	1.20	1.84	2.78	3.99
13280	0.020	.27	.60	.93	1.46	2.26	3.33
15640	0.02	.23	.50	.79	1.24	1.93	2.85
21950	0.03	.16	.33	.52	.81	1.26	1.86
132	80.7	88.5	83.5	77.8	69.1	56.8	42.1
4322	0.32	1.20	2.29	3.35	4.84	6.9	9.27
10900	0.05	.57	1.23	1.91	2.95	4.53	6.58
16920	0.025	.24	.53	.82	1.29	2.01	2.98

CHAPTER IV
INSTRUMENTATION

1. NEUTRON SOURCE

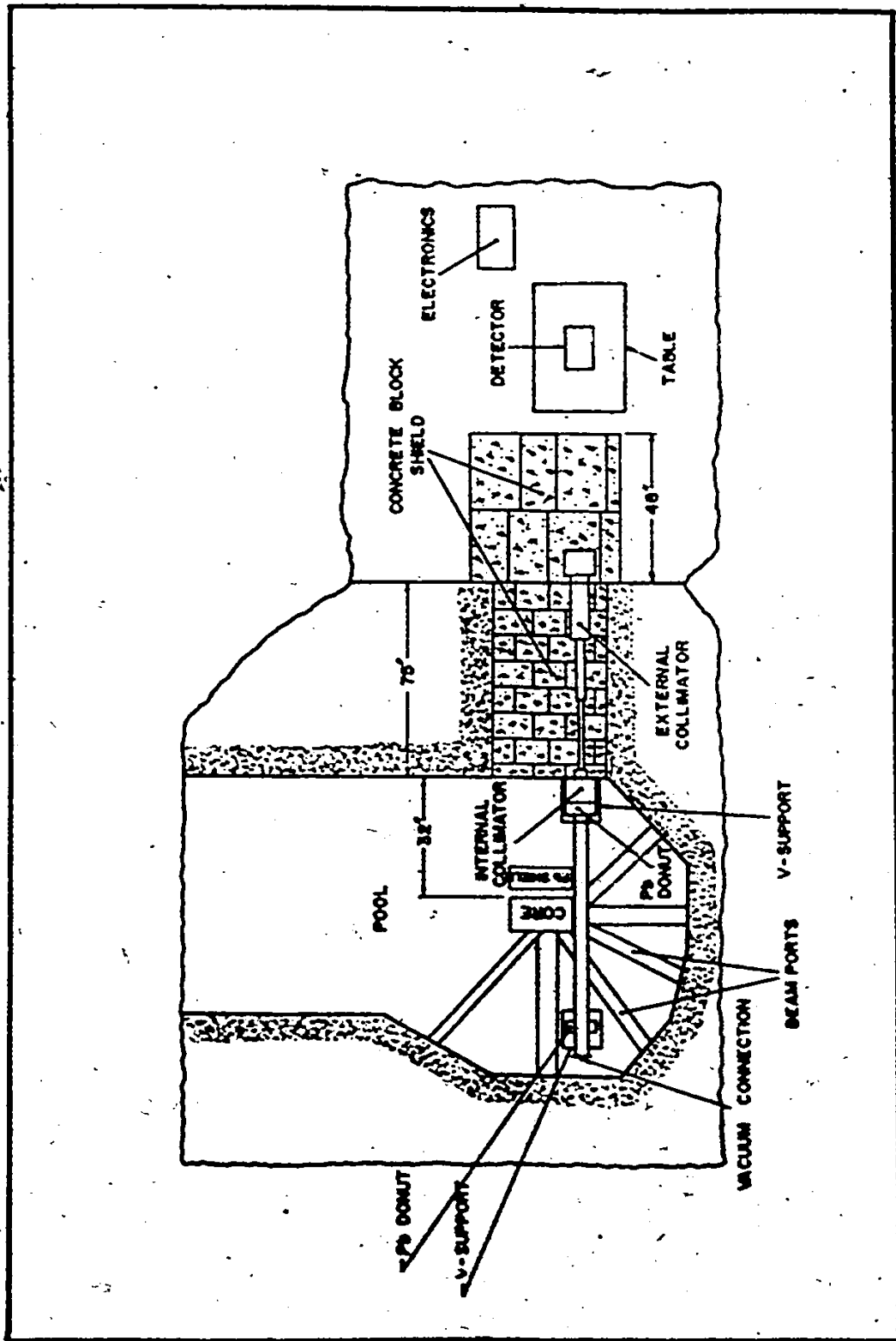
The source of neutrons used in these experiments is the McMaster University Reactor. It is a 2 MW swimming pool reactor using uranium enriched with U^{235} as fuel, and light water as coolant and moderator. A general layout of the reactor facilities is shown in Fig. 4.1.

As shown there are six radial beam ports each of which extends from the core through the wall surrounding the pool into the experimental area. These beam ports are equipped with bismuth plugs to attenuate the gamma radiation from the core without greatly affecting the outgoing neutron flux. When no experiment is being done the neutron beam may be shut off by placing neutron absorbers in front of it. In the floor area where a sample may be positioned the thermal flux is of the order of 10^6 n/cm²/sec.

There is also a vertical beam tube for experiments which require flexibility in sample position. This tube occupies a position normally occupied by a fuel cell and extends to the bridge area. A sample may be located in the core for higher neutron flux and the gamma rays from the sample are collimated towards a detector located on the bridge. If it is required that the sample be located on the bridge, as in coincidence

Figure 4.1

General Layout of the Nuclear Reactor Facilities



experiments, then a neutron scatterer may be placed in the core to increase the neutron flux incident on the target. Although this facility is very adaptable to many requirements there is the problem of unusually high background radiation in the bridge area. Furthermore the amount of equipment that can be installed is very limited because of the small space available.

For resonance capture experiments the primary considerations that determine the design of the experimental facility to be used are:

1. Requirement of high-sensitivity.
2. Minimum background radiation to yield an adequate signal to noise ratio.
3. Sufficient room in the sample position to accommodate large sample holders which will contain a B^{10} filter and the sample.

Since none of the existing facilities satisfied these requirements it was decided to build a horizontal irradiation system with tangential geometry. Three basic systems were constructed before a suitable arrangement was achieved.

2. TANGENTIAL THROUGH-TUBE IRRADIATION FACILITY

A. General Considerations

From the brief description of the reactor facilities given above, one can see that there are two basic alternative geometrical arrangements of neutron source, target and detector

which can be used for (n, γ) work. In an experiment using an external beam port, neutrons are extracted from the core and are allowed to interact with a sample under investigation suitably positioned in front of the beam.

The gamma rays, emitted isotropically following the absorption of a neutron, are observed with a counter located near the target. Thus positioning of the sample, the detector, and necessary background shielding is fairly easy and convenient. Furthermore the sample shape and size may be varied without much difficulty.

In an internal target facility such as the tangential through-tube, the target under investigation is located in the high flux region of the reactor. The capture gamma rays pass through a collimation system and are viewed by a detector located at a distance from the target. Hence the size and shape of the sample is much more limited. Coincidence experiments are not possible. Furthermore, because of the high radiation field of the order of 10^{13} n/cm²/sec for the thermal neutron flux, the targets are much more radioactive and hence may introduce handling problems.

For the resonance capture experiments the problems encountered in the internal target arrangement are either not significant or can be remedied. At the same time it offers the advantage of greater sensitivity which is very important.

For a given sample size, assuming the same detector efficiency, consideration of all factors affecting the counting

rate yields the following ratio of the internal to external geometrical sensitivity

$$R = \frac{T_{ni} \Omega_{ni} T_{yi} \Omega_{yi}}{T_{ne} \Omega_{ne} T_{ye} \Omega_{ye}}$$

The subscript i and e refer to the internal and external factors respectively. The solid angle subtended by the target relative to the neutron source is Ω_n while Ω_y refers to the solid angle subtended by the target relative to the detector. T is the transmission of the neutron or gamma ray beam through materials that may be along the beam path.

If one examines the terms individually, one finds that the main difference arises from the solid angles. Typical values are as follows:

$$\frac{\Omega_{ni}}{4\pi} = 0.75 \quad (\text{isotropic neutron source on one side with 50\% reflection from water})$$

$$\frac{\Omega_{yi}}{4\pi} = 10^{-6} \quad (\text{for } 1^\circ \text{ beam})$$

$$\frac{\Omega_{ne}}{4\pi} = 10^{-6} \quad (\text{for } 1^\circ \text{ beam})$$

$$\frac{\Omega_{ye}}{4\pi} = 3 \times 10^{-2} \quad (\text{for an } 8 \text{ cm}^2 \text{ Ge(Li) detector located } 5 \text{ cm from the target})$$

Substituting in the preceding equation one gets

$$R = 25$$

This increase in sensitivity is very important since in the resonance capture experiments, the use of B^{10} filters already result in neutron losses.

It is also expected that background radiation will be less in the internal target geometry. The main contribution will be from photons and neutrons from the reactor core which are scattered towards the detector by the target or surrounding materials. The Compton scattered photons can be made small by proper collimation and positioning of the target whereas the neutrons can be attenuated by a combination of a thermalizing material and neutron absorbers such as borax inserted between the collimation system and the detector. In the external geometry photons streaming from the reactor core may be scattered towards the detector. Neutrons from the beam may also be scattered by the target to surrounding materials or towards the detector resulting in subsequent gamma radiation upon absorption of these neutrons. Minimization of photons scattered by the target to the detector cannot be achieved without attenuating the gamma rays emitted by the target. For the scattered neutrons one may insert non-radiating neutron absorbers to lessen their contribution. Since the detector will have to be moved farther from the target, the solid angle will be smaller which consequently results in a loss in efficiency. Thus the internal geometry arrangement presents itself as the obvious choice for the resonance capture experiments.

B. Through-Tube Design #1

The initial through-tube design (Ni 70) consisted of 7.6 cm OD 65 ST aluminum pipe 2¹/₂ in length. Stainless steel wires attached to cylindrical Pb "donuts" which are secured on the ends of the tube are used for manipulating it in the proper position near the core. (See Fig. 4.1). The portable tube sits on V-notches and alignment with the internal and external collimation system is attained through the Pb "donuts" sitting on the V. The sample assembly, consisting of the target and boron filter is located inside the tube by means of aluminum strips and is strategically positioned to obtain the maximum neutron flux with the minimum scattering of radiation from the reactor core.

To protect the boron filter from thermal neutrons, a cadmium slider, consisting of Cd metal (.45 gm/cm²) wrapped around a movable 2 foot thin-walled aluminum pipe riding on the through-tube, is secured symmetrically about the sample position. Shielding of the B¹⁰ filter from thermal neutrons is done for two reasons - to keep the background radiation from thermal neutron capture in B¹⁰ to a minimum and to keep the production of heat resulting from the (n, α) reaction small. Heating problems which may cause sample melting are not anticipated because there is good contact between the target assembly and the walls of the through-tube which are being constantly cooled by the pool water.

The geometrical position of the tangential tube is such that direct gamma radiation from the core is negligible. A

lead shield 10 cm thick and with an area more than sufficient to cover the reactor core face is located between the core and the detector. Inside the pool, an internal collimator, consisting of a cylindrical lead annulus 15.2 cm OD, 22.9 cm long with a 2.5 cm central hole sits adjacent to one end of the tube on the V-support close to the detector. To remove the water filling up the central hole which contributes background radiation from the reaction ${}^1_0\text{H}(n,\gamma){}^2_0\text{H}$ and from Compton scattering of gamma radiation from the core, an empty closed-end aluminum tube is inserted. The end caps are constructed so they can contain Li^6F powder which is used to absorb neutrons scattered towards the detector. Outside of the pool, adjacent to the wall on the detector side are massive blocks of concrete and baryte shielding which is arranged to prevent streaming of radiation.

The external collimation system consists of a 1 cm aluminum tube encased in a rectangular aluminum container with varying cross-sections and filled with polyethylene and lead shots. The stepping of different sections of the container is to prevent a direct radiation path. The collimator is 20.3" long and the detector is located 15.2" away from the nearest end. The wall which separates the internal and the external collimators is thinned down to minimize its contribution in background radiation.

Even though these initial tubes have great portability, sample changing is not very convenient. One needs a different tube for a different sample. The tube which contains a sample

just irradiated cannot be used because it is usually too radioactive for handling and a cooling period which depends mainly on the decay rate of the target is required. The cadmium slider is usually radioactive too, however, it can be slid to one end of the tube which is underwater during this operation and is therefore shielded. Thus a minimum of three tubes is required for continuous operation assuming that a week is sufficient for radioactive decay time. Nonetheless unnecessary radiation dosage is received during a sample change as the tube has to be partly brought up to the pool surface for dismantling to get to the old sample.

A major defect in this design is the time loss during these tube changes. The reactor has to be shutdown so that the core can be moved from the neighborhood of the tube while the change is being made. This is very time consuming. The operation requires at least four people and a minimum of one hour. Furthermore there is always the possibility of misaligning the system during the process since one of the V-notches is designed to be movable and adjustable. There is then no guarantee that the sample is located in the same position so that it may be necessary to make intensity and energy calibration for every run. In this system, calibration is done by introducing nitrogen gas into the tube by means of a 0.63 cm OD stainless steel tube welded to the far end cap of the through tube and extending to the surface of the pool. During an experiment the system is usually evacuated through the same tubing by a mechanical pump.

C. Through-Tube Design #2

From the previous experience it was found that enough statistics were obtained after data accumulation of at most a week for a typical sample. With through-tube design #1, this meant frequent sample changes and frequent reactor shutdowns.

To improve the flexibility of the system it was decided to modify the basic design of the through-tube to facilitate sample changing without shutting down the reactor or moving the through tube. The result is a semi-portable through-tube in the sense that it is not as easily manipulated and is especially designed for resonance capture experiments. A schematic diagram of this new arrangement is shown in Figs. 4.2 and 4.3.

This through-tube has the same physical dimensions as #1. The main difference is the system of aluminum and plastic tubing forming an S-shape configuration which is welded at a right angle to the tube near the core where the sample assembly is to be positioned. The lower part of this tubing assembly is made up of 2.54 cm ID aluminum tubing and makes an angle of 60° from the vertical to clear the ion chambers by the core. To prevent radiation streaming, a second section of curved aluminum tubing which rests against the wall of the pool connects the first section to the plastic tubing which extends to a sample insertion position near the surface of the pool. A sample is lowered to the sample position near the core by means of aluminum wires. The whole system can be evacuated by means of a 0.63cm stainless steel tubing welded to the sample insertion cap or pressurized with nitrogen gas if desired.

Figure 4.2

General Arrangement for Through-Tube Design #2

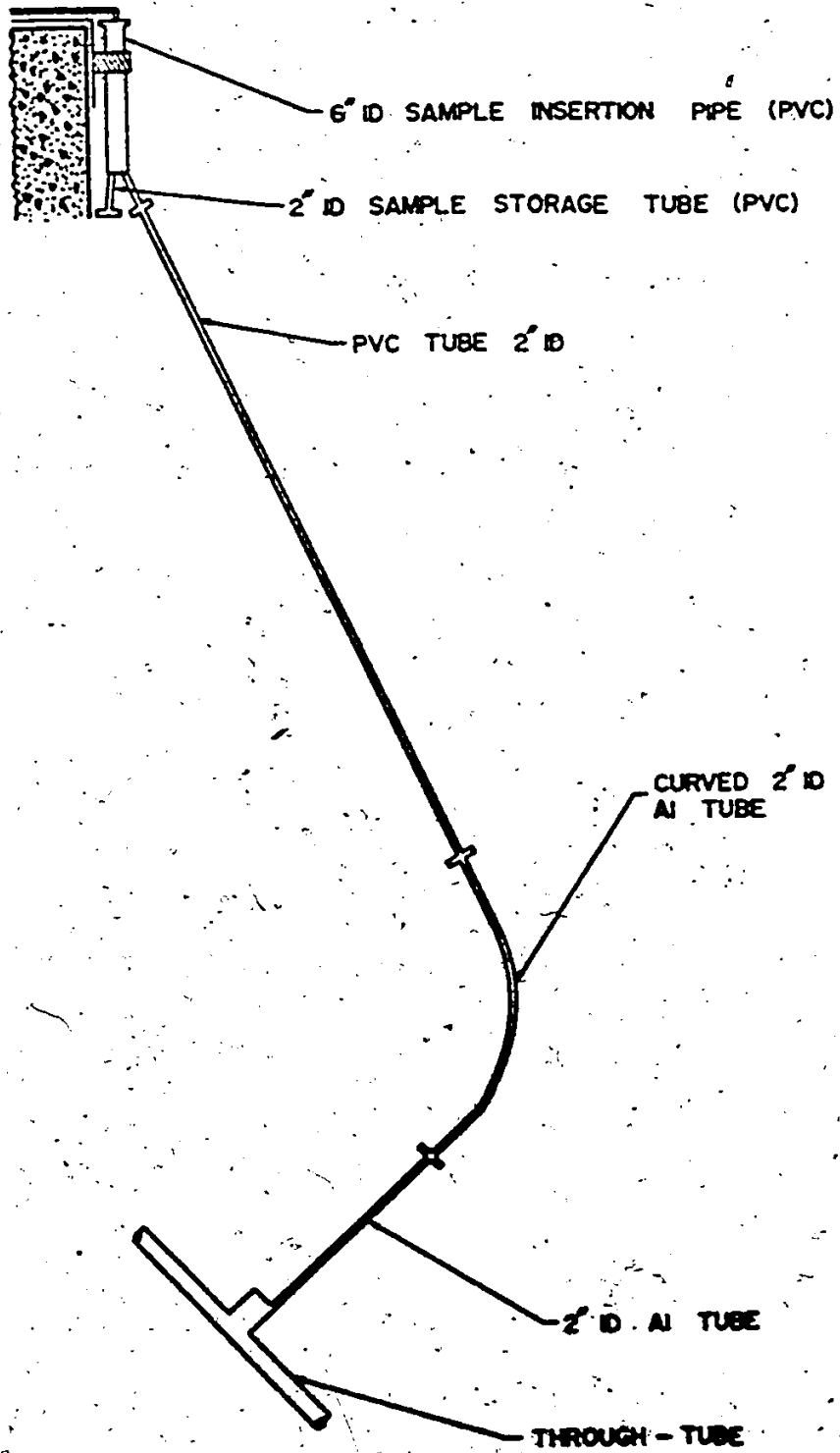
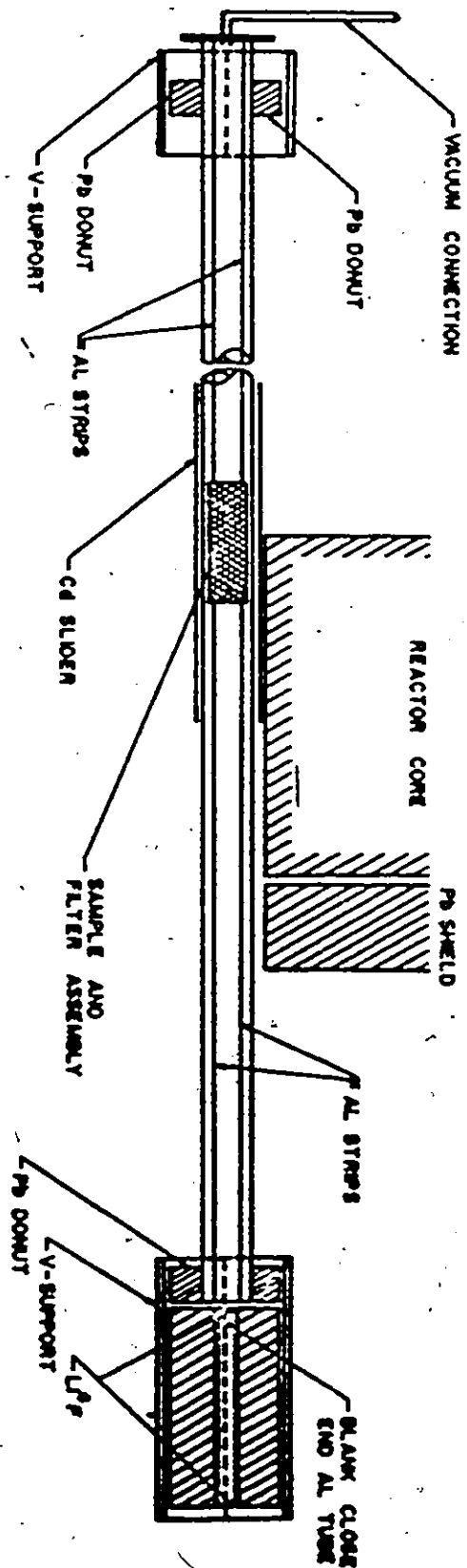


Figure 4.3

Details of Through-Tube Design #2

THROUGH-TUBE
DESIGN NO. 2



The S-shaped tubing assembly is made up of two parts because, in the neighborhood of the core, the plastic material (PVC-polyvinyl chloride) may not withstand the high radiation field. Near the surface of the pool it is adequate to use the plastic which has the advantage of flexibility and lightness - a great convenience during installation or removal.

Inside the through-tube, the sample is positioned vertically by means of a tapered seat which ensures that the sample axis passes through the detector view. This tapered support made of aluminum is located so it cannot be seen by the counter. The cylindrical sample and filter holder is made of carbon. The maximum OD for the sample holder is 2.29 cm.

To protect the B^{10} filter from thermal neutrons, a cylindrical annulus of natural B_4C filter is placed strategically near the sample position. In addition the natural filter is surrounded by cadmium metal which is wrapped around the outside of the through-tube.

Although this new system solved the previous problems it is not fully satisfactory. The main difficulty is the poor quality of the spectrum obtained with thick B^{10} filters. The main reason is that as more B^{10} surrounds the sample, not only is the sample size decreased, but also the relative amount of B^{10} seen by the detector is increased. This results in higher background, in an already lower signal, yielding an unsatisfactory spectrum.

D. Through-Tube Design #3

The main problem now is how to increase the signal to noise ratio. First, this can be done by modifying the through-tube to allow for a large sample holder which will contain a B^{10} filter and the sample. The sample should be large enough so that a reasonable signal to noise ratio is attainable even for the thickest filter. Secondly, background radiation from the reactor core and the surroundings should be minimized.

An obvious solution to the first part is a bigger overall system. However, a larger tangential through-tube cannot be used unless one is willing to alter the alignment of the collimation and the detector system. The operating position of the reactor core cannot be moved and the central axis of a bigger tube cannot be made to coincide with the present tubes. Hence one is limited to the same size through-tube in order to be able to use the existing external collimation system.

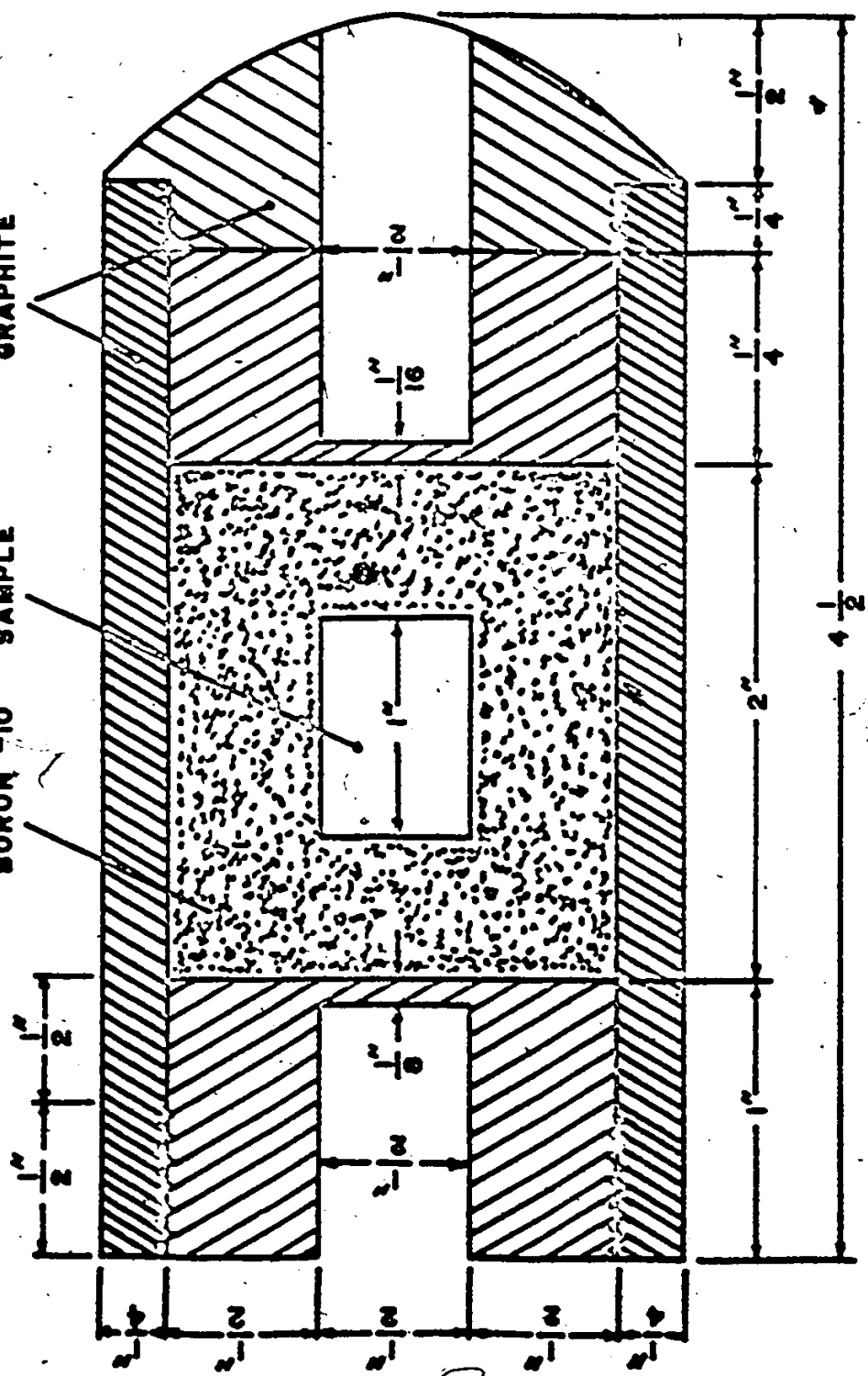
However, one can increase the size of the S-shape tubing to allow a large sample assembly and by proper positioning of the sample, a bigger effective size target can be viewed by the detector. For these experiments the maximum sample holder size is estimated to be 5 cm OD and 11.4 cm in length. This corresponds to a maximum sample size of 1.27 cm diameter and 3.81 cm long surrounded by the maximum B^{10} filter thickness planned which is 1.59 cm all around and a carbon holder with 0.16 cm wall thickness. A typical sample assembly is shown in Fig. 4.4. This requires that the sample insertion tubing

Figure 4.4

Typical Sample Assembly for Through-Tube Design #3

GRAPHITE

BORON-10 SAMPLE



should have an inside diameter a little over 5 cm. Since connection to the existing through-tube size can be done easily this solution was adopted.

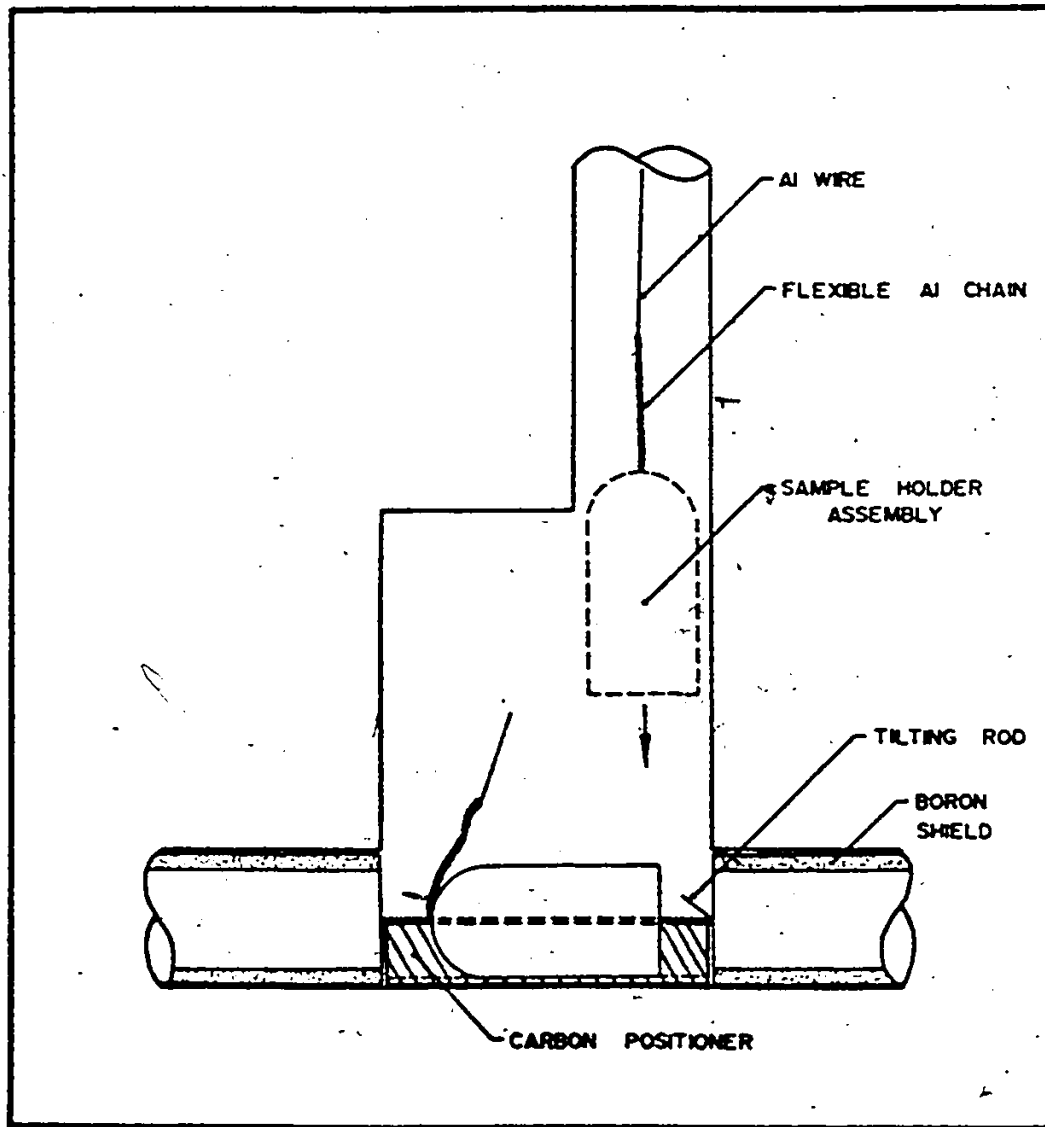
The seating of the sample holder in the through-tube required special consideration. The easiest way of placing the sample is to lower it through the S-wave shaped tubing and let it sit vertically as in #2. Since the detector view is only 1.25 cm, the effective target size, i.e. the target viewed by the detector, cannot be greater than this. Even with larger diameter sample insertion tubing, the increase in sample size is not sufficient to give a satisfactory signal to noise ratio hence a better scheme is required.

A desirable alternative is one where the sample can be positioned horizontally so that although the radial view size is limited, the axial extent of the sample can be longer. In this way the effective sample size can be made bigger by making longer targets. The only restriction then, as far as target length is concerned, is the self-attenuation of the gamma rays coming from the opposite end of the target. For cobalt and manganese the half-length is of the order of 4 cms.

To achieve this, a special arrangement in the sample position is made. The positioning of the sample is shown in Fig. 4.5. The sample is lowered vertically by means of a 4" aluminum chain immediately attached to the top of the carbon sample holder assembly and extended to the top by connected sections of aluminum wires. A rectangular enclosure welded on the aluminum through-tube allows the sample holder freedom

Figure 4.5

Positioning of Sample Assembly in Through-Tube #3



to swing from the vertical to the horizontal position. Two aluminum rods located halfway from the bottom of the through-tube are welded to the boron shield at an angle so that they hit the bottom of the sample holder as it is being lowered. This creates imbalance on the holder forcing it to tilt and then fall horizontally to a graphite positioner located concentrically at the bottom of the through-tube. The graphite positioner ensures that the target cross-section is aligned with the collimation system. Since the carbon sample holders must be of the same size to ensure this alignment, samples with thin B^{10} filters require sample holders with thicker walls.

Cadmium sheet, 0.45 gm/cm^2 thickness, is used to clad the horizontal tube over the extent of the reactor core, as well as the rectangular enclosure together with a portion of the sample insertion tube. This ensures a minimum of thermal neutrons hitting the B^{10} filter surrounding the sample. In addition to the cadmium wrapping, a boron shield consisting of natural boron contained in two sections of aluminum annuli which are connected together by aluminum rods is used to protect the B^{10} filter faces inside the sample holder from epithermal neutrons. As a secondary purpose it holds and positions the graphite positioner and the additional collimation inside the tube.

From the experience with the first designs there are three main sources of background radiation namely (1) scattering of core radiation by the sample holder assembly, (2) Compton

scattering of the core radiation by the aluminum material (i.e. through-tube end caps, swimming pool wall, ends of blank tube inside the internal collimator central hole) seen by the counter and (3) radiation from neutron capture in the aluminum materials as in (2). Not much can be done about (1) since the sample position has already been optimized. However (2) and (3) can be minimized by slight modifications.

The solution to (2) and (3) is accomplished by (a) decreasing the amount of aluminum material in the detector view, (b) shielding the remaining aluminum material from the core gamma rays and (c) reduction of thermal flux in this vicinity by using neutron absorbers.

To reduce the aluminum materials, the through-tube is extended up to the pool wall by a 2.54 cm ID aluminum tube welded at its end cap. The 2.54 cm ID tubing is capped with an .08 cm thick aluminum disc. Inside and at the end of this tube a disc of Li^6F is inserted to remove scattered neutrons. This disc of Li^6F is made self-supporting by mixing Li^6F powder with epoxy glue.

To facilitate the installation of this new tube by the core, a new internal collimator consisting of two halves was also built. The lower half sits on the V-notch. After the through-tube is in place, the upper half is placed on top of the lower half. The 2.5 cm extension sits snugly in the central hole formed by the two halves. Each half of the new internal collimator is wrapped with cadmium metal to protect the pool wall and the 2.54 cm tube and cap from thermal neutrons.

The Compton background is reduced by means of a cylindrical lead annulus inside the through-tube. It consists of three sections and is retained in place by the boron shield. The inside diameter of this lead shield is varied to accomplish a very effective shielding and to ensure at the same time that the walls are not in the detector line of sight.

This final design shown in Fig. 4.6 yields a very satisfactory result. The improvements afforded by these modifications can be seen by comparing the intensity of the aluminum line at 7725 keV observed in the previous systems with that in the new system. This is shown in Fig. 4.7.

3. DETECTING SYSTEM

A. Introduction

In these experiments, all the information of interest is necessarily contained in the energy and intensity of the gamma rays. It is therefore very important that these parameters are obtained with good accuracy.

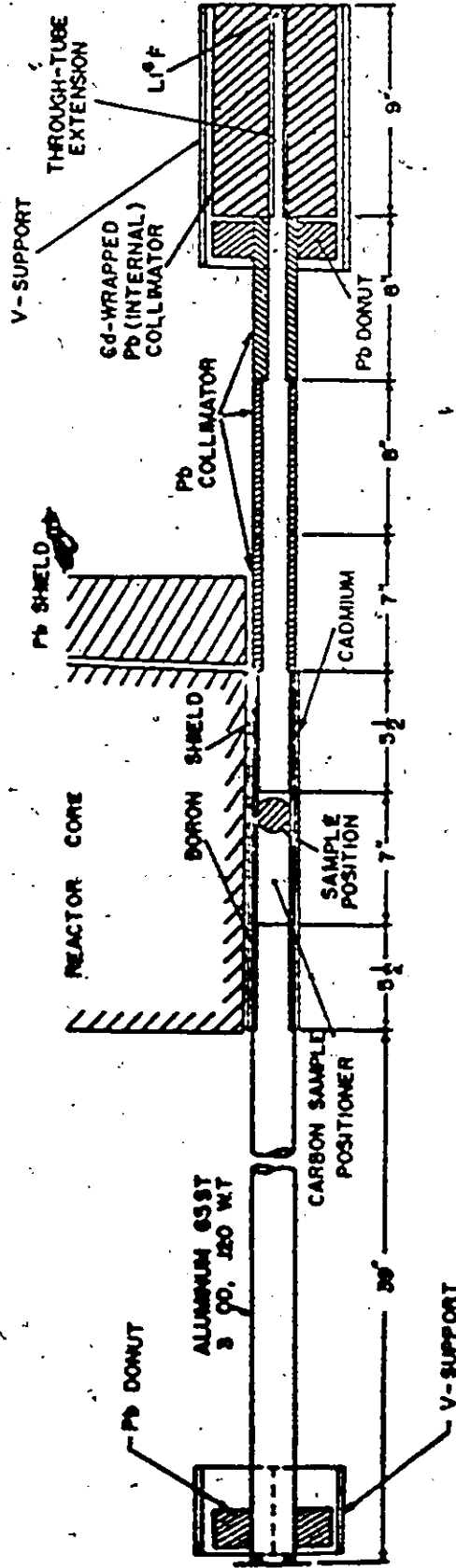
An ideal detection system would be one where the input signal is exactly identical to the output signal. Thus a gamma ray spectrum would be characterized by peaks with small widths (energy level widths) whose heights are equal to the relative intensities and whose positions are linearly related to the energies. Such a system is said to have a delta response function.

In practice every detection system exhibits a characteristic non-delta response function. Since the final output is

Figure 4.6

Final Through-Tube Design #3

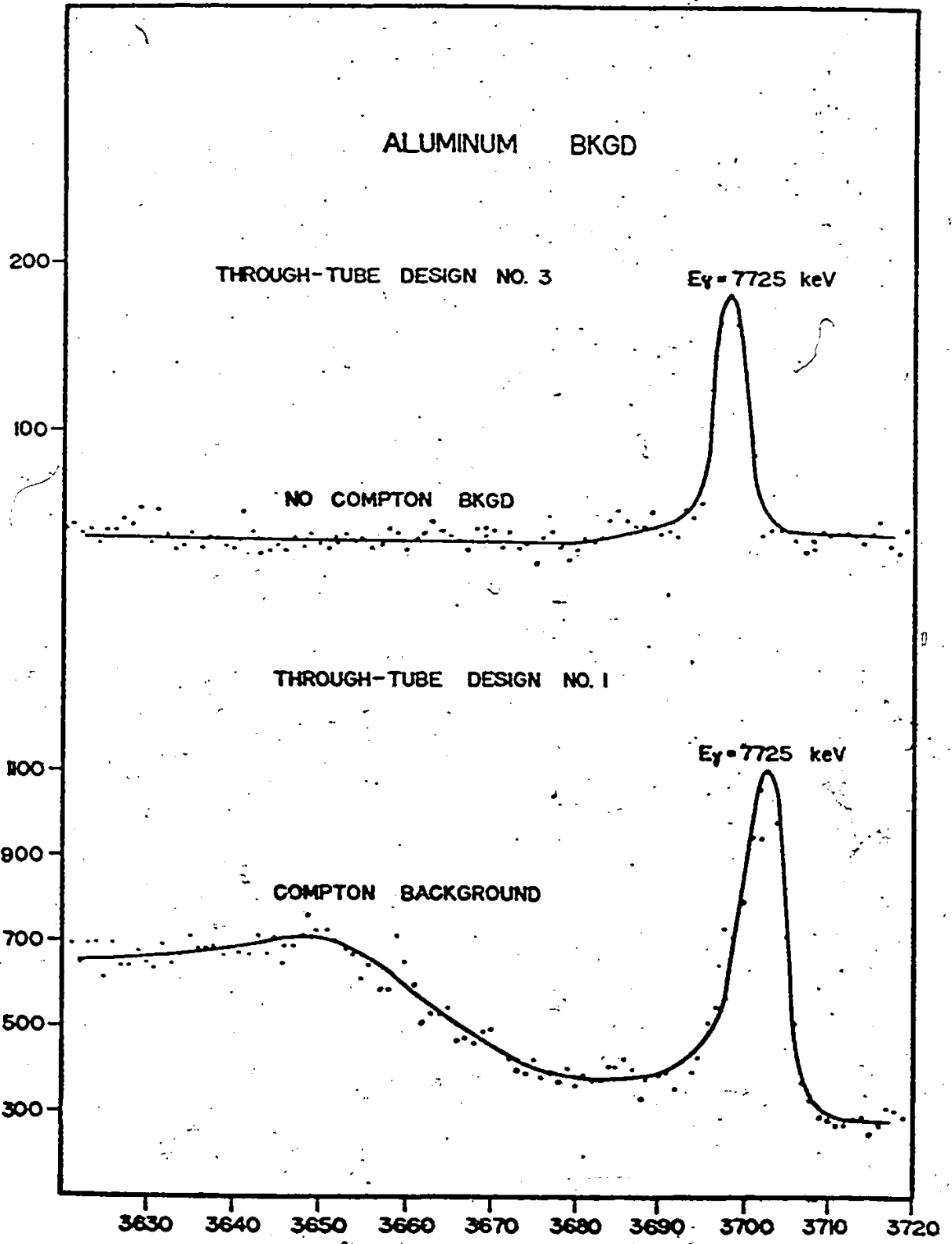
THROUGH-TUBE TANGENTIAL
IRRADIATION FACILITY



SCALE: 1:45

Figure 4.7

Comparison of Aluminum Background Obtained with TT#1 and TT#3



the convolution of the input and the response function, it never reproduces the input signal. The result of this distortion is to complicate the gamma ray spectrum and to cause masking of the low intensity gamma ray lines if not to introduce errors in the measured energies and intensities.

Closely related to the response function is the resolving power of the system. For precision spectrometry a detector with a high resolving power is desirable. This corresponds to a detection system whose response function nearly approximates a delta function.

For these experiments, a gamma ray of energy E_i is represented approximately by a Gaussian peak superimposed on a linear background. The net area of the Gaussian peak corresponds to the relative intensity while its centroid is related to its energy. If the variance about the centroid is σ^2 , then the full width at half maximum (FWHM) is 2.35σ . The variance σ^2 is characteristic of the detector being used.

To see how the detector resolution (through σ) affects the parameters of interest, consider the error in the measured centroid of the peak. A detailed derivation is shown in Appendix 3. The final result is

$$\sigma_c = \frac{\sigma}{\sqrt{A}} \left[1 + \frac{36 B_0 \sigma}{A} \right]^{1/2}$$

where σ_c is the error in the centroid, A the total count in the peak, B_0 the constant background under the peak and σ^2 , the

variance of the centroid characteristic of the detector used. To minimize the error in the centroid one needs a detector with a very good resolution, very small background contribution and large number of counts under the peak.

In choosing the detecting system used, consideration is given to the restricted interest in the primary high energy gamma rays. The detection system which tends to maximize the signal to background ratio is the Ge(Li)-NaI(Tl) pair spectrometer system.

The Ge(Li)-NaI(Tl) annulus pair spectrometer consists of a Ge(Li) detector located centrally inside an annulus of NaI(Tl) crystal. This annulus is divided optically into four quadrants. With the associated electronic logic circuitry, this system preferentially selects gamma rays which interact with the Ge(Li) detector by pair creation. A schematic diagram is shown in Fig. 4.8.

B. Ge(Li) Detector

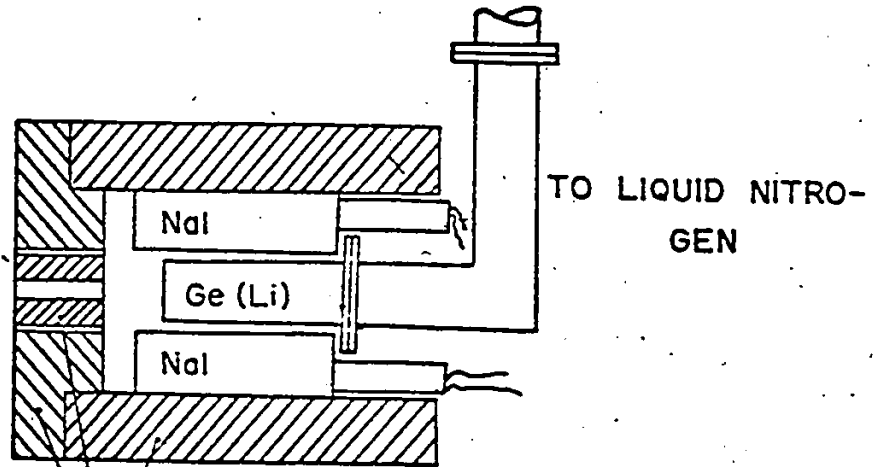
Detection of gamma rays by the Ge(Li) detector is based on the interaction processes of photoelectric effect, Compton scattering and pair production. Each of these interactions results in the transfer of energy from the gamma radiation to charge carriers. Thus the number of charge carriers liberated is proportional to the gamma ray energy deposited in the diode.

In the photoelectric effect the gamma ray is absorbed by a bound electron resulting in its ejection with a kinetic

Figure 4.8

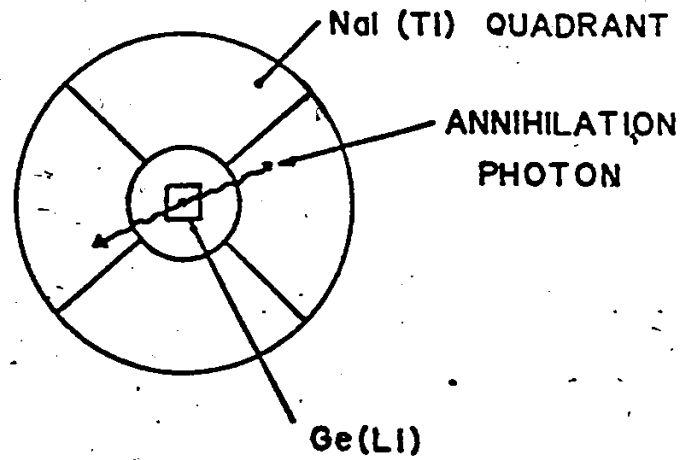
Schematic of the Ge(Li)-NaI Pair Spectrometer

Nal (TI)-Ge (Li) PAIR SPECTROMETER



LEAD

TO LIQUID NITROGEN



NaI (TI) QUADRANT

ANNIHILATION PHOTON

Ge(LI)

energy equal to the photon energy minus the binding energy of that particular electron. A negligible amount of energy is also shared by the recoiling atom. The free electron collides with other charge carriers which may also undergo further interactions.

In the Compton interaction the incident photon collides with a free electron and is scattered with lower energy. The rest of the energy is acquired by the recoiling electron. The scattered photon may interact further with other electrons. If all the photon energy is deposited in the detector by multiple interactions then the total number of charge carriers is again proportional to the original photon energy. However if the photon scattered after the n^{th} time manages to escape then only partial energy transfer is attained.

In pair production, a gamma ray with energy greater than $2M_0c^2$, where M_0 is the electron rest mass, interacts with the nucleus resulting in its disappearance and the formation of an electron-positron pair. The energy in excess of the electron-positron masses, $2M_0c^2$ is imparted to these particles as kinetic energies. A small recoil energy is also absorbed by the nucleus. By means of multiple collisions with the atoms of the material, the positron is slowed down and forms a positronium atom with an unbound electron. Subsequently the positronium atom annihilates into two photons each with energy M_0c^2 . Because the mean life of the positronium (10^{-10} sec) is small compared to the charge collection times, the annihilation photons could interact further and liberate more charge carriers.

The probability of each of these modes of interaction depends on the gamma ray energy and on the detector material. For germanium the energy dependence of the different cross-sections is shown in Fig. 4.9.

In the pair production process it is probable depending on the counter size and shape that one or both of the annihilation photons may escape and not interact any further. If one photon escapes then the energy absorbed is equivalent to $E_{\gamma} - M_0 c^2$ where E_{γ} is the photon energy. If both photons escape, then the energy absorbed is $E_{\gamma} - 2M_0 c^2$. The resulting peaks are called "single-escape" and "double-escape" peaks respectively.

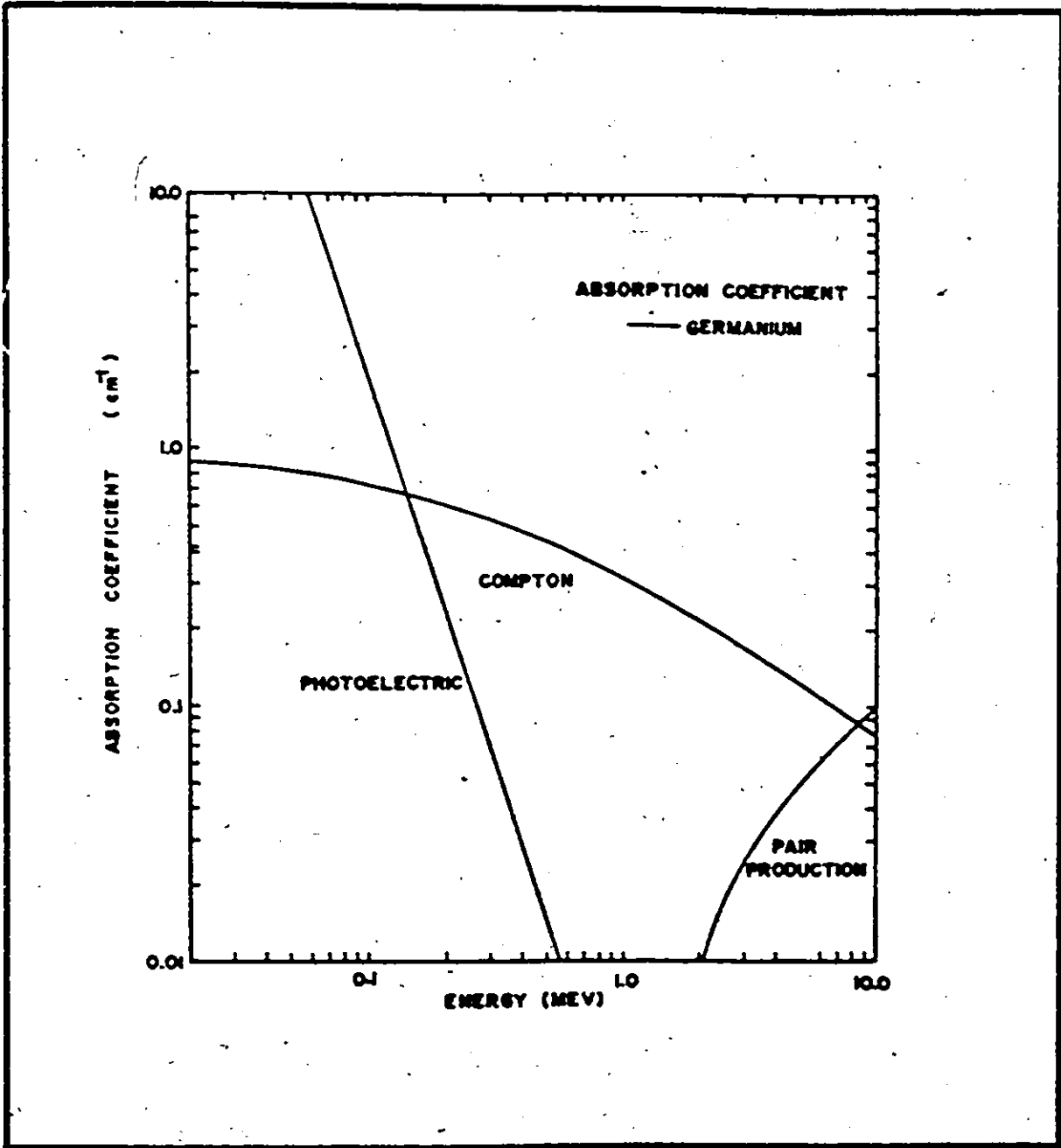
Therefore given a source of gamma rays with energies greater than $2M_0 c^2$, the spectrum will exhibit the escape peaks, a photopeak and a continuous spectrum due to Compton scattering. These peaks are approximately equally spaced in energy and are weighted according to their respective probabilities.

Additional distortion of the spectrum occurs due to other effects which result in partial energy transfer in the detector. The main causes would be the escape of high energy electrons or positrons, the trapping of charge carriers in dead zones in the counter and the escape of "bremstrahlung" radiation which is produced in the deceleration of the charge carriers. These processes contribute additional continuous background under the peak.

The detector used is gallium-doped germanium with lithium drifted at the appropriate surfaces. It is a cylindrical closed-end coaxial detector with an active volume of

Figure 4.9

Energy Dependence of the Photoelectric, Compton Effect and
Pair Production Cross-Section in Germanium.



25 cc. The p-region is gallium-doped germanium, the n-region is a Li rich alloy and the intrinsic region is formed by exactly compensating the gallium-doped region with lithium. At 1800 volts reversed bias, the leakage current is 1 nanoampere.

The shape of this detector is ideally suited for enhancing the escape of both annihilation photons. Therefore the second escape peak will dominate over the photopeak or the single escape peak.

C. NaI(Tl) - Ge(Li) Pair Spectrometer

From the previous discussion the response function of the Ge(Li) detector is complicated by the probability of different modes of interaction for a given gamma ray. If the source emits gamma rays of different energies, the resulting spectrum will be a superposition of the response function for each of them. The resulting spectrum will be so complex that one may not be able to unfold it without large uncertainties in the gamma ray energies and intensities. In some cases, especially in the low energy portion, the resulting background may be so high as to mask the existence of low intensity lines. It is also possible that a line may just overlap with one of the escape peaks or may even be under it. In such a case the measured parameters will be very unreliable.

The photopeak and the escape peaks are actually redundant in that they contain the same information. If one can discriminate between the different interaction processes and select only one, then a simpler response function which will yield all the information of interest will be obtained.

The NaI(Tl) - Ge(Li) pair spectrometer is such a device. It consists of an annulus of NaI(Tl) crystal which is optically split into four quadrants. The outside diameter is 15.2 cm while the inside diameter is 7.6 cm. To each section of NaI(Tl) crystal is a photomultiplier whose high voltage can be varied. When a photon interacts with the NaI(Tl) crystal, light is emitted which is detected by an optically coupled photocathode. A chain of dynodes accelerates the photoelectrons which multiply as they collide and liberate more electrons from the succeeding dynodes. The final output is taken from the anode connection.

The operation of the NaI(Tl) - Ge(Li) pair spectrometer can be understood by considering a gamma ray which creates a pair in the Ge(Li) counter. Upon slowing down of the positron, it forms a positronium atom. Subsequently it annihilates and two photons each of energy M_0C^2 are created. By conservation of momentum these photons will be directed in opposite directions. Assuming that they both escape, two photons of energy M_0C^2 will be simultaneously detected by a pair of opposing NaI(Tl) quadrants. The amount of energy deposited in the Ge(Li) counter will correspond to the double escape peak. The simultaneous detection of two 511 keV photons in opposite quadrants and a corresponding gamma ray in the Ge(Li) detector can therefore be used to select the double escape peaks. For a gamma ray of energy E_γ , the resulting spectrum will consist of a peak whose centroid will be at $E_\gamma - 2M_0C^2$ superimposed on a

background which extends to zero energy. The background is due to multiple partial energy transfer in the detector.

It is quite obvious that the response of this spectrometer is cleaner and easier to interpret. However, it has the limitation that it cannot detect photons whose energies are lower than the pair production threshold. In this case the logic circuitry is modified to operate in the anti-coincidence mode to enhance those events resulting in full-energy transfers in the Ge(Li) counter.

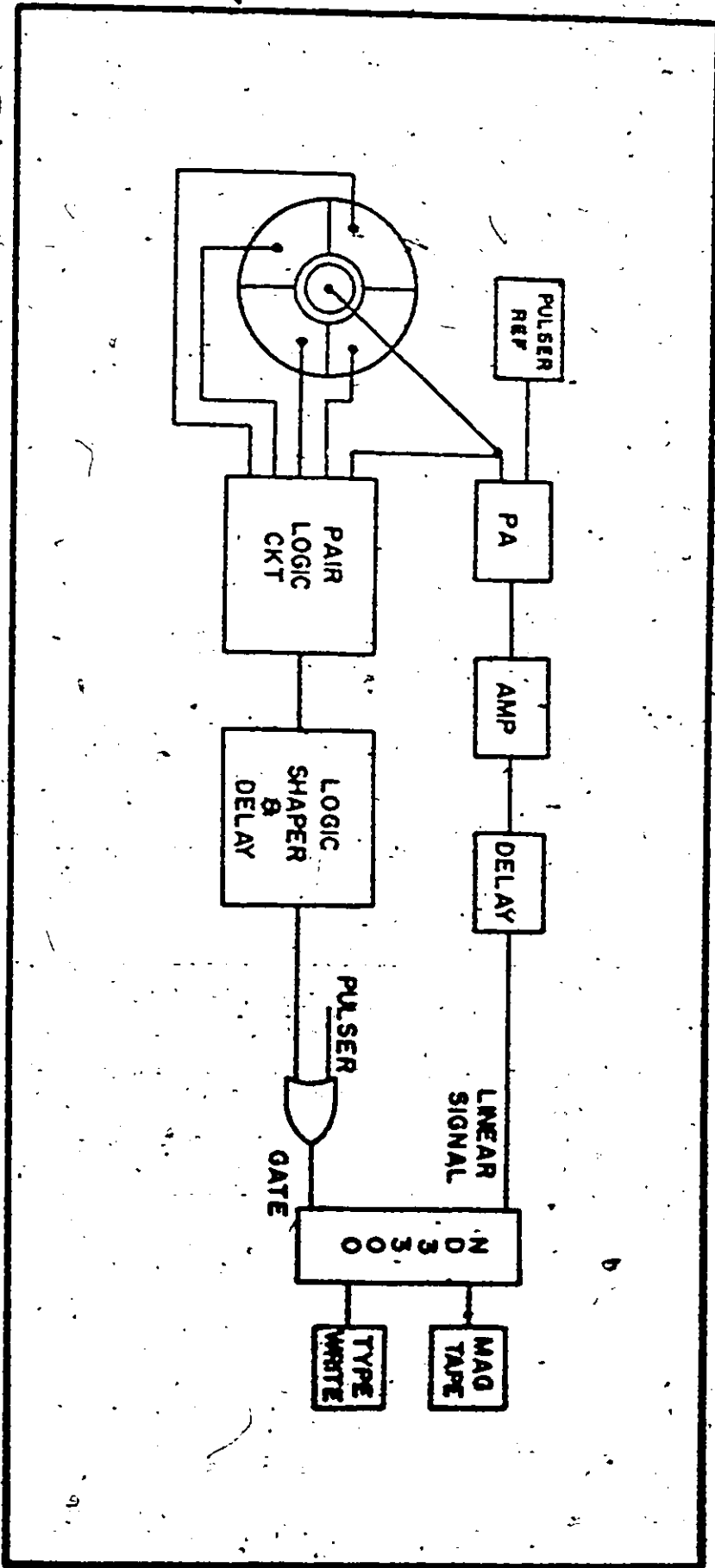
D. Electronic System

A simplified schematic of the electronic system is also shown in Fig. 4.10. Functionally the system may be subdivided into linear and logic signal branches. The linear branch performs the function of detecting, amplifying, and filtering the pulse from the Ge(Li) counter and transforming it into a signal acceptable to the multichannel pulse height analyzer. The logic circuit inspects the pulses from the Ge(Li) counter and the NaI(Tl) annulus and ensures that proper conditions are satisfied by events accepted for amplitude analysis.

The integration of the charge carriers liberated by the incident photon in the Ge(Li) counter results in an output voltage pulse. When the detector output is connected to a charge sensitive preamplifier, the resultant signal V_o is proportional to the number of total charges collected, independent of the detector bias voltage.

Figure 4.10

Overall Schematic of the Detection System



A charge sensitive preamplifier consists of an operational amplifier with a capacitive feedback. Provided that $G_o C_f \gg C_t$ where G_o is the open loop gain, C_f the feedback capacitance, C_t the detector capacitance (dependent on bias voltage) plus stray capacitance, the preamp output voltage $V_o = Q/C_t$ where Q is the total charge collected.

The preamplifier output is coupled to the amplifier for amplification and waveshaping. The pulses to the amplifier input are long and since the signal to noise ratio decreases with pulse duration it is necessary to differentiate them to an optimum pulse width. This yields a monopolar pulse. Double differentiation yields a bipolar output. Either shape is acceptable to the analyzer, however the overall resolution may be better for one or the other depending on the rate of the incoming signals. Since detailed discussion of waveshaping techniques and amplifier performance can be found in many texts, (Fa 65, Ma 69) it will not be pursued further in this discussion.

For these experiments an overall energy resolution of 12 keV at 10.8 MeV is obtained by operating in the bipolar mode. A Tennelec TC135 FET charge sensitive preamplifier and a Tennelec TC200 amplifier are used. The amplified output is coupled to an ORTEC 427 delay amplifier for timing adjustment between the linear and the logic signals. The maximum input to the analyzer is 10 volts corresponding to the maximum gamma ray energy.

There are five input signals to the logic circuit - one from each of the four quadrants and one from the second stage

of the TC200 for signals from the Ge(Li) counter. The anode pulse from each quadrant is fed to a single channel analyzer with a fixed window setting centered at 511 keV. The logic pulses from two opposite quadrants are aligned in time and coupled to an "AND" gate. Then the AND outputs of each pair of opposite quadrants are fed to an "OR" gate. Finally, the Ge(Li) detector signal, derived from the second stage of the TC200 amplifier and fed into a low level discriminator, is coupled with the final NaI(Tl) detector logic pulses into an "AND" gate. This triple coincidence pulse (Ge(Li) detector signal coincident with 511 keV pulses from two opposite NaI(Tl) quadrants) is then used to gate the linear signals that will be analyzed.

The logic circuit which has all the above functions is made up of integrated circuits and uses comparators, J-K flip-flops and nand gates. A comparator is a high gain differential amplifier which changes the state of its output from 0 to 4 volts or vice versa when the input signal crosses a reference voltage. The reference voltage is usually made variable and can be any dc voltage source. The width of the comparator output depends on the width of the input pulse and is equal to the points where the reference voltage equals the input voltage.

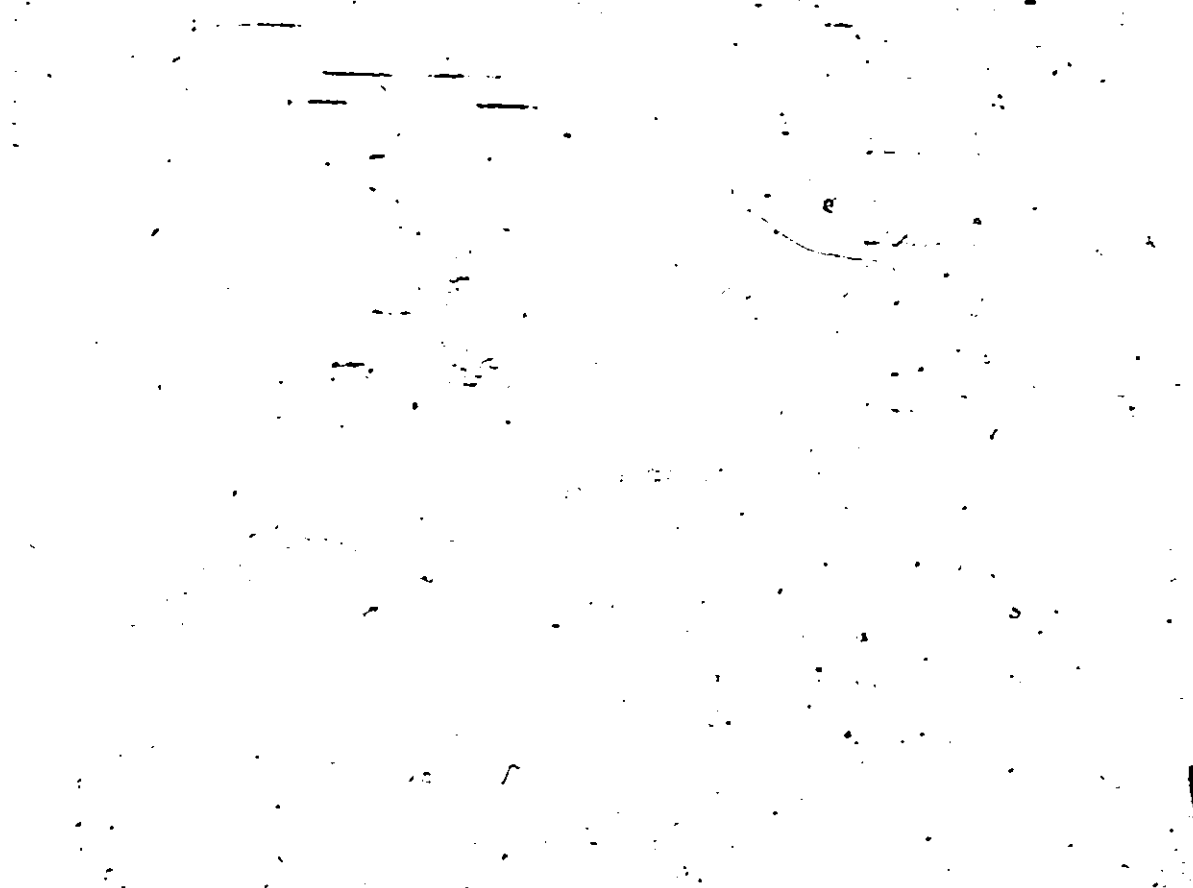
A schematic diagram for the single channel analyzer for each quadrant is shown in Fig. 4.11. The anode pulse is "differentiated" with an RC network and then branched out to three μ A710 comparators. The timing comparators (upper most)

Figure 11a

Schematic of the Single Channel Analyzer Used for Each
Annular Quadrant

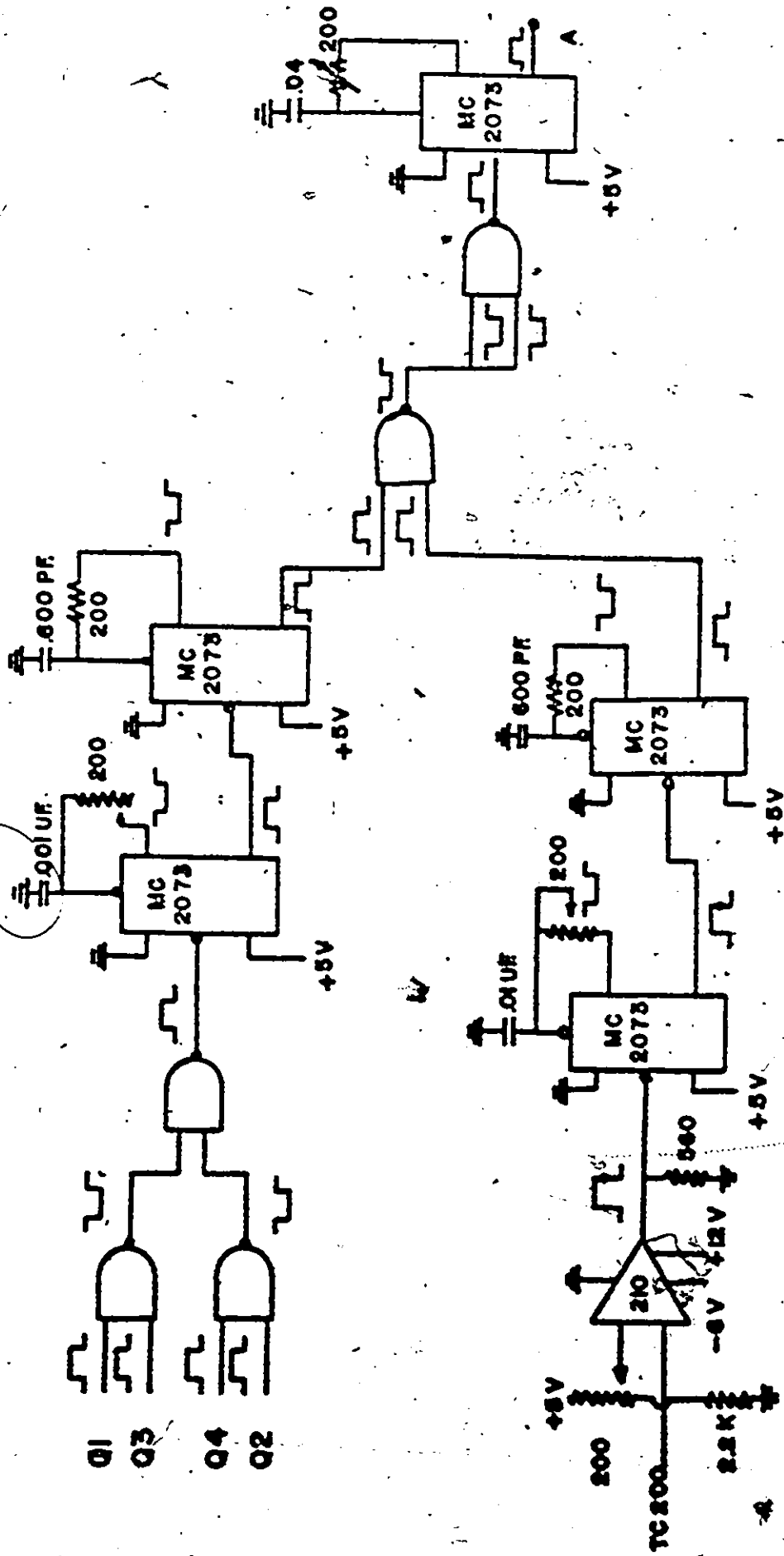
Figure 4.11b

Overall Schematic of the Electronic Logic Circuitry



COINCIDENCE

ELECTRONICS



has its reference voltage just above noise. It acts as a time marker for any photon detected by the NaI crystal. The lower energy level comparator (middle) discriminates against photons with energies less than 511 keV and the upper energy level comparator discriminates against photons with energies greater than 511 keV. Together these two comparators defined a finite width of photon energy and are usually adjusted to give ΔE from 50-100 keV. Since the differentiated anode signal has a rise time of about 25 ns, the time marker is out of time with the energy level comparators. A time delay of 600 ns is inserted in the path of the timing comparator output by means of an RC network and a J-K Flip-flop (MC2073). The same type of flip-flops are also used to vary the width of the logic pulses. When the output of these three comparators are in time a 50 ns pulse results indicating that a photon of energy $(M_0c^2 + \Delta E)$ is detected.

The AND and OR logic functions are obtained by properly interconnecting 7400 TTL nand gates. Thus when two opposite quadrants simultaneously detect 511 keV photons the system of nand gates which are doing the "AND" function will give a single logic signal. Unless it is a four-fold coincidence the signal from each pair of quadrants will not be in time. The "OR" circuit ensures that each pair event be processed further.

The detection of two 511 keV gamma rays in opposite quadrants is not necessarily the result of the pair production and double escape process at the Ge(Li) counter. Pair

production in materials external to the detector, particularly the chamber walls, results in signals satisfying logic function requirements. Without demand for a triple coincidence with the Ge(Li) detector the linear gate will be opened unnecessarily.

The time resolution curve between two opposite quadrants is shown in Fig. 4.12. A typical single channel analyzer window obtained by using a Na^{22} source located in the central axis of the annulus is shown in Fig. 4.13.

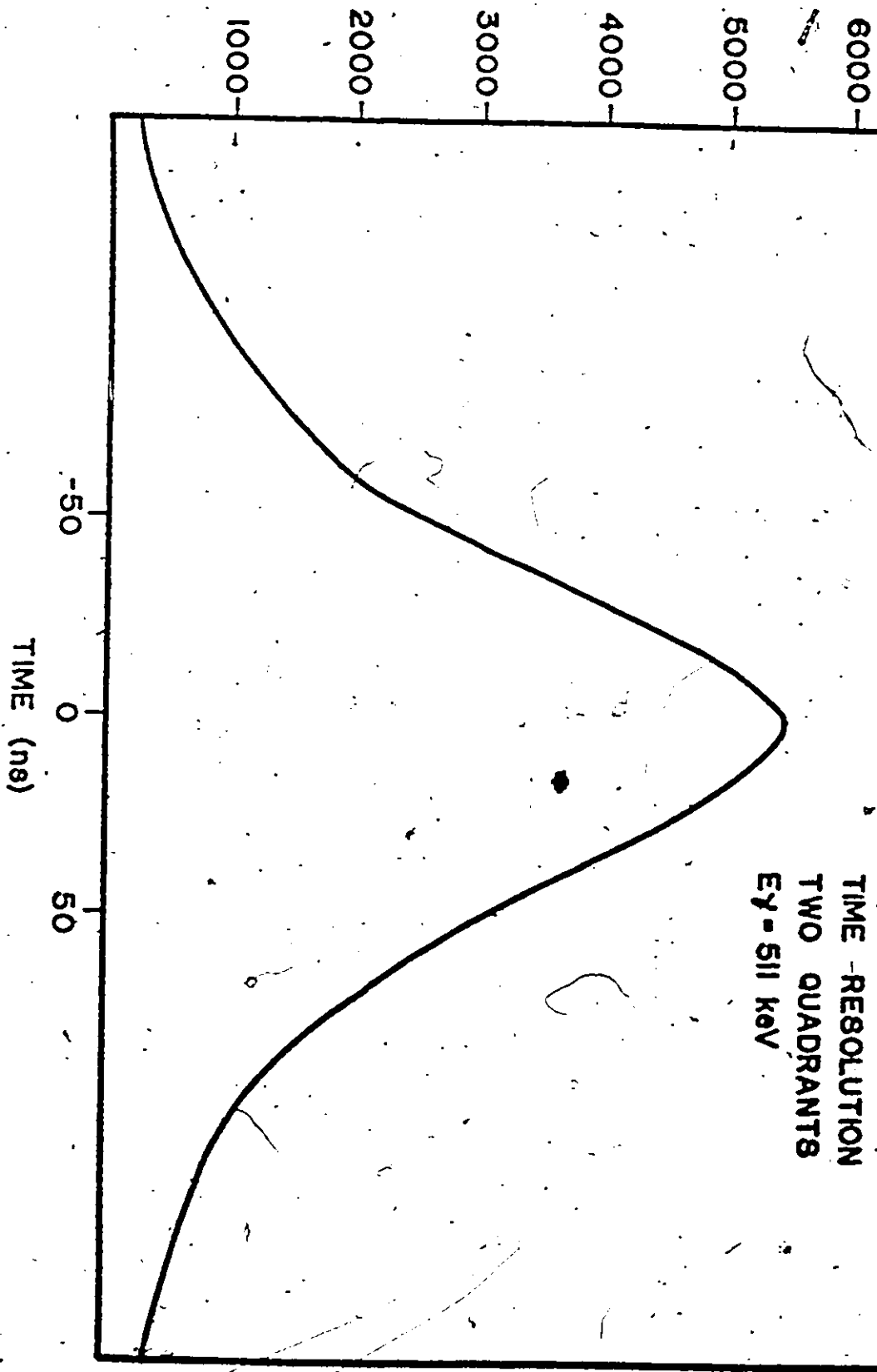
During an experimental run there is always the possibility of changes in the performance of the electronic circuitry due to fluctuations in ambient temperature and humidity which affect the characteristic of the component parts. The result of these changes may be characterized by variation in the gain and a drift in the zero energy channel. These effects will be observed as shifts in peak centroids, resolution broadening or a combination of both. Since true peak centroid shift due to capture in the keV region is also being measured, it is essential that the system be as stable as possible not only during a given run but throughout all the runs (i.e. different sample filter thicknesses).

The problem of zero and gain changes can be dealt with in two ways. The simplest way would be to accumulate data for short periods of time and record it in magnetic tape. The time of data accumulation should be short enough to avoid noticeable shift. In order to ensure internal stability

Figure 4.12

Time Resolution Curve Between Two Opposite Quadrants

COUNTS



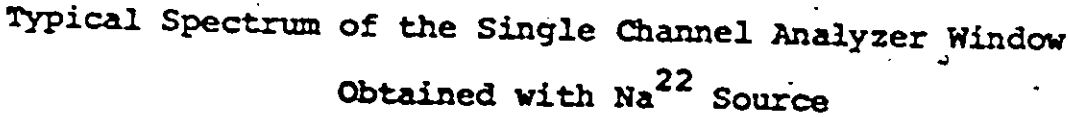


Figure 4.13

Typical Spectrum of the Single Channel Analyzer Window
Obtained with Na²² Source

TYPICAL SCA WINDOW
USING Na^{22} SOURCE

511 keV

1000

800

600

400

200

0

COUNTS

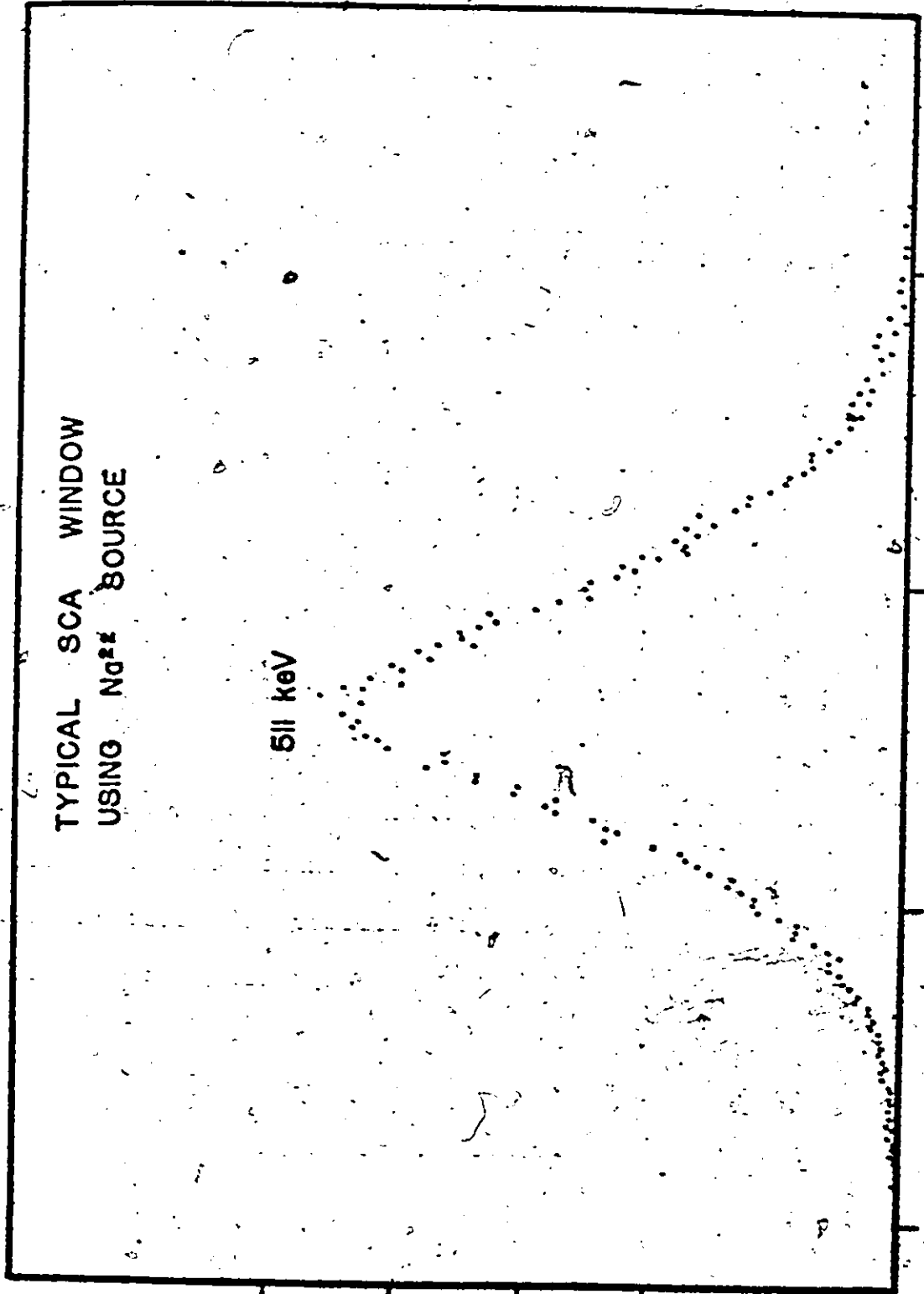
150

200

250

300

CHANNEL NO.



not only in any given spectrum but also between several spectra, it is required to have at least two common reference peaks which will serve to monitor the zero and gain of any particular spectrum. The spectra can then be aligned with reference to the common peaks by use of a computer.

This method has the advantage that if the analyzer malfunctions for whatever reason, only a small portion of the accumulated data is lost. However, it has the disadvantage of requiring more magnetic tapes than is actually necessary and the need for an external computer to do the necessary checking and correction of data.

The other method would be to employ an automatic detection and correction of both gain and zero drifts during the run. This is done by using a specialized computer which senses the positions of reference peaks and makes instantaneous correction when changes are observed. The device that does this is called a stabilizer and is incorporated with the pulse height analyzer.

The reference pulses, one at the low energy end of the spectrum to indicate zero drifts, another at high energy to indicate gain change, can be obtained either from a radioactive source which yields relatively strong peaks of the proper energy or from an ultra stable pulser. Since the available calibration sources yield only low energy gamma rays compared to the region of interest (up to 8 MeV) an ultra stable reference pulser designed by Strass et al^(St 68) was built and used throughout these experiments.

This pulser used solid state components. A block

diagram is shown in Fig. 4.14. An oscillator flip-flop combination generates two square waves which are 180° out of phase. These are passed through waveshaping circuits which in turn give out pulses similar to the detector output and which are compatible with the requirements of the charge sensitive amplifier. To attenuate the signal from each branch for amplitude variation, separate 7 bit R-2R ladder attenuators are used. The signals are then mixed to yield two pulses of different amplitudes.

The stability of the output pulses is determined by the reference voltage supplies, the attenuators and the transistor switches which are especially chosen to meet the required stability requirements. Furthermore, in order that the response of the ADC will be the same for the pulser and the detector pulses, the proper rise times and fall times are carefully matched. The performance test^(St. 68) showed a gain and zero drift of ± 20 ppm/day when a stabilizer is locked on the pulser peaks.

The pulser frequency is variable to suit the counting rate. Tag pulses generated in coincidence with the reference pulses are also available for gating or coincidence purposes. The polarity of the pulses can also be changed to suit the output pulse of any given Ge(Li) detector.

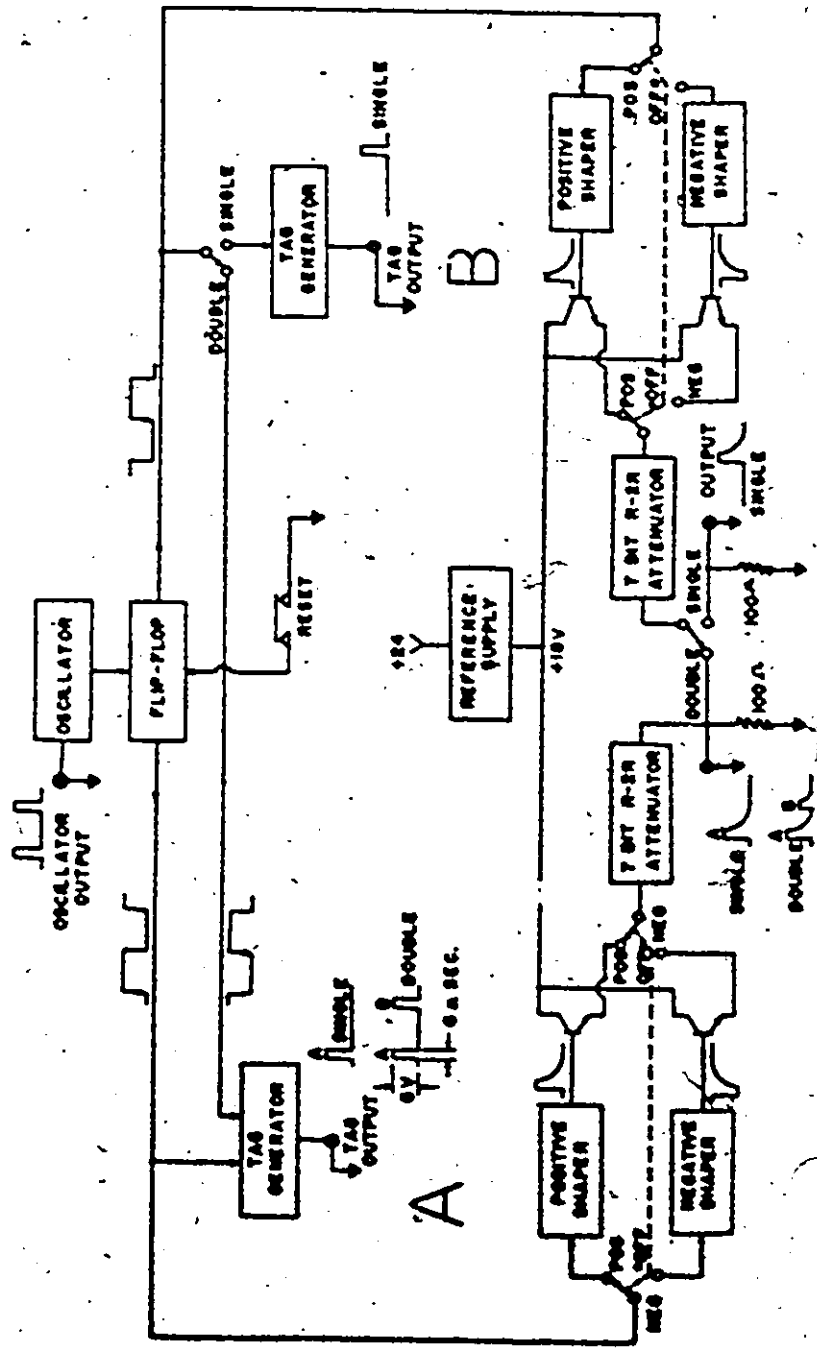
The pulser output is coupled to the test input of the preamplifier. It is then mixed with the linear detector signal and processed in the same way. Since the reference pulses cannot activate the logic circuit, the tag pulses are "OR"ed with the logic circuit output in order that the pulser peaks be analyzed in the same fashion as the proper detector signals.

Figure 4.14

Block Diagram of the Reference Pulser

==
==

REFERENCE PULSER



The stabilizer is locked on the pulser peaks by means of switches which select the address or channel number of the peak centroid. A window which specifies the channel width for correction and the drift rate compensation are also set.

The stabilizer operates by calculating the median of the window width specified. Depending on the count rate and the drift rate compensation setting, the stabilizer compares the centroid setting with the calculated median and makes gain and zero corrections in order that the median and the centroid setting stays the same during the run. For pulser peaks much stronger than the background or for a flat background the centroid of the pulser and the median of the window will be identical. However if the background is asymmetric and is comparable to the pulser intensity, then the stabilizer will ensure that the median will correspond to the address as specified by the switches. In this case the median is not identical to the pulser centroid. Although the gain and zero will not be changed throughout the experimental run, the gamma ray peaks may be shifted relative to other runs where the median of the window width are not the same. A discussion of the performance of the stabilizer in these experiments will be discussed in the section on data analysis.

The ND3300 multichannel pulse height analyzer is a specialized computer which sorts the incoming linear signal according to their amplitudes. The whole system may be subdivided into three main functional groups - pulse height

measurement, data acquisition, and data output. Pulse height measurement is accomplished by one or more analog to digital converters of the Wilkinson type. The input pulse is integrated until the maximum peak height is sensed at which time a linear discharge is initiated. During the linear discharge the pulses from a clock with a fixed frequency of 16 megacycles is counted until the voltage across the integrating device reaches the zero reference voltage of a comparator. The number of clock pulses is proportional to the pulse height and correspond to a particular address or channel number. The data acquisition section consists of a magnetic core memory and several registers. Its function is to sort the digital information from the ADC and store it in the proper channel number. Finally the data output section enables the transfer of the memory content to a magnetic tape, a typewriter, or a plotter.

For a 12-bit conversion gain, the pulse heights are sorted into 4096 channel numbers. The number of events that can be accumulated in a particular address is 2^{18} corresponding to a word length of 18 bits.

When the data is written on a magnetic tape each spectrum can be identified with tagwords and can be separated by end of file marks. The tagword and data are written on the tape as follows: The tagword is written first as two 36 bit words. The data record is written next and this is followed by two additional 18 bit words written to satisfy the Parity Redundancy Check. Each memory dump is recorded with a density of 556 bits per inch.

The data which is now on tape is ready for analysis which is done by using a CDC 6400 computer to calculate the different parameters such as peak centroids and relative intensities.

B. Experimental Procedure

The final system as described above evolved after several experimental runs. The problems associated with background radiation, electronic performance, sample size and geometry have all been considered in the present design. The data presented are obtained from runs made using the optimum design.

The cobalt samples were of two kinds. For thin B^{10} filters a smaller amount of cobalt is used to ensure that the count rate of all samples was about the same. For these runs cobalt powder with 99.99% purity was used. The powder is contained in thin-walled (1/32") capsules 1/2" ID and 1-1/2" long. The amount of cobalt in the capsule can be varied by mixing it with graphite powder if necessary. The same sample volume was used to maintain the same geometry which is equivalent to maintaining the same detector efficiency. For thick filters high density cobalt was used to increase the amount of sample for the same sample volume. For these runs solid pieces of cylindrical cobalt rods 1/2" outside diameter and 1" long were used. These rods are prepared by melting 99.99% purity cobalt pellets. Longer rods can be used, however self-shielding effects become significant so that

there is little gain by doing so. For the cobalt samples nominal B^{10} thicknesses are 0", 1/8", 3/16", 1/4", 3/8", 1/2" and 5/8".

Manganese samples of 99.99% purity were prepared by containing the powder in thin-walled carbon capsules 1/2" ID by 1-1/2" long. Because of the physical properties of manganese it is difficult to prepare samples in solid cylindrical form. Nominal B^{10} filter thicknesses used are 0", 1/8", 3/16", 1/4", 5/16", 7/16", and 1/2".

The nominal B^{10} thicknesses are not very accurate because the actual amount of B^{10} used depends on how well it is packed during the sample preparation. To get the actual amount of B^{10} filter in a given sample, it is necessary to weigh each component of the sample assembly.

The B^{10} powder is obtained from USAEC, Oak Ridge. It has the following isotopic composition: B^{10} 94.3% B^{11} , 3.4%.

Although electronic stabilization is employed through the whole experiment, the gain and zero of the spectrum is monitored frequently. The accumulated data was written on magnetic tape every 12 hours and rough visual comparison with the previous data was made. Furthermore to ensure that correction for gain and zero drifts can be made if they occur, intensity and energy calibration was made before and after every sample run.

Energy and intensity calibration was done by using a sample consisting of melamine powder ($C_3H_6N_6$). The calibration peaks are the capture gamma ray lines of nitrogen, the absolute intensities and energies of which are well known and

determined with sufficient precision. The melamine powder is contained in an thin-walled carbon capsule and carbon container identical to that for Co and Mn

For the cobalt and manganese samples, the time for data accumulation varies from 1-4 days. The calibration run is typically 36 hours. The total running time excluding the feasibility studies which extended for a few months, is about 6 weeks.

CHAPTER V

DATA ANALYSIS

This section describes how the parameters gamma ray energy, intensity and energy shift are obtained from the raw data. The parameters are later used in the discussion of results to interpret the experimental observations with regard to the theoretical predictions.

To determine the gamma ray energies the centroids of the gamma ray peaks in the sample spectrum are found. The parameters in the equation which relate the gamma ray energy and the gamma ray peak centroid are obtained from the nitrogen calibration data.

The extraction of the absolute gamma ray intensities involves four steps. Firstly, the net peak area is determined. Secondly, a relative efficiency is obtained using the known intensities of the calibration gamma rays. Thirdly the relative intensities are calculated from the efficiency curve. Lastly these relative intensities are converted to absolute intensities by proper normalization procedures.

The measurement of a centroid shift due to high energy resonance capture is more difficult. This is because being a small effect, it cannot be easily distinguished from shifts caused by instability in the detection system. The difficulties and problems encountered with the determination of this parameter are discussed.

For illustrative purposes the analysis of the cobalt spectrum obtained with 5/8" boron-10 filter will be considered in detail.

1. Determination of Gamma Ray Energy

The first step in this analysis is the determination of the gamma ray peak centroids. Three different methods were tried to check the dependance of the results on the method used.

A. Method 1 - Gaussian Fit

Here a non-linear least squares fit of the data to a Gaussian curve superimposed on a linear background is made. Thus

$$y(X_i) = a + bX_i + \sum_j C_j e^{-d_j (X_i - X_{0j})^2}$$

where $y(X_i)$ is the number of counts in channel X_i , X_{0j} is the peak centroid of the j^{th} peak, C_j , d_j are parameters related to the peak height and FWHM, a , b are parameters related to the background contribution. The sum indicates a multiplet which may not be well resolved. A CDC 6400 computer is used to process the computer code. Typical results after fitting the ground state and a doublet (line 6 and Boron line) are shown in Figs. 5.1 and 5.2. The dotted lines indicate the best fit functions.

A similar procedure is followed to determine the peak centroid of the nitrogen lines in the calibration spectra which were obtained before and after each sample run.

Figure 5.1

Co^{60} Ground State Line Showing the Curve Obtained with
Gaussian Fit (Solid Line)

Co-60 GROUND STATE
(5/8 INCH FILTER)

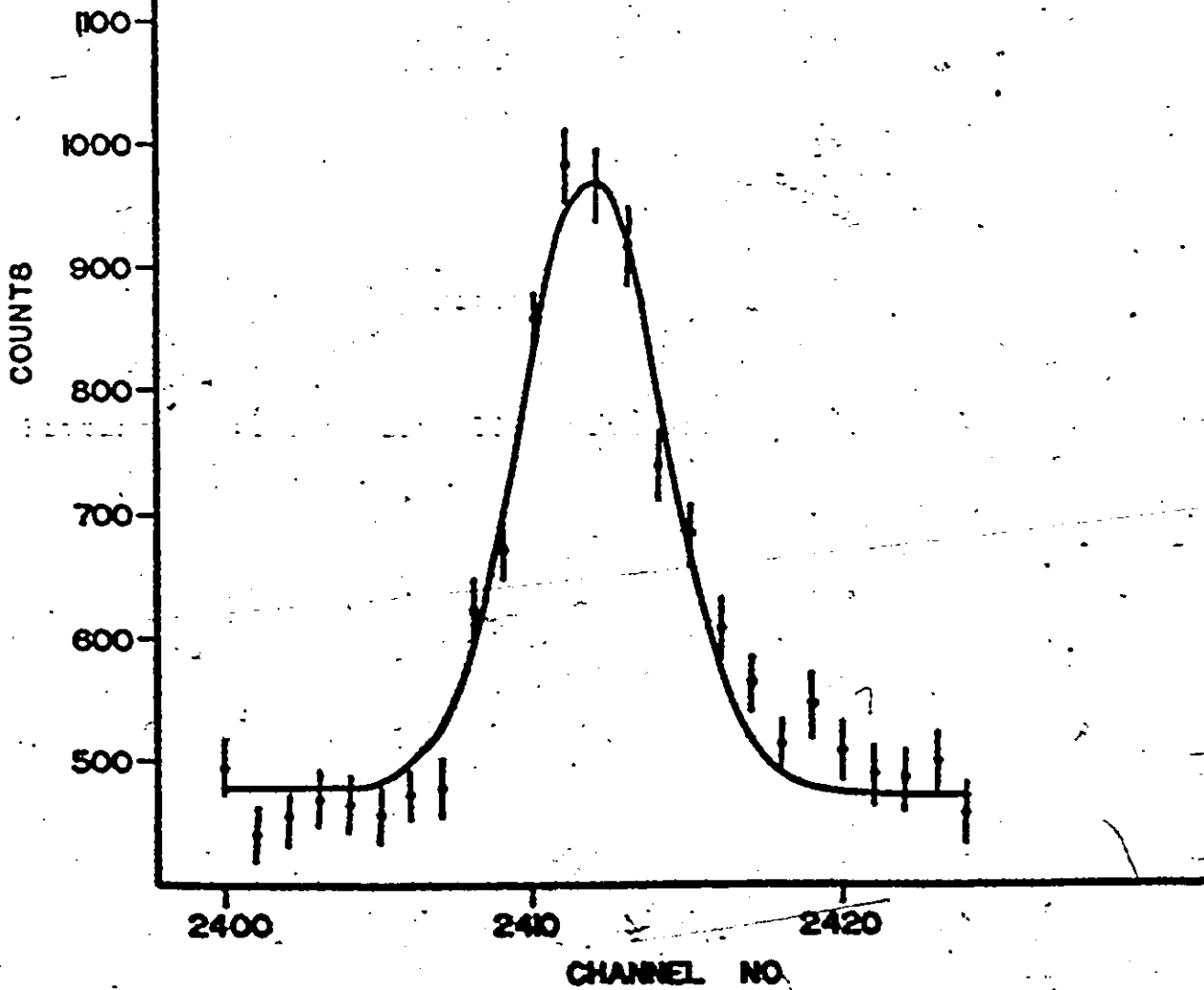


Figure 5.2

Fitting a Doublet (line 11^c) with Gaussian Curve

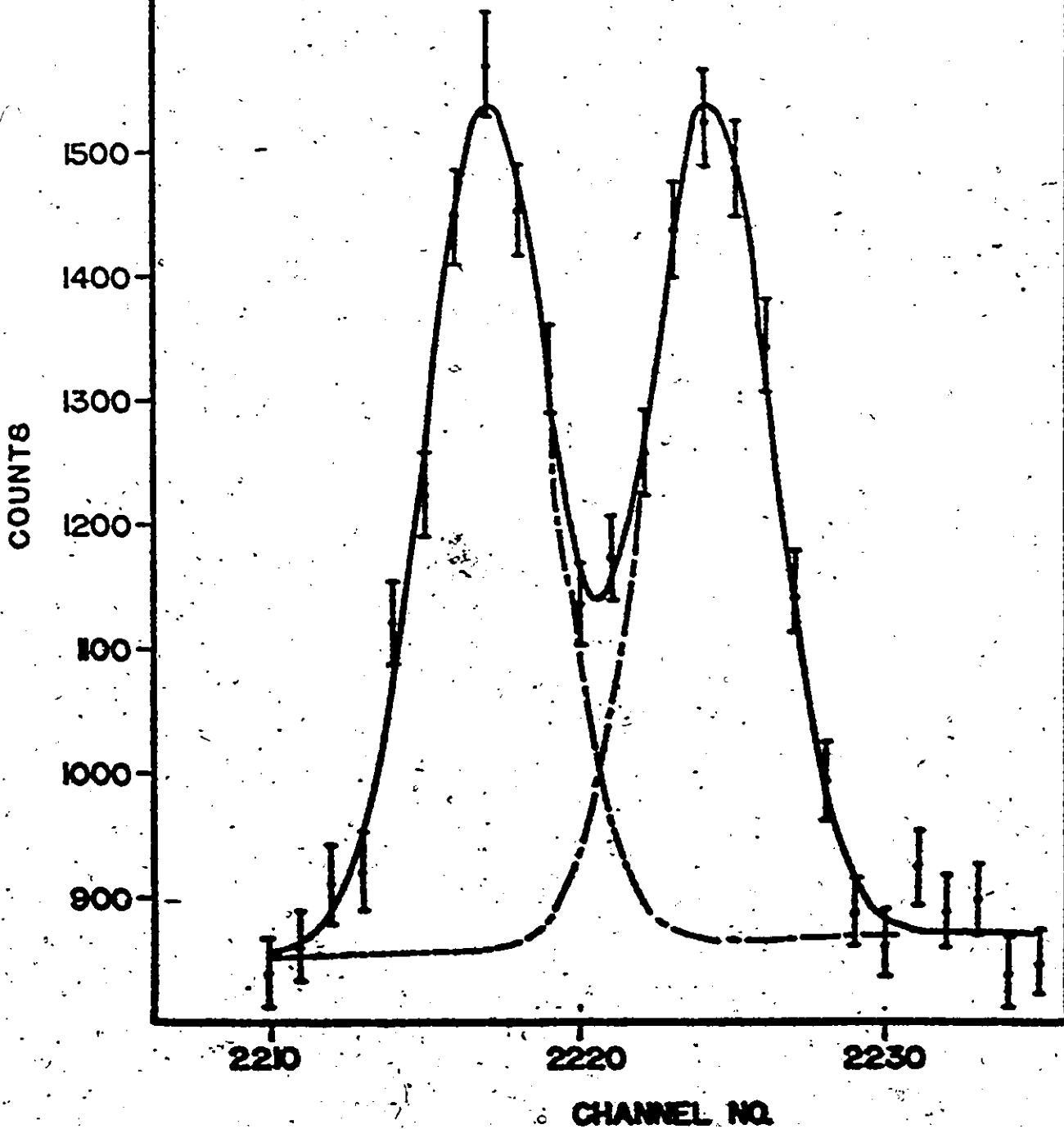
Co-60

LINE NO. 6

E=6985 keV

BORON LINE

E=7006 keV



The parameters obtained with the Gaussian fit are accurate. For the centroid calculations the errors are usually in the range .01-.05 channel for reasonable symmetric and strong peaks. The statistical errors are of the same order of magnitude.

B. Method 2

In this method no assumption of a line shape is made. The definition of a centroid is employed directly.

Hence

$$\langle x \rangle = \frac{\int x [Y_T(x) - Y_B(x)] dx}{\int [Y_T(x) - Y_B(x)] dx}$$

where $Y_T(x)$ is the total count in channel x and $Y_B(x)$ is the background contribution in the same channel. It is assumed that the background component varies linearly across the peak. As long as a peak is not sitting on top of a Compton edge or on an unobserved weak contaminant line the above approximation should be adequate.

C. Method 3

This method uses a zero area fold-in function to extract the signal from the background contribution (Ro 72). Very briefly a correlation spectrum is obtained by folding in a proper function which may approximate the line shape. It is shown that for a slowly varying background component the correlation spectrum contains only the signal content.

Thus if $C(X)$ is the correlation spectrum, $F(X)$ is the correlator, $S(X)$ is the actual signal of interest, and $B(X)$ is the background then

$$\begin{aligned} C(X) &= \sum F(X) [S(X) + B(X)] \\ &= F(X)S(X) \end{aligned}$$

since $\sum F(X)B(X) = 0$

The results of using the above methods in determination of the centroids show that Method 2 and 3 differ from Method 1 by $\pm .05$ and $\pm .09$ channel respectively for reasonably isolated peaks of comparable statistical accuracy. Thus the peak centroid calculation is not very sensitive to the method used. For energy determination any of the above methods is actually sufficient since the uncertainty in the calibration energies is larger than this:

Knowing the centroids of the nitrogen lines and using the results of Marion^(Na 68) the parameters which relate the energy and channel number are determined by making a least squares fit of the data to the form $E_i = a + bC_i + cC_i^2$ where E_i is the known gamma ray energy, C_i is the peak centroid and a, b, c are the unknown parameters.

2. Determination of Gamma Ray Intensity

A. Relative Intensity

The first step in the calculation of the relative intensities is to find the net count under the peaks. The

approach taken is to use the true line shape in the calculation of the net peak area. Consider the i^{th} peak. If N_{Tij} is the total count in channel number j and N_{Bij} , the background contribution, then the net area A_i is

$$A_i = \sum_j (N_{Tij} - N_{Bij}) = \sum_j N_{Tij} - M_i \langle N_B \rangle$$

where the summation is over the peak width M_p channels and $\langle N_B \rangle$ is the average background peak component. Since N_{Bij} is not known for all the channel number j , $\langle N_B \rangle$ is approximated by taking the average count over a reasonable number of channels M_B located just outside the peak width. The statistical error in the net area is approximated by

$$\begin{aligned} \sigma_{A_i}^2 &= \sum_j \sigma_{N_{Tij}}^2 + M_p^2 \sigma_{\langle N_B \rangle}^2 \\ &= \sum_j N_{Tij} + \frac{M_p^2}{M_B^2} \sum_k (N_{Bik}) \\ &\quad \text{(inside peak)} \qquad \qquad \text{(outside peak)} \end{aligned}$$

The relative efficiency curve shown in Fig. 5.3 is obtained by using the data from all the nitrogen calibration runs and the nitrogen intensities (^{68}Ga). If I_i is the intensity of the i^{th} nitrogen gamma ray, the relative efficiency at energy E is $\epsilon_{Ri} = \frac{A_i}{I_i}$. A curve of the form $e^{A+B E + CE}$ is fitted to the data points to get the relative efficiency as a function of energy.

Since the variation of the intensity of a gamma ray with respect to the filter thickness is of interest it is necessary to reduce the relative intensities to absolute values. This is done by normalizing the relative intensities to the known absolute values (Wa 68, Co 68). The absolute intensities are calculated from the net peak areas by the following relationship

$$I_{\gamma i} \text{ (photons/1000 n) } = k \left(\frac{A_i}{E_{Ri}} \right) \frac{1}{N_c}$$

where N_c is the total relative intensities of all the gamma rays whose energies are greater than an arbitrary value such that most of the primary gamma rays are included, and k is the sum of the absolute intensities of all gamma rays above the same energy threshold. Since the absolute intensity $I_{\gamma i}$ is related to the relative intensity I_{Ri} by a constant then $I_{\gamma i} = k I_{Ri}$. The value of the constant can be evaluated by summing up the intensities as that $k = I_{\gamma i} / I_{Ri}$.

The assumption that k is a constant for all the lines in each of the measured spectra is justified by the fact that it is proportional to the total gamma ray width Γ_γ . Since Γ_γ is a sum of widths which follows mainly the Porter-Thomas distribution it obeys a very narrow distribution which in the limit is a constant.

3. Determination of Centroid Shift

It was mentioned previously that when a neutron of kinetic energy T_n is captured the resulting excitation energy is $E_x = S_n + T_n$. Thus for a given gamma ray, the transition energy will increase as the boron filter allows higher energy band of neutrons to be captured in the sample due to higher energy resonances. Therefore a measure of the partial capture cross-section can be obtained by closely examining the centroid shift in the gamma ray peak. For the cobalt and manganese samples the dominant resonances are separated by at most a few keV. The maximum shifts expected relative to the no B^{10} filter spectrum are therefore of the order of this magnitude.

The main problem encountered with the determination of a gamma ray peak shift is that electronic instabilities resulting in gain and zero-energy channel changes produce similar effects. It is therefore necessary that the gain and zero are as stable as possible and that if this cannot be reasonably achieved one must be able to monitor these effects so that they can later be corrected. This is the main reason for using an ultra-stable pulser as a source of reference peaks for the electronic stabilizer. As another monitor for any gain and zero changes calibration runs with nitrogen in the form of melamine powder were performed before and after each sample run.

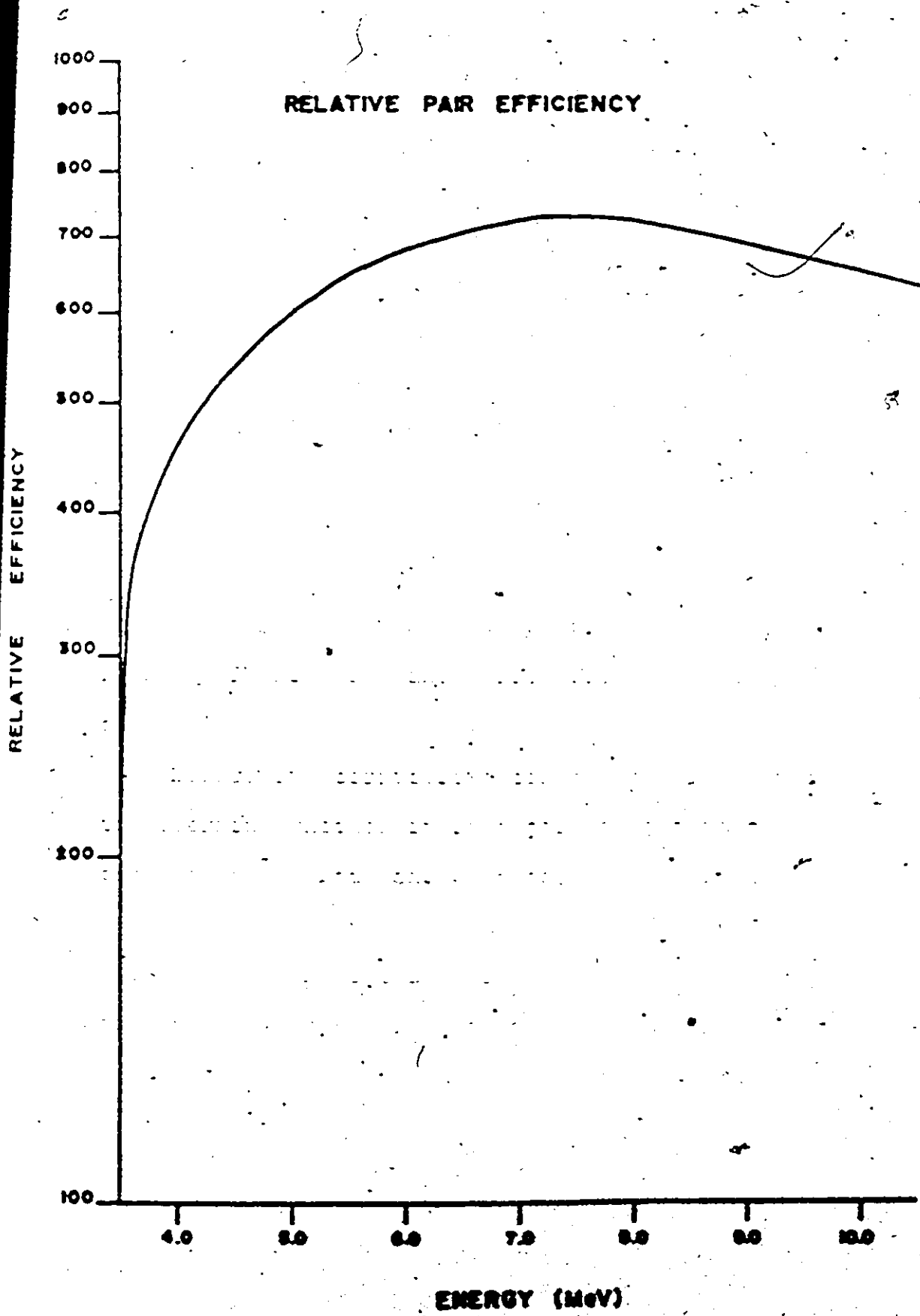
Throughout the runs the stabilizing system showed no indication of any unsatisfactory performance. However it was necessary to check for any changes since small variations may not be easily observed. This was done by carefully investigating the nitrogen spectra.

The nitrogen spectra were obtained using three identical samples. Although the reactor power may have changed from run to run the signal to noise ratio should remain the same. Furthermore the statistical accuracy for a given nitrogen peak should be approximately the same for all the nitrogen spectra since this was maintained by adjusting the time of data collection. It is therefore expected that the spectra will be very identical in all aspects. Any changes in the peak positions can only be caused by instabilities in the detection and data handling system.

The most direct and easiest way to detect the average shift of the nitrogen peaks would be by calculating the cross-correlation function of the first and the later calibration runs and comparing it with the auto-correlation function of the initial calibration run.

Figure 5.3

Relative Efficiency Curve



Let $N_1(X)$ and $N_j(X)$ represent the counts in channel number X for the first and the j^{th} calibration runs. Then the auto-correlation and the cross-correlation functions are given respectively by

$$R_{11}(\epsilon) = \int N_1(X)N_1(X+\epsilon) dX$$

$$R_{1j}(\epsilon) = \int N_1(X)N_j(X+\epsilon) dX$$

where the limits of integration included most of the nitrogen lines. Let ϵ_{11} be the position of the maximum of $R_{11}(\epsilon)$ and ϵ_{1j} that of $R_{1j}(\epsilon)$. Then the average shift of the lines in the j^{th} spectrum relative to the first is $\delta_{ij} = \epsilon_{11} - \epsilon_{1j}$. Had there been no change in the line positions then $\delta_{ij} = 0$ for all j . The value of δ_{ij} plotted as a function of time is shown in Fig. 5.4 and varies from -0.20 to $+0.26$ channel.

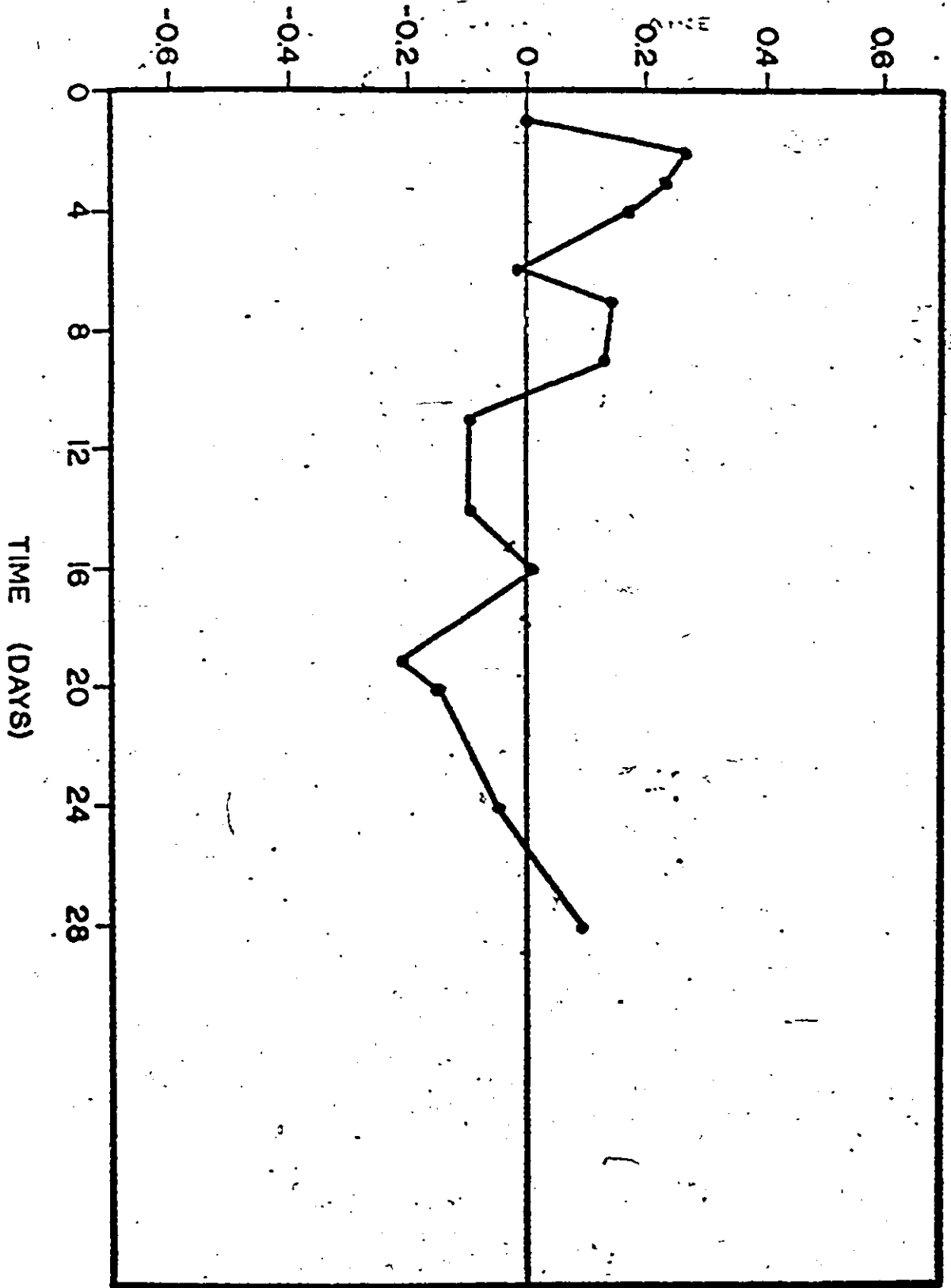
Before any corrections can be done it is necessary to determine whether it is a gain or a zero change or a combination of both and what caused it. If the cause of change is random then the best values of the gain and zero would have to be obtained from the average values calculated from the nitrogen calibrations before and after each run. If they changed because of rate effects then these must be corrected accordingly.

The method of extraction of the change in gain and zero of any nitrogen spectra relative to the first is as follows. Assume the gain to be G so that a gamma ray of energy E_γ will be stored in channel number C and that

Figure 5.4

Average Shift of Nitrogen Lines Obtained by Method of
Cross-Correlation

CENTROID CHANGE



of energy zero in Co. Then $E_Y = G(C-Co)$. Since E_Y is fixed, $\Delta E_Y = 0 = \Delta G(C-Co) + G(\Delta C - Co)$. This yields

$$\Delta C = -\frac{\Delta G}{G}C + \left(\frac{\Delta G}{G}Co + \Delta Co\right).$$

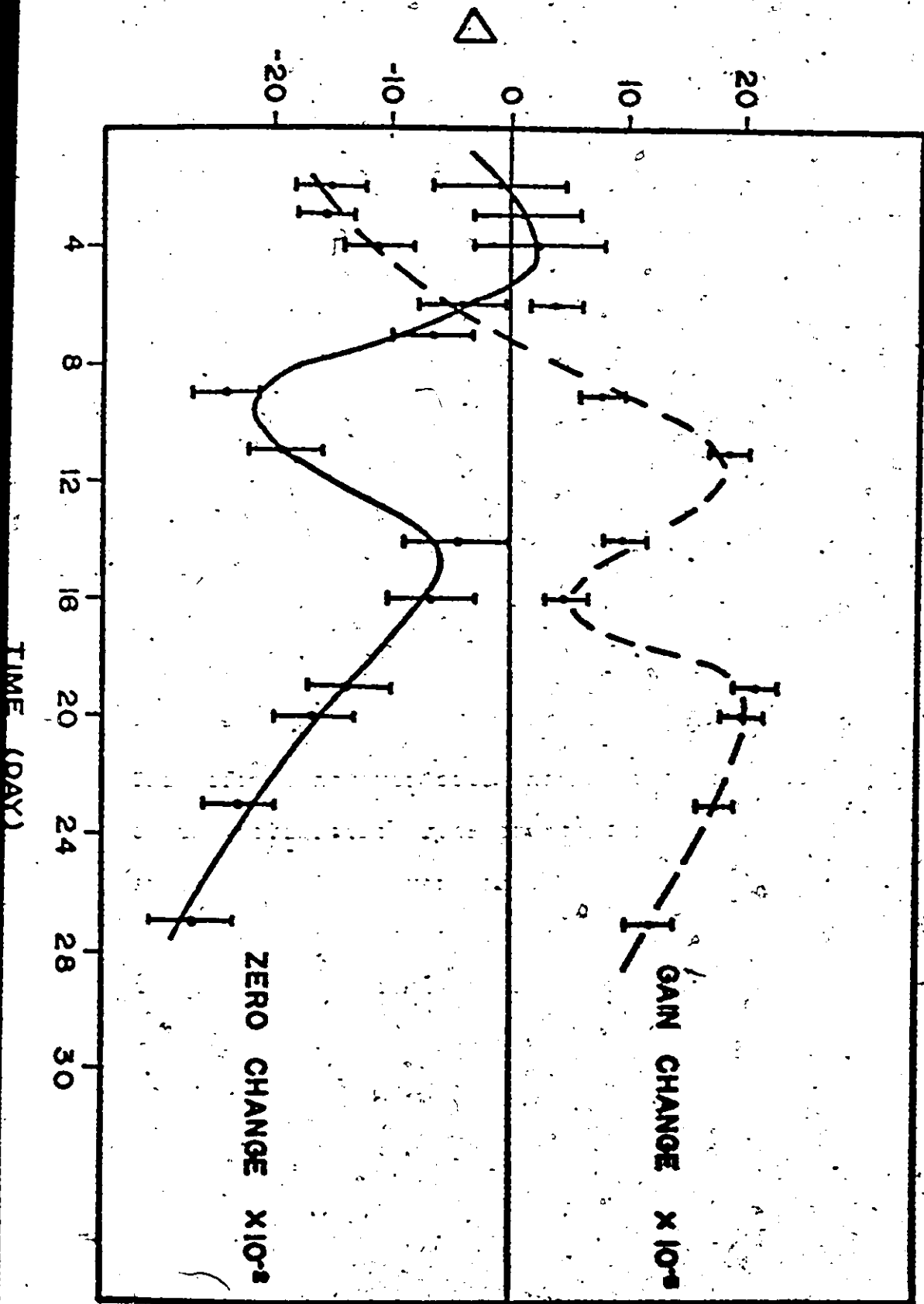
Therefore if the difference in the peak positions relative to the first nitrogen run ΔC , is plotted against the initial peak positions C , then ΔG can be calculated from the slope and ΔCo from the intercept. The slopes and intercepts were obtained by linear least squares method. The result is shown in Fig. 5.5.

There are at least three possible causes of these gain and zero changes. One would be due to variations in the ambient temperature and humidity which might have affected the electronic and detection system. Another possibility would be due to instability of the reference pulser. Lastly it could be due to dependence of the system performance on changes in absolute rates of the incident radiation from one spectrum to another.

It has been shown ^(St 68) that the reference pulser is very stable. As for the variation in ambient conditions this could not be easily controlled, however it is expected that the average values of the gain and zero from the calibration runs would be very close to their values during the sample run. Therefore the only systematic cause of error which can be corrected is the rate effect.

Figure 5.5

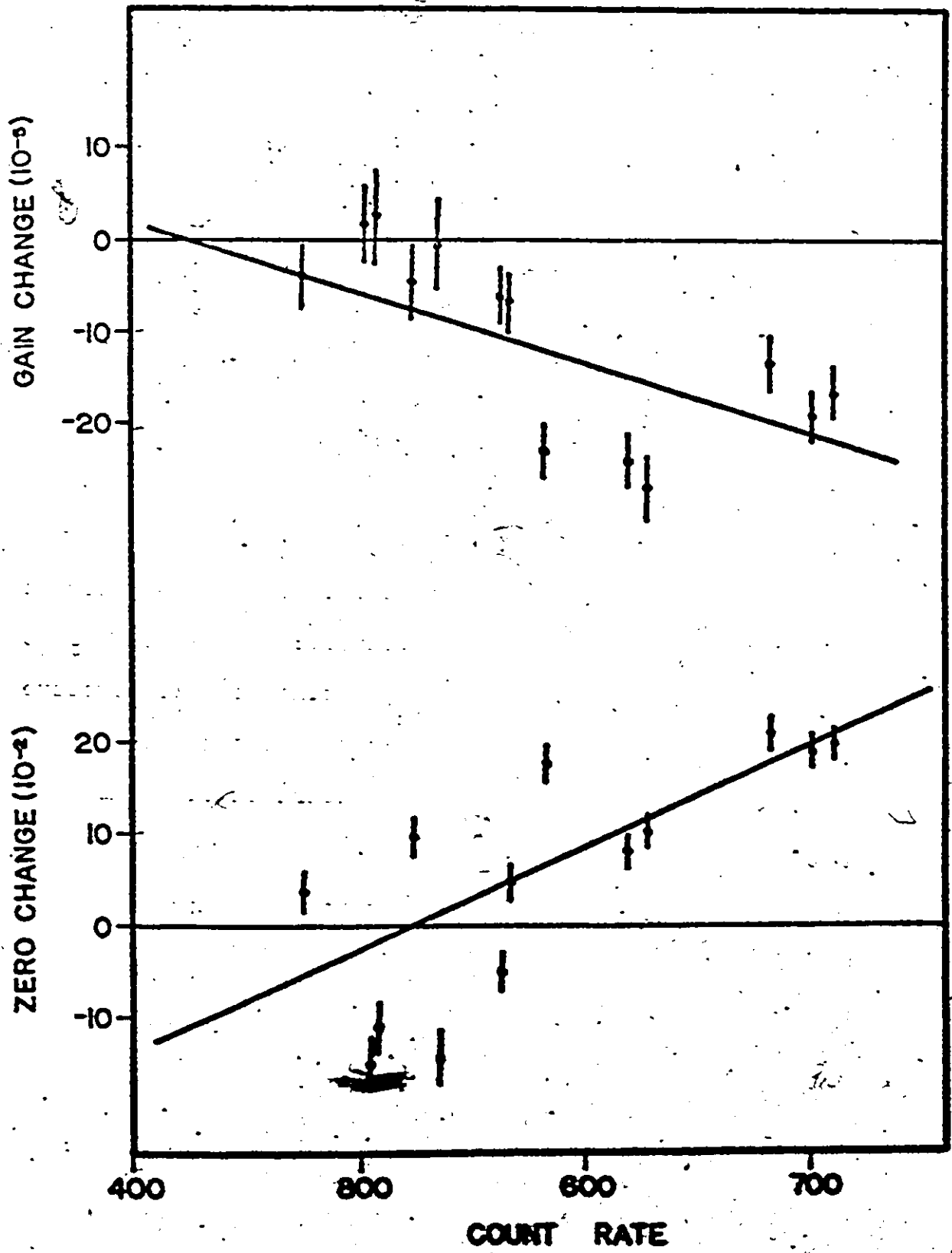
Change in Gain and Zero as a Function of Time



It was never expected that the rate dependence would be very significant. Furthermore since the sample sizes for the calibration runs are about the same, small rate changes would only be due to reactor power which could have varied from 1.5 to 2.0 MW to suit the requirements of other experiments. A plot of the calculated ΔG (gain change) and ΔZ (zero change) against average rate is shown in Fig. 5.6. Some sort of rate dependence is observed for both of them.

Another factor that is suspected is the line shape dependence of the stabilizer. Since it senses the median of the pulser peaks rather than the centroid, additional background under them could cause asymmetries. Therefore a difference in asymmetry from one spectrum to another will cause the stabilizer to shift the gain and the zero values. This effect however could not be very significant as far as the calibration runs are concerned because the melamine spectra should be very identical.

Nonetheless a more controlled experiment was done to verify the effects of rate variations and also the effect of varying amount of background under the reference pulses. To simulate rate changes a strong Co^{56} source was placed at different distances from the Ge(Li) counter. The gain was increased so that the maximum energy at 3.5 MeV was stored around the maximum channel number. Hence small change in gain or zero would be more easily observed. The stabilizer was also set up as in the actual experiment using the same source of reference pulses. The count rate was varied in



such a way that the analyzer dead time ranged from 0 to 60% compared to about a change of 5% in the actual runs. The result showed that there was no significant change in centroid positions of the peaks proving that the rate effects could not account for the observed shift in the nitrogen spectra. The observed correlation cannot therefore be very meaningful.

The dependence of the stabilizer on the window width about which correction was made and on the shape of the pulser peaks was then investigated. This was done by introducing varying rates of background under the reference peaks. Each run was then repeated so that the background under the pulser peaks were gated out. This means that stabilization is purely on the undistorted pulser peaks. When the centroids of the lines were determined and compared, no significant evidence of peak shifts were observed.

The results of these controlled experiments proved that there is no straightforward way of correcting for the seemingly observed gain and zero fluctuations.

Fortunately there are some built in reference lines common to all the spectra which can be used as internal calibrations. These are lines due to capture in the aluminum material seen by the detector, in the carbon sample holder and in the B^{10} filter. Although there are not enough lines to give accurate calibration throughout the whole energy

range in the spectra, they are sufficient to give an indication of the consistency of the average obtained from the calibration runs. The final results are obtained using the data from the nitrogen calibration runs as well as these internal references lines. Nevertheless because of the inability to ascertain the proper corrections to be made and because of the above approximations, the errors assigned the centroid shifts are increased by a factor of 2.



CHAPTER VI

EXPERIMENTAL DATA

This section summarizes the experimental conditions under which the data were obtained and the results of the data analysis carried out as described previously.

1. Experimental Conditions

The cobalt and manganese powder samples were purchased from Alfa Inorganics Ltd, Beverly, Massachusetts. The cobalt powder purity is 99.8% and has the following contaminants in parts per million (ppm): Ni = 750, S = 150, C = 150, others less than 10. For the manganese the purity is 99.9% with the following contaminants in ppm: Fe = 500, S = 250, O = 5000, N = 70, C = 100, Si = 10, P = 10. The solid cobalt samples were prepared by melting cobalt pellets in a cylindrical alumina container 1/2" inside diameter, and then cutting it into 2.54 cm lengths. A summary of the experimental conditions for cobalt and manganese is shown in Tables 6.1 and 6.2.

For the nitrogen calibration runs three identical samples were prepared from melamine powder which contains mainly nitrogen and hydrogen. Each sample is contained in a cylindrical carbon capsule 1/2" inside diameter and 1-1/2" long. The length of data accumulation for each calibration run was adjusted to maintain approximately identical statistics. On the average this is 36 hours. The average count rate is 3000 cpm.

TABLE 6.1

Cobalt Sample - Experimental Conditions

Nominal* Filter Thick	Normal Filter Thick. gm/cm ²	Sample wt. gms	Sample Form	Average Pair Rate CPM	Length of Data Acc. Hr
0	0	4	Powder	8000	12
1/8"	0.35	18	Powder	9000	6
3/16"	0.58	10	Powder	6000	23
1/4"	0.74	17	Powder	6300	12
3/8"	0.93	25	Solid	6600	16
1/2"	1.16	26	Solid	4600	47
5/8"	1.43	25	Solid	6500	44

*Difference between the nominal and the actual filter thickness is due to difference each sample was packed.

TABLE 6.2Manganese - Experimental Conditions

Nom. Filter Thickness	Filter Thickness (g/m/cm ²)	Sample wt. (gms)	Sample Form	Average Pair Rate (cpm)	Length of Data Acc (HRS)
0	0	4	Powder	6700	7
1/8	0.33	15	Powder	6000	21
3/16	0.62	13	Powder	8000	15
1/4	0.74	17	Powder	4600	18
5/16	0.91	21	Powder	5000	22
7/16	1.16	22	Powder	7000	36
1/2	1.29	13	Powder	6000	44

2. Experimental Results

The different spectra using different filter thicknesses are shown in Figs. 6.1 to 6.4 for cobalt and Figs. 6.5 to 6.8 for manganese. The main characteristics of these spectra are

1. The variation of the line intensity for the different gamma rays from run to run
2. The increase of the continuum background relative to the line intensities with increasing filter thickness and.
3. The growing prominence of the B^{10} , C and Al lines with thicker filter.

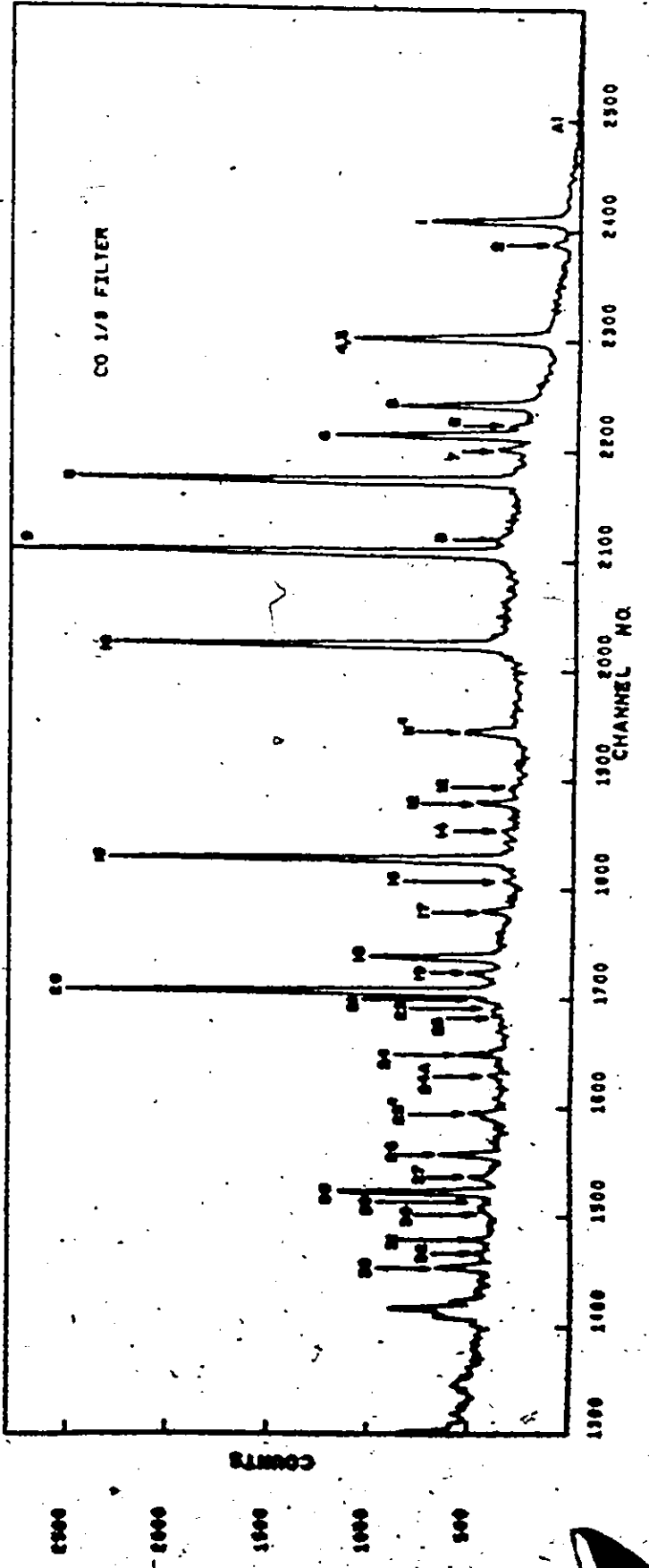
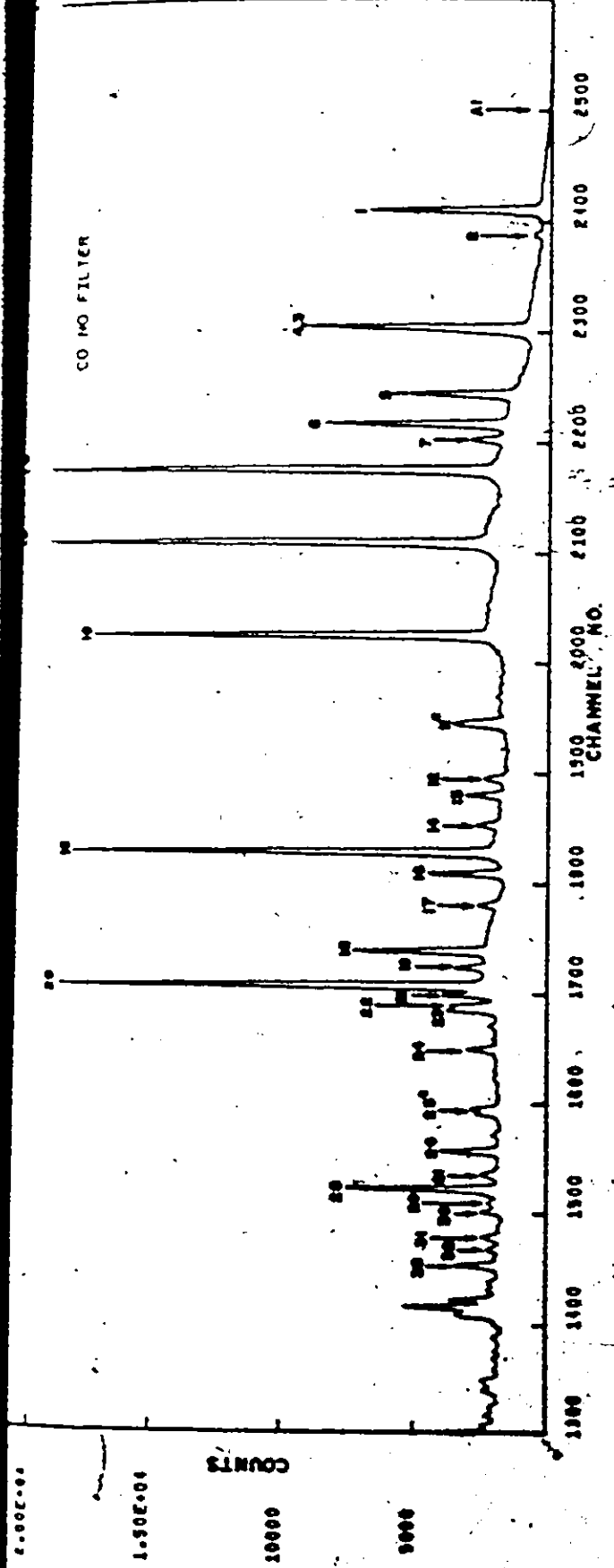
Furthermore, although it is not very obvious, some of the lines exhibit definite centroid shifts and increases in FWHM. Another obvious observation is the increasing skewness of the line shapes which is not present in the nitrogen lines. This implies that the asymmetry is not due to the response function of the system but more possibly due to the contributions from high energy resonances.

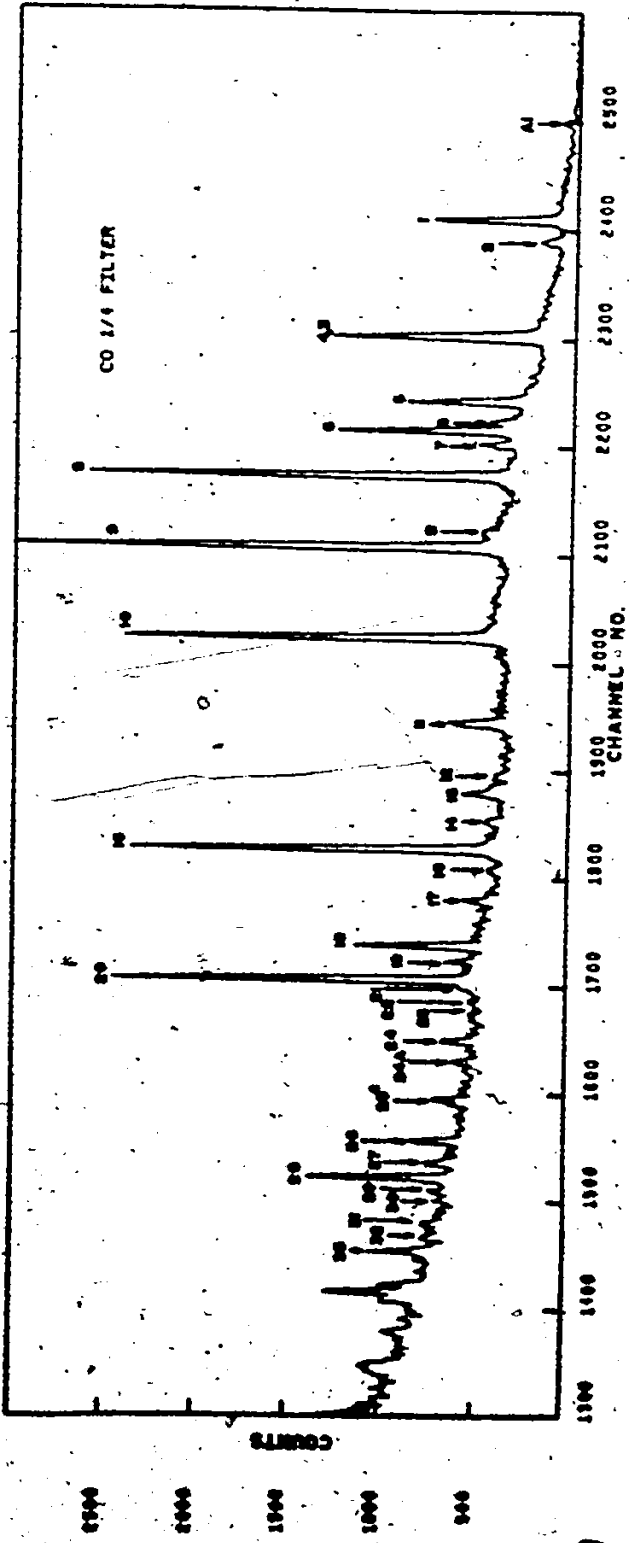
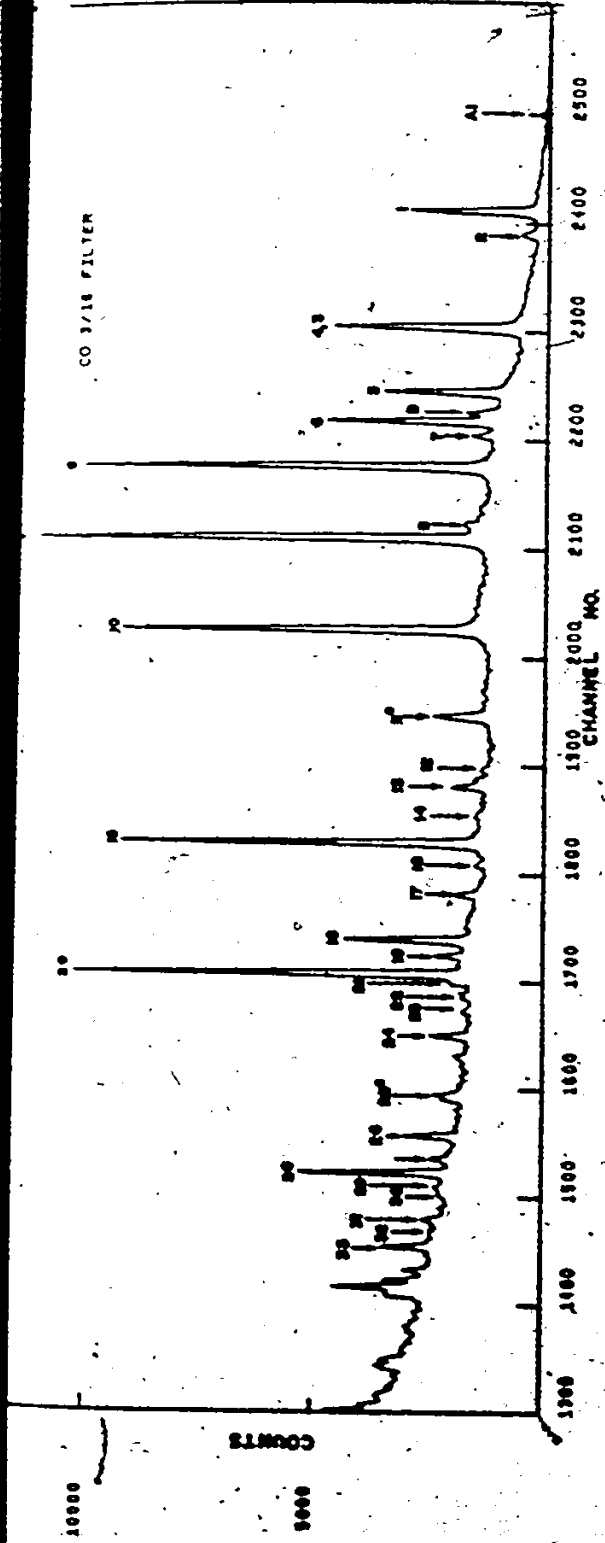
Since interest is in the primary high energy radiative transitions, the lower energy portion of each of the gamma ray spectra is ignored. The different spectra are identified by quoting the nominal filter thickness in inches.

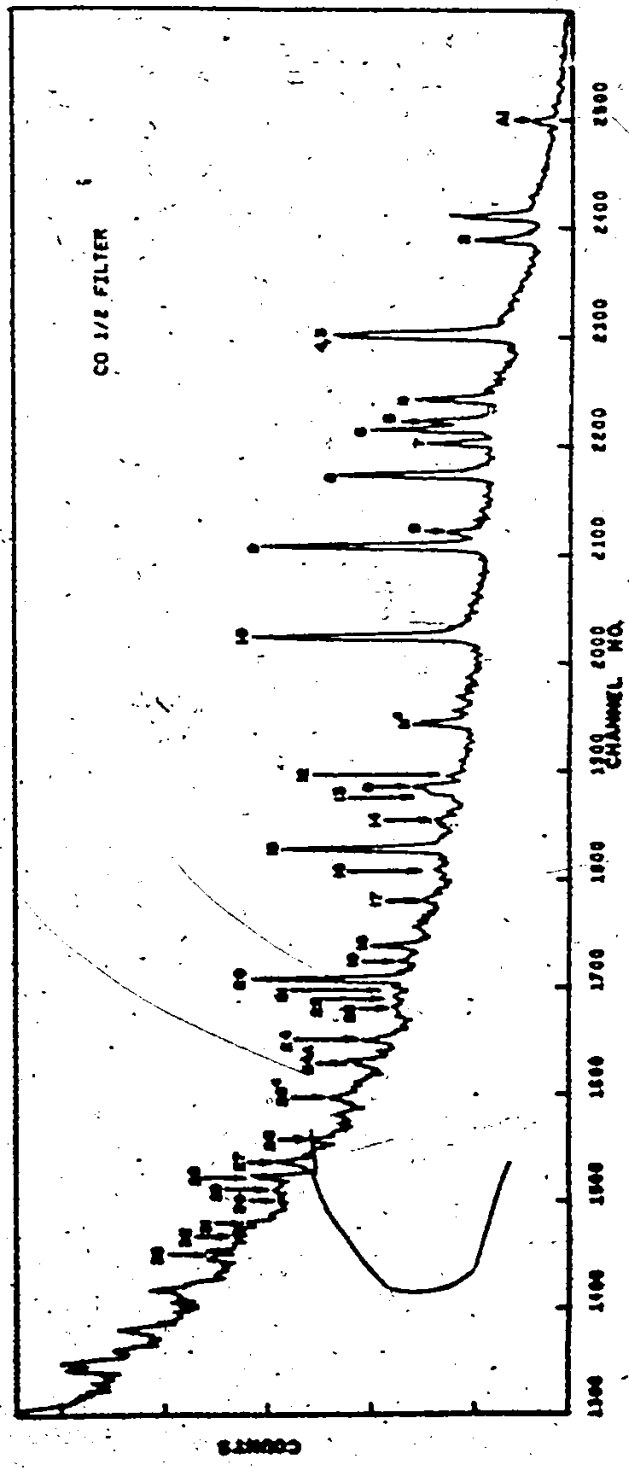
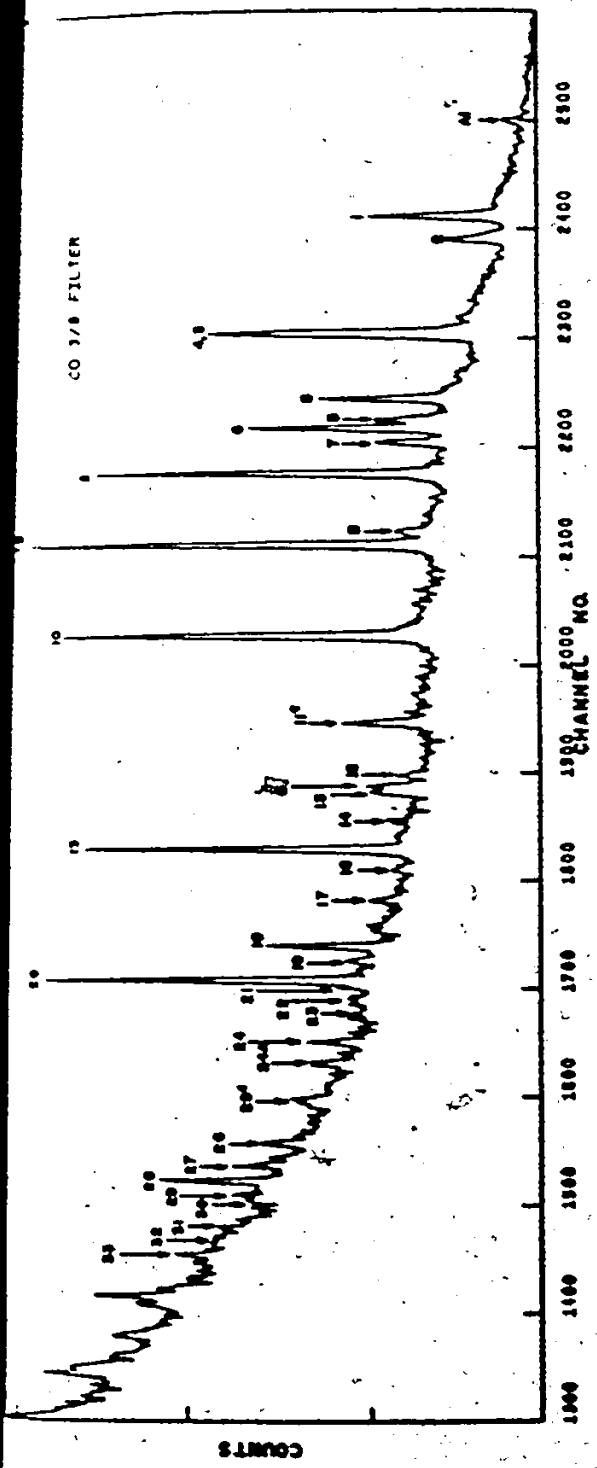
Following the data analysis described in the previous section the 0-filter energies and the absolute intensities are summarized in Table 6.3,4 for cobalt and Table 6.5,6 for

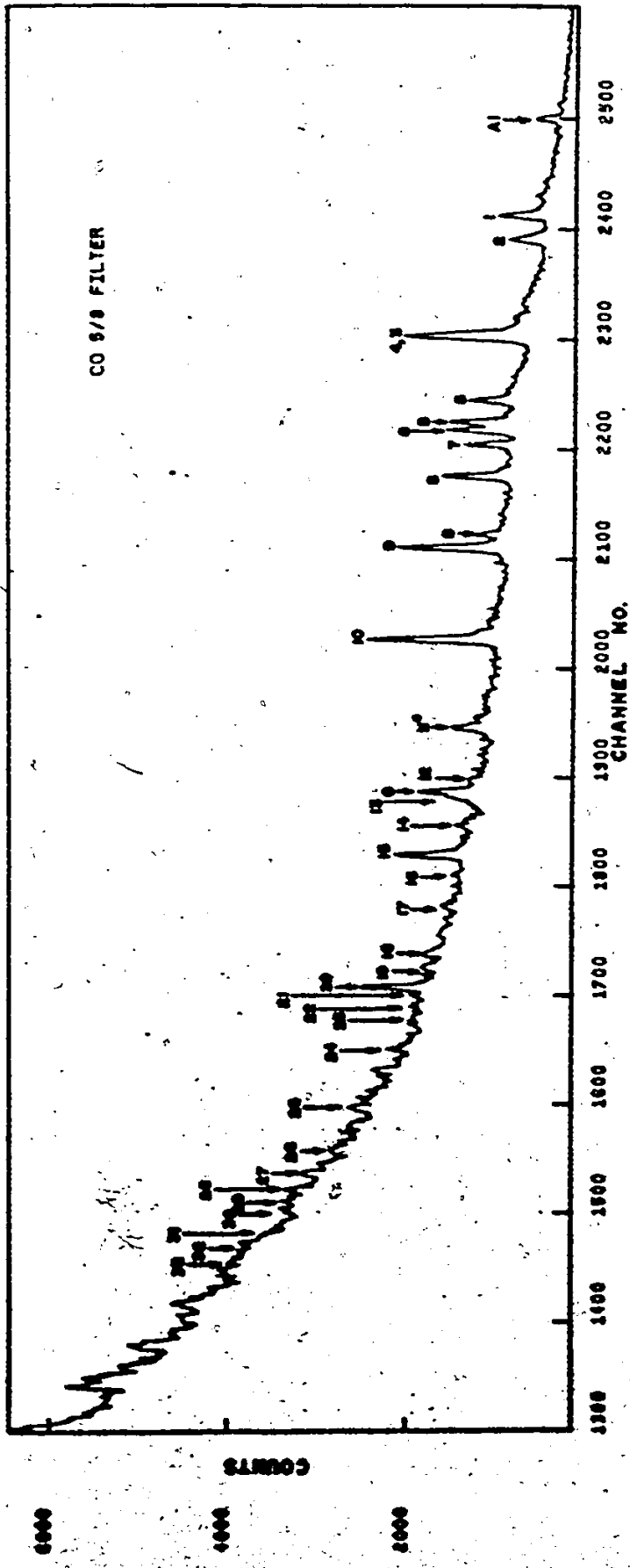
Figures 6.1 - 6.4

Co^{60} Spectra Obtained with Different Filter Thicknesses



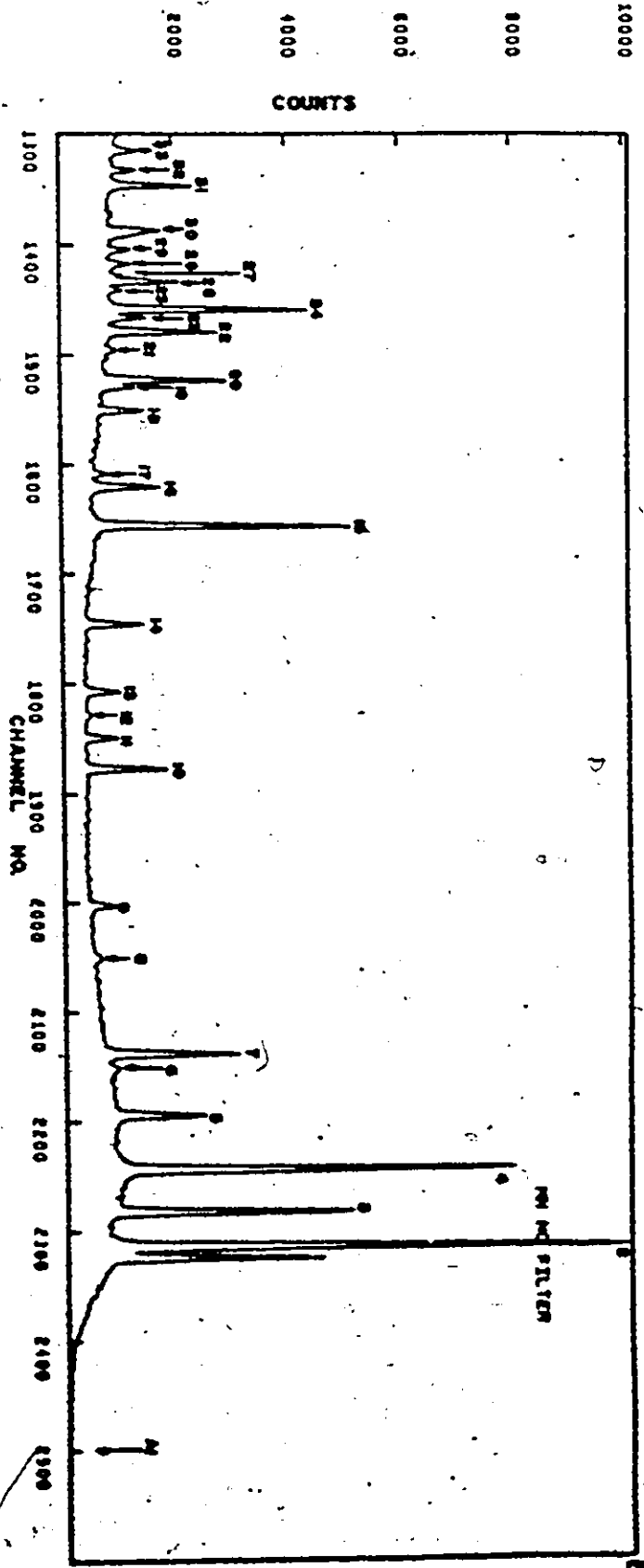
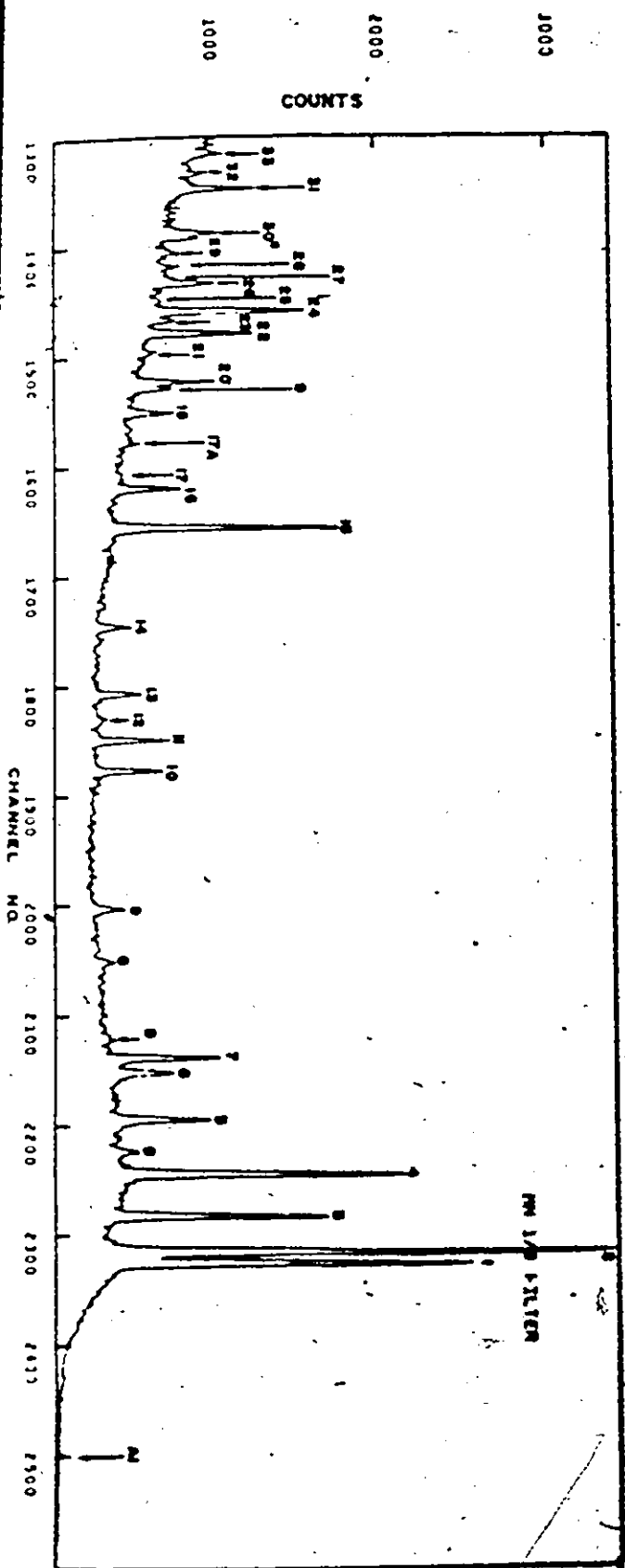


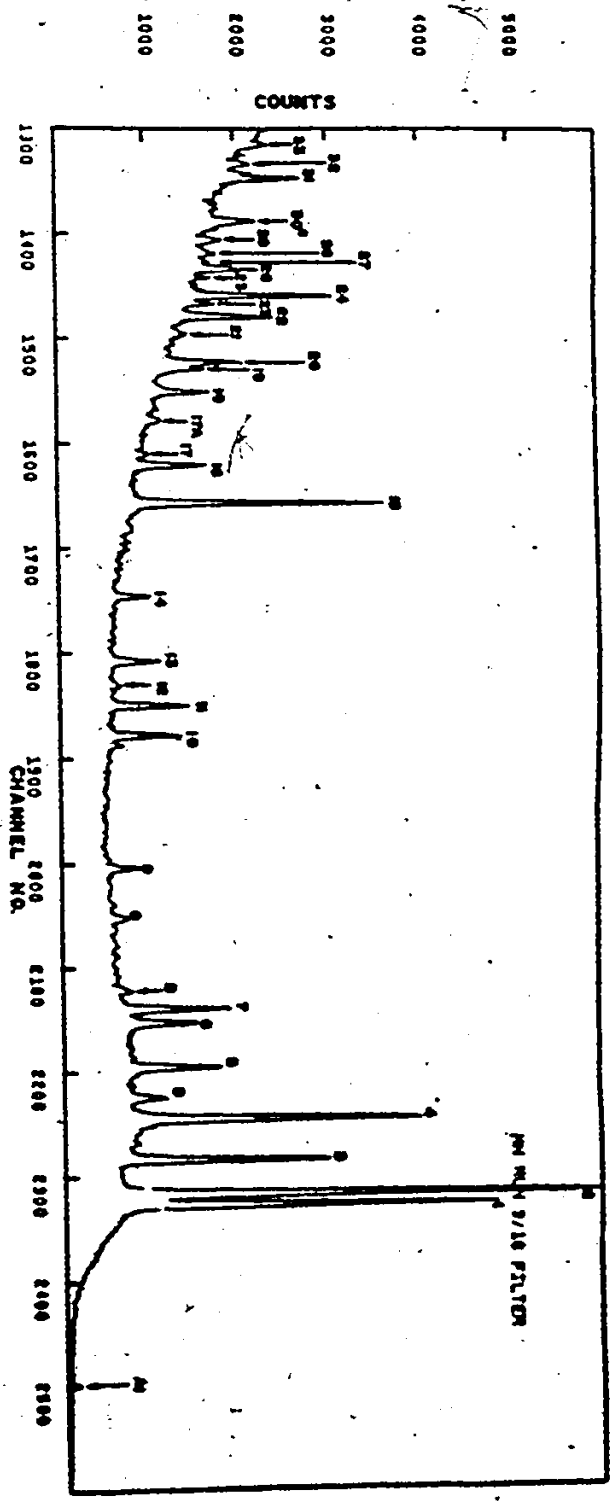
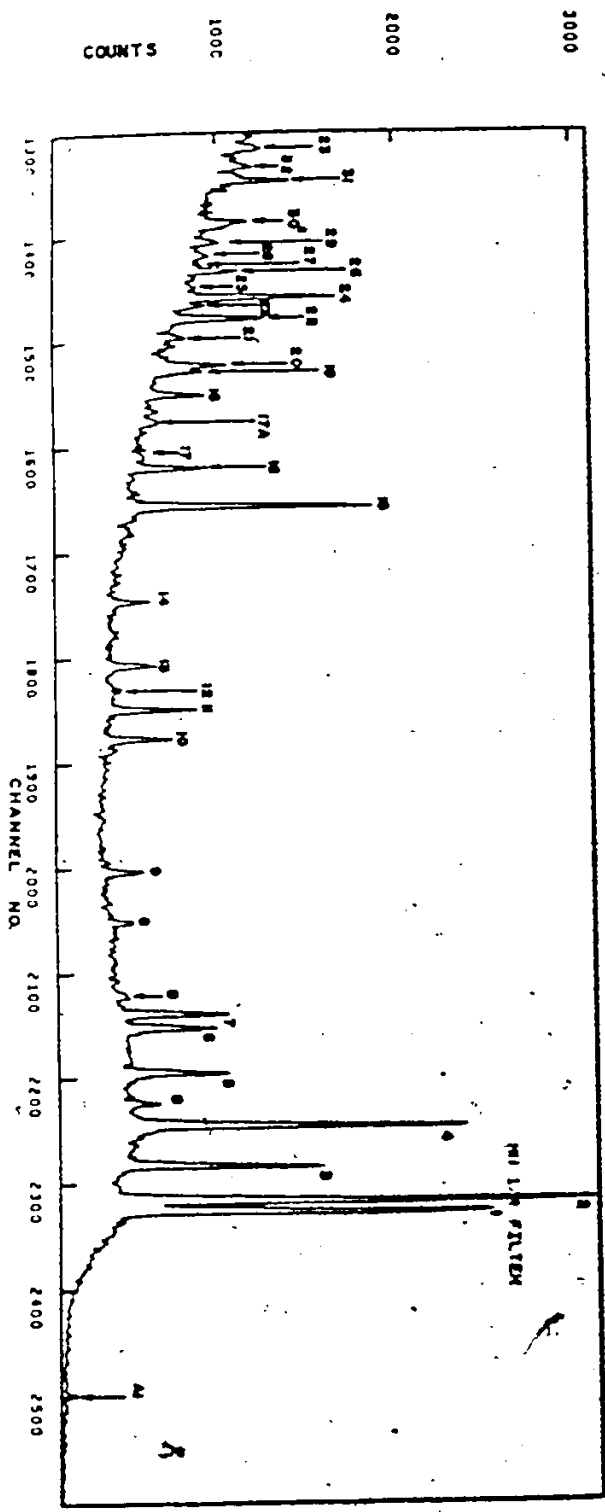




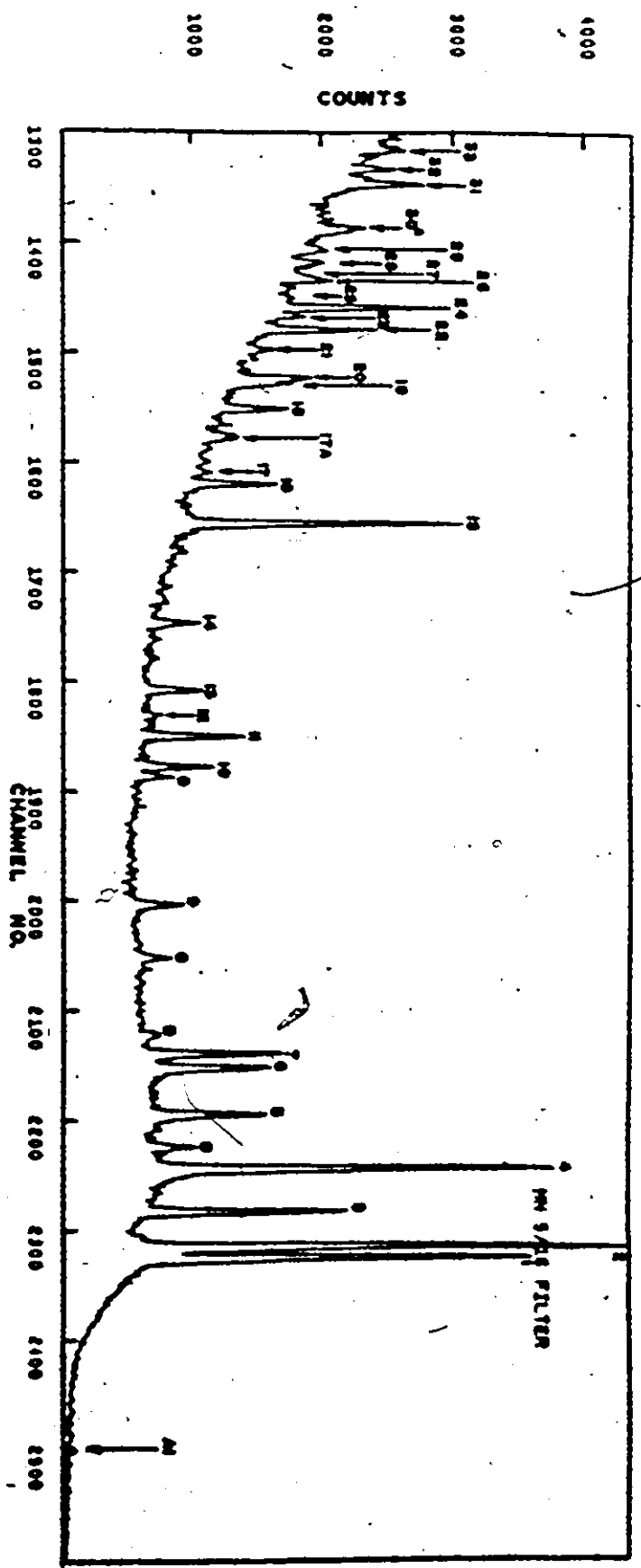
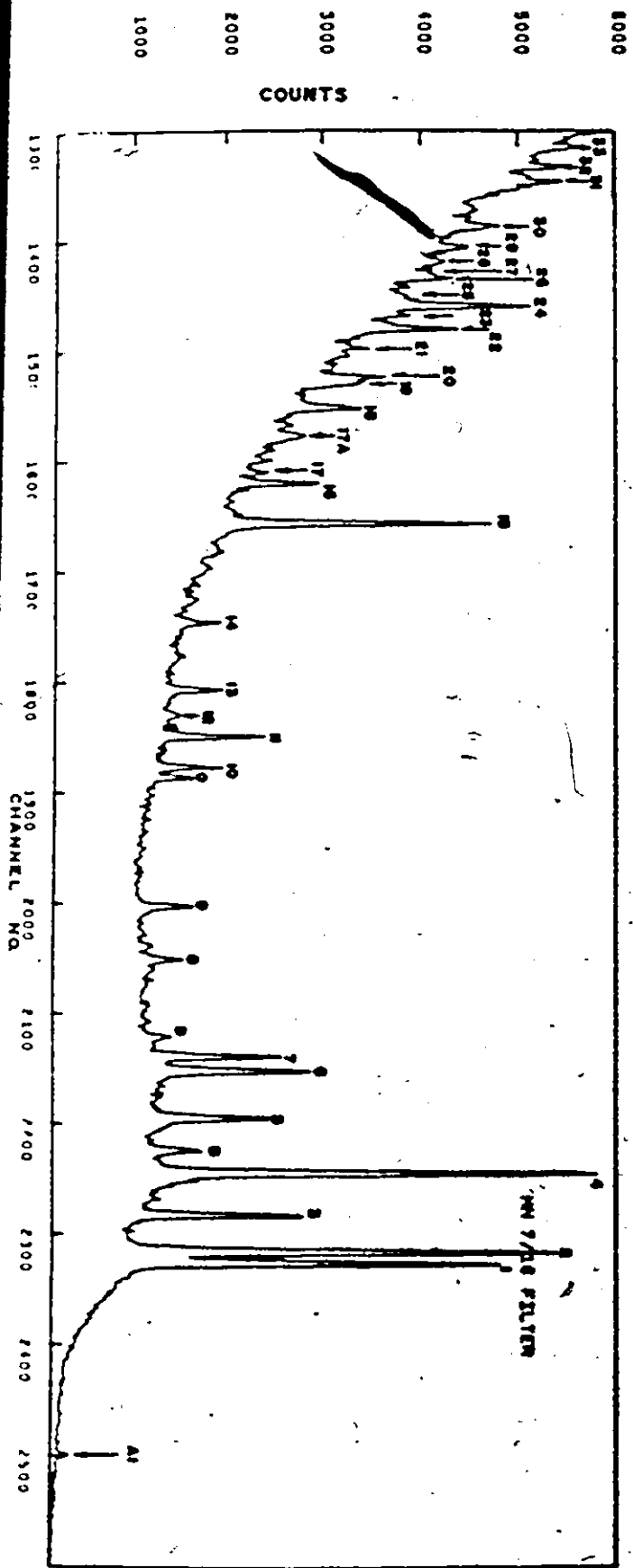
Figures 6.5 - 6.8

Mn⁵⁶ Spectra Obtained with Different Filter Thicknesses





NATIONAL BUREAU OF STANDARDS
 PHYSICS DIVISION
 GAITHERSBURG, MARYLAND 20899



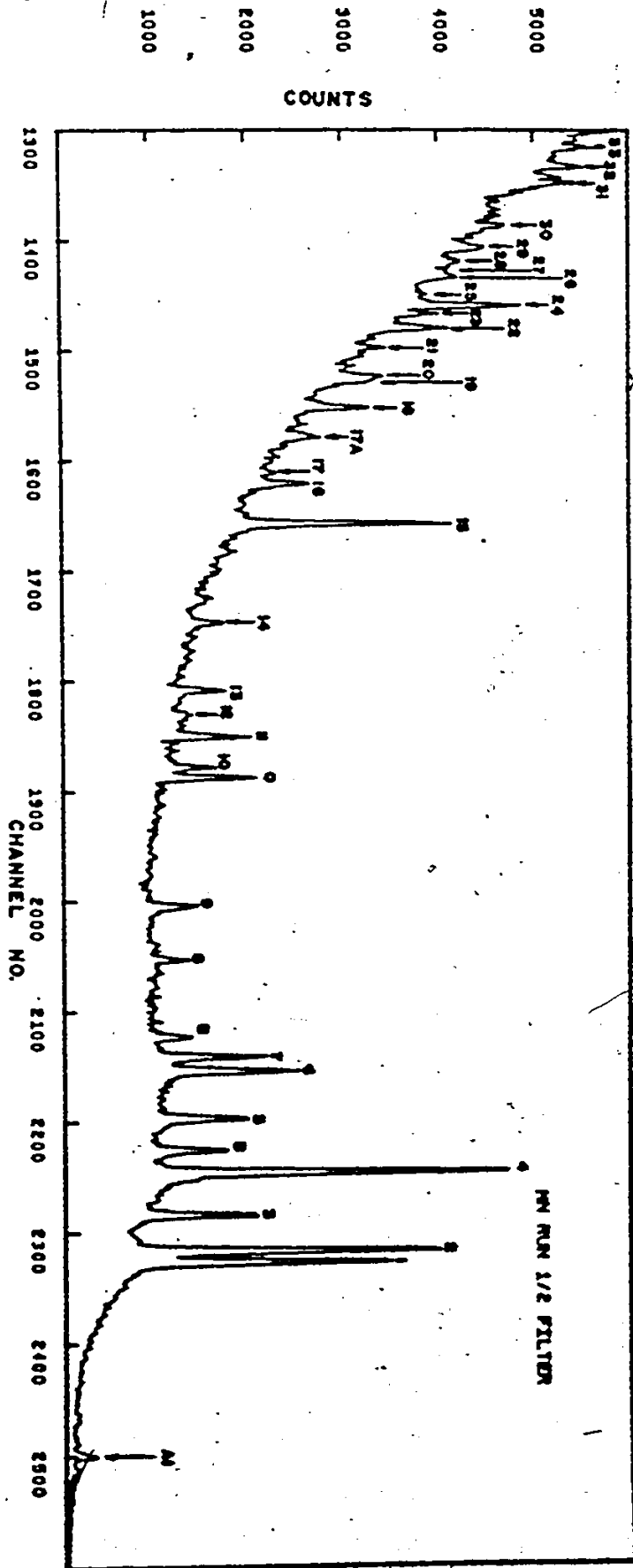


TABLE 6.3

High Energy Gamma Rays from $^{59}\text{Co}(n,\gamma)^{60}\text{Co}$

Line No.	Energy (keV)	Excitation Energy of Final State
1	7491.8	0
2	7433.6	58.2
3	7214.9	276.8
4	7203.9	287.9
5	7055.9	435.9
6	6985.4	506.3
7	6948.9	542.8
8	6876.9	614.9
9	6705.7	786.1
10	6486.1	1005.6
11 ^c	6283.7	1208.0
	6274.6	1217.2
12	6149.4	1342.3
13	6110.8	1381.0
14	6040.5	1451.3
15	5975.8	1515.9
16	5925.9	1565.9
17	5852.0	1639.7
18	5742.7	1749.1
19	5704.4	1787.4
20	5660.5	1831.3

TABLE 6.3 (cont.)

Line No.	Energy (keV)	Excitation Energy of Final State
21	5639.9	1851.8
22	5615.0	1876.7
23	5603.7	1888.1
24	5511.2	1980.6
25 ^c	5370.9	2120.8
	5359.4	2132.3
26	5270.8	2221.0
27	5214.9	2276.9
28	5182.1	2309.6
29	5149.9	2341.8
30	5128.5	2363.3
31	5069.5	2422.3
32	5040.9	2450.9
33	5002.1	2489.6

1. c denotes a complex peak

2. Uncertainty in these values ± 1.5 keV

TABLE 6.4

Observed Intensities of Transitions in the $\text{Co}^{59}(\text{n},\gamma)\text{Co}^{60}$ Reactions (photons/1000n)

Line No.	Nominal Filter Thickness (inch)							
	0	1/8	3/16	1/4	3/8	1/2	5/8	
1	27.2 ± 1.5	25.1 ± 1.5	24.5 ± 1.4	24.2 ± 1.5	26.4 ± 1.8	27.8 ± 2.1	29.6 ± 2.7	
2	1.3 ± 0.2	2.8 ± 0.6	3.4 ± 0.4	4.6 ± 0.8	13.4 ± 1.3	18.5 ± 1.7	25.8 ± 2.5	
3 } 4 }	41.8 ± 2.2	40.4 ± 2.4	42.1 ± 2.3	46.9 ± 2.8	68.4 ± 4.1	87.8 ± 5.2	102.7 ± 6.6	
5	16.9 ± 1.1	21.4 ± 1.5	22.6 ± 1.3	22.3 ± 1.6	22.1 ± 1.8	23.5 ± 2.1	22.3 ± 2.7	
6	27.8 ± 1.5	32.4 ± 2.0	31.6 ± 1.8	33.2 ± 2.1	35.2 ± 2.2	36.0 ± 2.2	35.2 ± 2.5	
7	5.1 ± 0.4	3.5 ± 0.8	3.2 ± 0.5	6.0 ± 0.9	12.1 ± 1.3	18.1 ± 1.6	22.0 ± 1.8	
8	82.6 ± 4.4	81.7 ± 4.7	78.3 ± 4.3	75.3 ± 4.3	60.6 ± 3.7	50.6 ± 3.4	40.2 ± 3.6	
9	78.3 ± 4.2	40.1 ± 5.2	93.0 ± 5.1	93.2 ± 5.3	82.2 ± 4.9	77.4 ± 4.7	68.7 ± 4.8	
10	62.8 ± 3.4	67.4 ± 3.9	68.5 ± 3.7	69.1 ± 4.0	70.4 ± 4.2	72.4 ± 4.4	76.8 ± 5.1	
11 ^o	11.7 ± 0.7	13.8 ± 1.3	13.1 ± 0.8	14.3 ± 1.4	17.4 ± 1.8	18.9 ± 1.5	24.6 ± 3.2	
12	3.3 ± 0.3	1.7 ± 1.0	0.7 ± 0.3	2.9 ± 0.8	2.8 ± 0.9	4.5 ± 1.0	<1.5	
13	5.6 ± 0.4	6.8 ± 0.9	7.8 ± 0.5	6.1 ± 1.0	13.2 ± 1.0	10.5 ± 0.9	11.4 ± 1.1	
14	3.4 ± 0.4	2.4 ± 0.9	1.2 ± 0.6	2.7 ± 1.2	1.7 ± 0.9	5.5 ± 1.1	8.4 ± 1.6	

TABLE 6.4 (con't)

Line No.	Nominal Filter Thickness (Inch)									
	0	1/8	3/16	1/4	3/8	1/2	5/8			
15	67.5 ± 5.6	70.3 ± 4.0	69.1 ± 3.8	67.1 ± 3.9	59.1 ± 3.7	50.6 ± 3.4	43.1 ± 3.9			
16	11.2 ± 0.7	1.7 ± 0.9	1.7 ± 0.5	3.7 ± 1.0	1.1 ± 0.8	2.3 ± 1.7	1.6 ± 1.3			
17	3.1 ± 0.4	5.1 ± 1.2	4.4 ± 0.7	4.9 ± 1.3	4.8 ± 1.8	6.4 ± 2.2	6.2 ± 3.4			
18	21.1 ± 1.2	24.4 ± 1.7	22.9 ± 1.4	22.0 ± 1.7	19.4 ± 1.9	12.7 ± 2.1	13.4 ± 3.0			
19	4.4 ± 0.4	4.5 ± 1.0	4.5 ± 0.6	2.3 ± 1.0	4.6 ± 1.2	2.4 ± 1.1	6.1 ± 2.1			
20	79.2 ± 4.3	74.8 ± 4.3	74.8 ± 4.1	67.7 ± 3.9	61.8 ± 3.8	46.5 ± 3.4	39.4 ± 3.8			
21	7.8 ± 0.4	3.0 ± 0.9	3.8 ± 0.3	2.1 ± 0.7	3.5 ± 0.4	4.8 ± 0.4	4.7 ± 0.4			
22	6.6 ± 0.4	<0.4	0.6 ± 0.5	<0.5	1.3 ± 0.6	<0.8	<1.5			
23	7.5 ± 0.4	<0.4	0.6 ± 0.5	<0.5	1.3 ± 0.6	<0.8	<1.5			
24	4.6 ± 0.4	6.0 ± 1.3	6.8 ± 0.8	6.4 ± 1.5	7.2 ± 2.1	12.5 ± 2.7	7.1 ± 2.2			
25 ^o	7.7 ± 0.5	7.5 ± 1.1	7.6 ± 0.6	6.3 ± 0.8	9.0 ± 1.7	10.6 ± 2.2	9.2 ± 3.1			
26	9.3 ± 0.6	10.2 ± 1.2	9.6 ± 0.8	9.4 ± 1.4	8.0 ± 2.0	5.0 ± 2.0	6.9 ± 2.6			
27	3.2 ± 0.3	3.7 ± 1.1	3.3 ± 0.6	6.1 ± 1.3	5.0 ± 1.4	10.6 ± 2.5	12.4 ± 2.9			
28	24.4 ± 1.3	27.3 ± 1.9	26.4 ± 1.6	25.2 ± 1.9	18.7 ± 1.3	14.0 ± 2.6	6.9 ± 3.2			
29	1.5 ± 0.1	<0.5	2.4 ± 0.5	3.3 ± 1.1	1.4 ± 1.3	<1.2	<1.8			

TABLE 6.4 (con't)

Line No.	0	1/8	3/16	1/4	3/8	1/2	5/8
30	2.7 ± 0.3	<0.5	1.7 ± 0.3	1.6 ± 0.5	<1.0	<1.2	<1.8
31	1.5 ± 0.3	2.0 ± 1.1	2.7 ± 0.7	2.1 ± 0.8	3.1 ± 1.2	7.0 ± 1.3	43.5
32	1.5 ± 0.3	<1.0	<0.3	2.1 ± 1.0	<1.0	<1.3	<3.0
33	7.0 ± 0.5	9.6 ± 1.3	9.5 ± 0.9	8.3 ± 1.6	5.4 ± 2.3	0.3 ± 0.3	<3.5

Note: e denotes complex peak

TABLE 6.5

Observed High Energy Gamma Rays in Mn⁵⁵(n, γ)Mn⁵⁶

Line No.	Final State Excitation Energy (keV)	Gamma Ray Energies (keV)
1	0	7270.5
2	26.7	7243.8
3	110.6	7159.9
4	212.6	7057.9
5	341.2	6929.3
5a	451.9	6818.6
6	486.7	6783.8
7	716.5	6554.0
8	840.9	6429.6
9	1165.7	6104.8
10	1239.7	6030.8
11	1293.2	5977.3
12	1349.6	5920.9
13	1509.3	5761.2
14	1743.1	5527.4
15	1835.3	5435.2
16	1865.8	5404.7
17	2016.1	5254.4
18	2071.9	5198.6
19	2089.0	5181.5

TABLE 6.5 (CON'T)

Line No.	Final State Excitation Energy (keV)	Gamma Ray Energies (keV)
20	2159.1	5111.4
21	2202.6	5067.9
22	2235.3	5035.2
23	2255.7	5014.8
24	2300.5	4970.0
25	2321.4	4949.1
26	2362.7	4907.8
27	2395.4	4875.1
28 ^c	2430.4	4840.1
	2440.9	4829.6
29	2545.4	4725.1
30	2580.5	4689.6
31	2626.7	4643.8

Notes:

1. Uncertainty in these values ± 1.5 keV
2. c denotes complex peak

TABLE 6.6

Measured Intensities of Gamma Rays in Mn 55 (n,γ) Mn 56

Line No.	Nominal Filter Thickness (inch)									
	0	1/8	3/8	1/4	5/16	7/16	1/2			
1	50.4 ± 2.8	94.2 ± 5.2	95.3 ± 5.2	94.0 ± 5.2	89.9 ± 4.9	86.8 ± 4.7	80.7 ± 4.5			
2	126.4 ± 6.8	125.5 ± 6.9	125.0 ± 6.7	119.4 ± 6.5	110.3 ± 6.0	105.1 ± 5.7	95.4 ± 5.2			
3	56.9 ± 3.1	54.6 ± 3.0	52.3 ± 2.8	47.8 ± 2.7	42.6 ± 2.4	38.2 ± 2.1	36.0 ± 2.1			
4	97.4 ± 5.1	73.5 ± 4.0	72.7 ± 3.9	80.7 ± 4.4	85.5 ± 4.6	97.0 ± 5.2	98.7 ± 5.4			
5	22.7 ± 1.3	23.9 ± 1.5	24.0 ± 1.4	23.9 ± 1.6	25.7 ± 1.6	29.7 ± 1.8	29.7 ± 1.9			
5a	1.5 ± 0.4	16.6 ± 1.3	18.7 ± 1.0	23.9 ± 1.6	27.5 ± 1.7	38.5 ± 2.3	39.8 ± 2.5			
6	31.7 ± 1.7	24.3 ± 1.7	26.8 ± 1.6	27.2 ± 1.8	29.7 ± 1.8	27.9 ± 1.8	28.3 ± 1.9			
7	1.9 ± 0.3	2.5 ± 0.7	4.6 ± 0.6	4.0 ± 0.8	5.9 ± 0.7	7.2 ± 0.8	6.7 ± 0.9			
8	6.0 ± 0.4	8.7 ± 0.8	7.9 ± 0.7	10.3 ± 0.9	11.0 ± 0.9	12.4 ± 0.9	14.4 ± 1.2			
9	19.0 ± 1.0	17.8 ± 1.2	19.1 ± 1.3	18.6 ± 1.6	16.2 ± 1.1	15.0 ± 1.2	14.7 ± 1.2			
10	7.3 ± 0.5	17.8 ± 1.2	19.2 ± 1.2	20.2 ± 1.3	21.4 ± 1.4	21.5 ± 1.4	21.1 ± 1.4			
11	1.7 ± 0.3	2.5 ± 0.7	1.6 ± 0.5	2.0 ± 0.8	2.1 ± 0.8	3.0 ± 0.7	2.4 ± 0.9			
12	8.3 ± 0.5	12.0 ± 0.9	12.8 ± 0.9	13.0 ± 1.1	12.9 ± 1.0	12.6 ± 1.0	12.2 ± 1.1			
13	14.0 ± 0.8	8.7 ± 0.9	8.2 ± 0.7	8.6 ± 0.9	9.4 ± 0.9	9.4 ± 1.0	9.9 ± 1.1			

TABLE 6.6 (CONT)

Line No.	Nominal Filter Thickness (inch)							
	0	1/8	3/8	1/4	5/16	7/16	1/2	
14	61.8 ± 3.3	60.6 ± 3.4	59.8 ± 3.2	60.2 ± 3.4	62.0 ± 3.4	65.2 ± 3.6	63.3 ± 3.6	
15	19.7 ± 1.1	19.3 ± 1.3	21.5 ± 1.4	21.7 ± 1.6	22.9 ± 1.6	23.2 ± 1.5	25.7 ± 1.9	
16	3.0 ± 0.4	0.9 ± 0.7	0.6 ± 0.6	2.6 ± 1.1	1.2 ± 0.8	3.4 ± 1.1	2.5 ± 1.3	
17	11.2 ± 0.7	13.6 ± 1.2	13.5 ± 1.0	14.0 ± 1.3	16.8 ± 1.4	23.1 ± 1.7	24.7 ± 2.0	
18	8.9 ± 0.7	11.1 ± 1.1	12.4 ± 1.2	12.5 ± 1.5	12.6 ± 1.2	12.7 ± 1.5	13.8 ± 1.8	
19	33.2 ± 1.9	21.0 ± 1.7	22.4 ± 1.7	20.1 ± 1.9	19.5 ± 1.6	16.0 ± 1.7	17.0 ± 2.0	
20	3.3 ± 0.4	3.8 ± 1.0	5.1 ± 0.9	4.2 ± 1.2	4.4 ± 1.3	4.2 ± 1.4	<1.6	
21	28.1 ± 1.6	29.4 ± 2.0	27.2 ± 1.7	27.6 ± 2.2	24.2 ± 1.8	24.5 ± 1.9	27.0 ± 2.5	
22	8.4 ± 0.9	5.9 ± 0.8	6.4 ± 1.5	5.0 ± 1.4	5.3 ± 0.9	3.7 ± 1.1	7.5 ± 1.7	
23	50.8 ± 2.9	38.1 ± 3.3	34.2 ± 3.1	33.3 ± 3.7	30.4 ± 3.0	20.4 ± 9.0	27.3 ± 4.0	
24	2.3 ± 0.6	1.2 ± 1.2	1.7 ± 0.8	<0.9	1.6 ± 1.1	<1.3	<1.6	
25	17.6 ± 1.3	14.9 ± 1.9	14.1 ± 1.9	9.9 ± 1.6	10.3 ± 1.4	4.4 ± 1.6	7.7 ± 1.7	
26	5.2 ± 0.7	4.0 ± 2.5	2.4 ± 1.5	3.4 ± 2.0	6.2 ± 1.3	5.1 ± 2.0	4.1 ± 1.8	
27	5.4 ± 0.6	5.6 ± 1.8	6.1 ± 1.4	6.6 ± 1.9	7.1 ± 1.4	8.5 ± 2.0	14.0 ± 4.6	

TABLE 6.6 (CONT)

Line No.	Nominal Filter Thickness (inch)							
	0	1/8	3/8	1/4	5/16	7/16	1/2	
28 ^c	5.8 ± 0.7	20.8 ± 2.2	3.4 ± 1.1	5.3 ± 1.0	15.3 ± 2.0	4.2 ± 1.5	4.7 ± 1.7	
29	13.8 ± 1.0		13.4 ± 1.7	10.3 ± 1.5		5.7 ± 1.7		
30	23.1 ± 1.3	23.5 ± 1.8	24.8 ± 1.7	23.7 ± 1.9	22.1 ± 1.9	25.3 ± 2.0	13.7 ± 2.2	
31	5.4 ± 0.6	3.3 ± 1.2	2.8 ± 1.3	5.0 ± 2.3	6.1 ± 1.7	8.9 ± 2.0	11.3 ± 2.5	
	6.7 ± 0.6	3.4 ± 1.6	3.0 ± 1.1	3.7 ± 1.8	4.5 ± 1.5	1.4	7.7 ± 2.4	

manganese. The errors in intensities are based on statistical uncertainties only. The errors in energies are calculated from the errors in locating the peak centroids as well as in the errors quoted in the values of the nitrogen calibration lines as tabulated by Marion (Ma 68).

The results of the centroid peak shift calculations are summarized in Table 6.7 and Table 6.8 for cobalt and manganese respectively. Because of the difficulty of obtaining these values as described in the section on data analysis, only relatively strong lines yield significant results. This implies that lines omitted from these tables did not show a measurable shift in centroid or that the measured shift is smaller than the error associated with it. For the shifted lines, the gamma ray energy measured at any particular filter thickness can be obtained by adding the peak centroid shift to the corresponding tabulated gamma ray energy determined from thermal neutron capture.

A typical nitrogen calibration spectrum is shown in Fig. 6.9. Compared to the cobalt and manganese spectra the lines are more symmetrical in shape. The overall resolution is best observed from the pair of doublets at about 5.3 and 5.6 keV. The peaks in each doublet are separated by 29 keV.

For energy and intensity calibrations the values used are in Table 6.9. The overall efficiency curve shown in Fig. 6.10 is derived by fitting a curve of the form

Figure 6.9

Nitrogen Calibration Spectrum

STROBEM

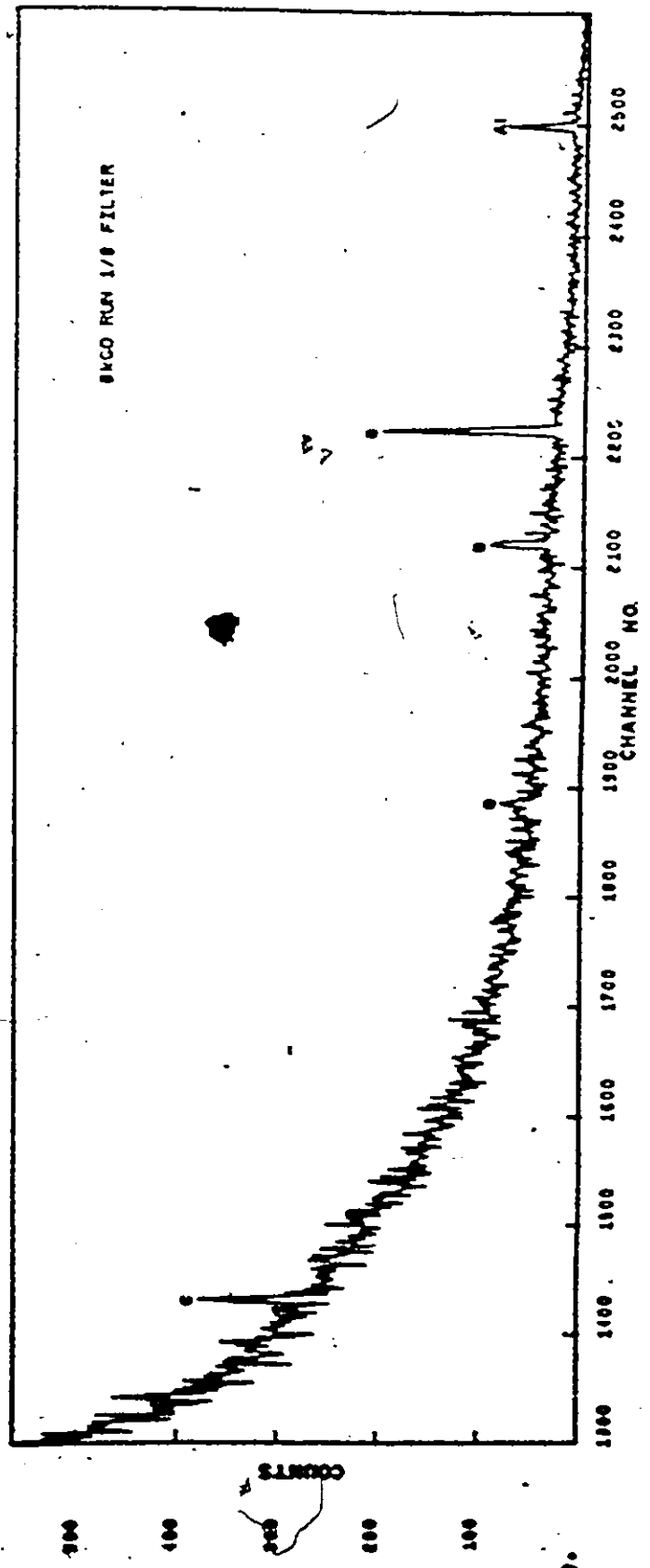
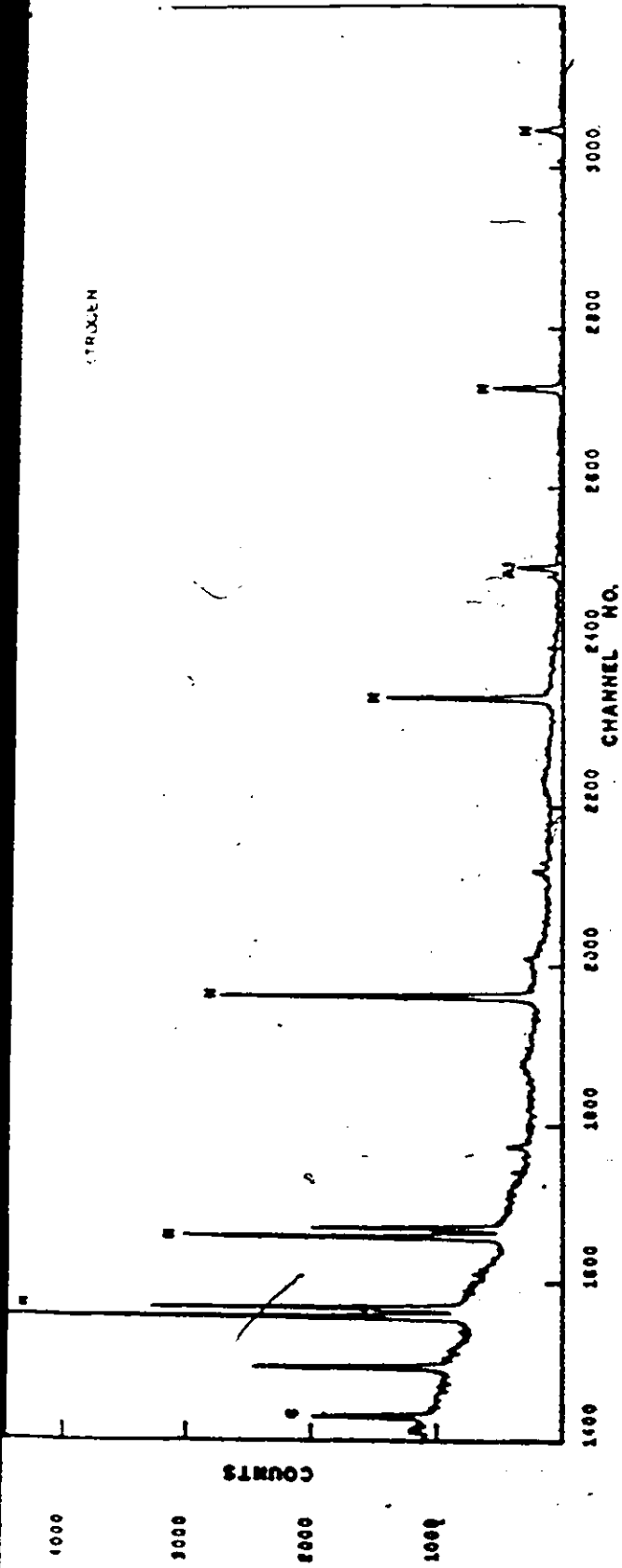
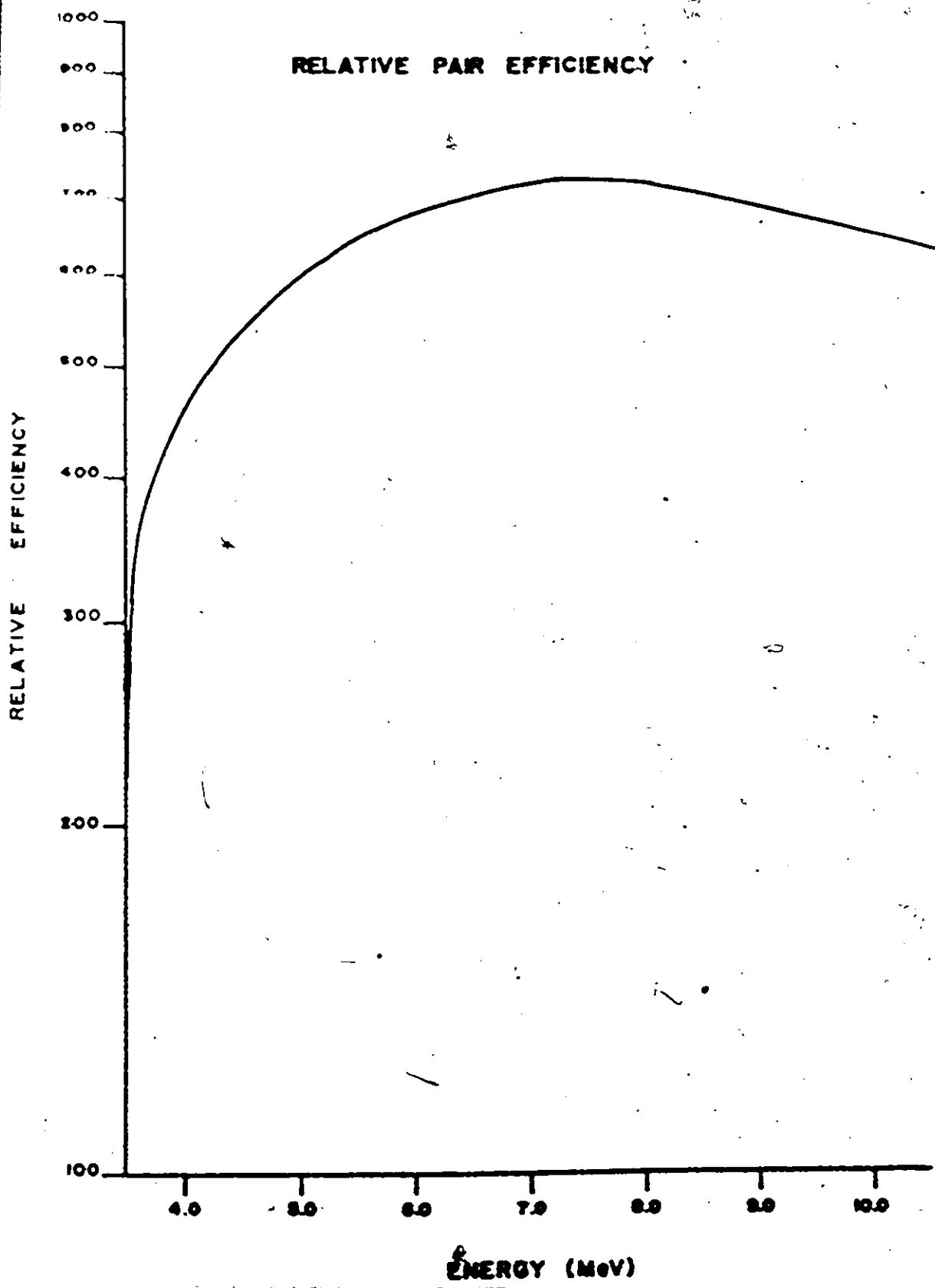


Figure 6.10

Relative Efficiency Curve

UNIVERSITY LIBRARY



RELATIVE PAIR EFFICIENCY

TABLE 6.8

Peak Centroid Shifts in Manganese Lines

Line No.	O-Filter Energy (keV)	Nominal Filter Thickness (Inch)					
		1/8	3/16	1/4	5/16	7/16	
1	7270.69	1.27 ± .20	1.10 ± .40	1.22 ± .20	0.95 ± .60	1.49 ± .40	1.30 ± .60
2	7244.04	1.47 ± .20	1.26 ± .40	1.42 ± .20	1.38 ± .20	1.91 ± .20	1.81 ± .20
3	7160.15	1.12 ± .20	1.00 ± .20	1.00 ± .20	0.70 ± .40	1.04 ± .20	1.05 ± .40
4	7058.39	1.92 ± .20	1.90 ± .26	2.15 ± .26	1.92 ± .20	2.31 ± .26	2.10 ± .30
5	6929.99	1.58 ± .42	1.49 ± .30	1.94 ± .46	2.07 ± .36	2.36 ± .42	3.05 ± .42
5A	6818.92	2.00 ± .62	1.87 ± .40	2.03 ± .56	2.04 ± .46	2.01 ± .40	2.05 ± .62
6	6784.36	1.46 ± .36	1.70 ± .30	1.96 ± .36	2.15 ± .26	2.30 ± .26	2.64 ± .42
9	6104.46	0.28 ± .40	0.50 ± .30	0.64 ± .40	0.60 ± .38	0.90 ± .42	0.80 ± .72
10	6031.02	0.80 ± .30	0.84 ± .30	1.14 ± .30	0.90 ± .36	1.46 ± .40	1.00 ± .62
14	5527.05	0.92 ± .70	1.23 ± .20	1.20 ± .20	1.22 ± .20	1.62 ± .30	1.80 ± .30
21	5066.78	0.30 ± .36	0.70 ± .42	0.53 ± .42	0.68 ± .36	1.28 ± .42	1.10 ± .68
23	5013.86	0.43 ± .20	0.88 ± .50	0.74 ± .50	0.91 ± .40	0.90 ± .52	0.95 ± .62

TABLE 6.9Nitrogen Calibration Lines

Energy (keV)	Intensity (per 100 captures)
10829.2 ± 0.4	13.3 ± 2.0
9150 ± 0.8	1.7 ± 0.2
8310.3 ± 0.7	4.4 ± 0.4
7298.7 ± 0.4	10.0 ± 0.5
6322.1 ± 0.4	18.8 ± 0.9
5562.0 ± 0.3	10.3 ± 0.5
5533.0 ± 0.3	18.8 ± 0.9
5297.4 ± 0.3	21.4 ± 1.1
5268.5 ± 0.2	30.6 ± 1.5
4508.8 ± 0.3	16.6 ± 0.8

$f(E) = e^{A+BE+CE^2}$ to all the nitrogen data. The best fit curve yields the following parameters for $4 \leq E \leq 8$ keV: $A = 4.77$, $B = 0.47 \times 10^{-3}$, and $C = -0.31 \times 10^{-7}$. Similarly the gamma ray energies were obtained after fitting the nitrogen peak centroids of the spectra obtained before and after each sample run to the equation $E_i = a + bC_i + cC_i^2$ where $\{E_i\}$ are the known nitrogen gamma ray energies and $\{C_i\}$ the corresponding peak centroids obtained from the Gaussian fit.

The main background lines observed are from (n, γ) reactions in B^{10} , C^{12} and Al^{27} which make up the component parts of the sample assembly and the through tube. A background run using the complete filter assembly with the sample replaced with an empty carbon capsule of the same dimensions as the solid cobalt sample is shown in Fig. 6.9. The lines are identified as follows: C - carbon, B - boron-10, Al - aluminum and O - oxygen. At lower energies the capture line in deuterium at 2223 keV and the inelastic line of carbon at 4445 keV are also prominent.

The activity of each of the cobalt samples was initially measured with an ion chamber. Subsequently more accurate measurements were made using a Ge(Li) detector connected to a multichannel pulse height analyzer. To reduce the dead time to a maximum of 5%, the samples were shielded with lead and were positioned relative to the counter in identical manner. The total count under the cobalt peaks which is proportional to the activity of each sample was

corrected for room background. The results are tabulated in Table 6.10.

14110778 110046

TABLE 6. 10Activity of Co Samples

Nominal Filter Thick (inches)	Normal Filter Thick (gm/cm ²)	Mwh	Relative Eff	Sum of Co Peak	Ion Chamber
0 (2 gms)	0	22.5	995.14	31107	17.5
0 (4 gms)	0	6.0	462.88	14199	5.7
1/8	0.35	15.7	117.89	12244	5.6
3/16	0.58	45.9	485.42	16395	7.1
1/4	0.74	25.7	121.95	9335	4.4
3/8	0.93	48.0	133.65	9035	5.3
1/2	1.16	72.2	127.69	8994	5.6
5/8	1.43	80.38	85.688	8157	5.6

CHAPTER VII

DISCUSSION OF RESULTS

Background Information

The cobalt-60 nucleus has 27 protons and 33 neutrons. According to the shell model the proton configuration should be $\pi(f_{7/2})^{-1}$, a proton hole in the 28-particle closed shell. This is confirmed for Co^{59} by the measurements of Blair and Armstrong (Bl. 65).

The analysis of the nickel isotopes by Cohen et al (Co 62, Co 64) showed that the single particle neutron levels in the region $A \approx 60$ are arranged in order of increasing energy as $2p_{3/2}$, $1f_{5/2}$ and $2p_{1/2}$. Hence it is expected that the ground state and the low-lying levels of Co^{60} can be described by coupling a proton hole $\pi(f_{7/2})^{-1}$ with a neutron hole $\nu(p_{3/2})^{-1}$ resulting in levels with $J^\pi = 2^+, 3^+, 4^+, 5^+$. The ground state of Co^{59} has spin and parity $J^\pi = 7/2^-$. Capture of s-wave neutrons leads to intermediate states with $J^\pi = 3^-$ and 4^- which de-excite by E1 transitions to final states with the same spins and parities as the $\pi(f_{7/2})^{-1}\nu(p_{5/2})^{-1}$ multiplet.

The ground state has been assigned $J_f^\pi = 5^+$ by Dobrowolski et al (Do 56) and the first excited state $J_f^\pi = 2^+$ (Sh 66, Ro 71). Furthermore, the results of Robertson (Ro 71) based on his analysis of magnetic moment

measurements and data from the $f_{7/2}$ proton pick-up reaction, $Ni^{61}(d, He^3)Co^{60}$, indicate that both these states contain mainly a $p_{3/2}$ neutron amplitude.

Extensive research on the Co^{60} nucleus has been performed using (n, γ) and (d, p) studies. The most recent gamma ray spectra using Ge(Li) detectors have established an energy level scheme (Sh 66, Pr 66, Se 71, Ro 71). Spin measurements on the low-lying levels have been carried out (Me 69, St 72, Ro 72) and resonance capture experiments have also been done (Wa 66, Pr 67, Wa 68, Au 68). The latest spin assignments on levels up to an excitation energy of 2.31 MeV are shown in Table 7.1.

The levels of Mn^{56} have also been studied by several authors. The high energy gamma rays following neutron capture have been analyzed using a magnetic pair spectrometer (Ba 53), Compton spectrometer (Gr 58) and more recently high resolution Ge(Li) detectors (Me 70, As 71, Ra 67, Hu 66). The fluctuation of the gamma ray partial widths was first noted in the resonance neutron capture experiment of Kennett et al (Ke 58) in Mn^{55} . Comprehensive studies of Mn^{56} levels have also been carried out from (d, p) reaction (Da 61, Co 68) and from (d, α) reaction (Ke 72).

The total neutron capture cross-section of Mn^{55} has been investigated and analyzed in terms of the R-matrix theory (Kr 55). Cote' et al (Co 64) using the R-matrix

TABLE 7.1

Final State Spin Assignments in Co⁶⁰

Line No.	J ^π (Ta 73)	J ^π (Me 69)	J ^π (St 72)	J ^π (Ro 72)
1	5 ⁺	5 ⁺	5 ⁺	
2	2 ⁺	2 ⁺	2 ⁺	
3		4 ⁺	3 ⁺	4
4		3 ⁺	3 ⁺	3
5	5	3 ⁺ , 5 ⁺ , (4 ⁺)	5 ⁺	
6		3 ⁺	3 ⁺	3, 4
7	2	3 ⁺ , 4 ⁺ , (2 ⁺)	3 ⁺ , 4 ⁺	
8		3 ⁺	3 ⁺	3
9		4 ⁺	3 ⁺	4
10		3 ⁺ , 4 ⁺	3 ⁺ , 4 ⁺	4
15		3 ⁺ , 4 ⁺	4 ⁺	4
18			3, (4)	3
20		3, 4	3, 4	4
21			3 ⁺ , 4 ⁺	4
28			2, 3, 4	

analysis of Firk, Lynn and Moxon (Fl 63) were able to fit the experimental total neutron cross-section, from 0.01 eV to 15 keV.

Mn⁵⁵ has 25 protons and 30 neutrons. The simple shell model places the protons in the $1f_{7/2}$ level and the neutrons in the $2p_{3/2}$ level (Pr 62). The ground state spin and parity is $I^{\pi} = 5/2^{-}$. Capture of s-wave neutrons results in intermediate states with $J^{\pi} = 2^{-}$ and 3^{-} .

The spins and parities of the lowest three states were established by the atomic magnetic resonance measurements of Childs et al (Ch 61). The most recent spin assignments for the low-lying levels up to an excitation energy of 1.24 MeV are summarized in Table 7.2.

Both nuclei have been investigated for a direct capture component in the neutron radiative capture process. Search for direct capture in this mass region is pursued because the s-wave neutron strength function is maximum and because the Lane and Lynn theory predicts a large component in the region of the p-orbitals. In this region the 2p orbitals are being filled.

The first attempt to measure the direct capture contribution in Co⁶⁰ was carried out by Wasson et al (Wa 66) by looking for an asymmetry in the ratio $R(E_n) = \sigma_{n\gamma f}(E_n) / \sigma_{n\gamma}(E_n)$ ($\sigma_{n\gamma f}(E_n)$ is the partial cross-section; $\sigma_{n\gamma}(E_n)$ is the total cross-section; E_n is the neutron energy captured)

TABLE 7.2

Spin and Parity - Low-Lying Levels in Mn⁵⁶

Excitation Energy (keV)		Spin and Parity J		
(Ke ⁷²)	(Me ⁷⁰)	(Me ⁷⁰)	(As ⁷¹)	(Ke ⁷²)
0	0	3 ⁺	3 ⁺	3 ⁺
25	26	2 ⁺	2 ⁺	
107	110	1 ⁺	1 ⁺	1 ⁺
	212	2 ⁺ , 4 ⁺	4 ⁺	
214	215	1 ⁺ , 2 ⁺	2 ⁽⁻⁾	
334	336	2 ⁺ , 3 ⁺ , 4 ⁺ , 5 ⁺	4 ⁺ , 5 ⁺	5 ⁺
	341	2 ⁺ , 3 ⁺	3 ⁺	
449	454	2 ⁺ , 3 ⁺ , 4 ⁺	4 ⁺	3 ⁺
485	486	2 ⁺ , 3 ⁺	(2, 3, 4) ⁺	
707	717			3 ⁺
747			(3, 4) ⁺	
	840			
	1165	1 ⁺		
1245	1237			

due to direct-resonance interference. The result was not conclusive since level-level or direct-resonance interference could explain the data.

The latest measurements on the direct capture cross-section for the Co^{60} ground state were performed by Wasson et al (Wa 68) and Auchampaugh (Au 68). Both used time-of-flight techniques and Ge(Li) detectors to study the variation of intensity as a function of neutron energy.

Wasson et al (Wa 68) studied forty lines and concluded that only the ground state required a direct capture component to fit the experimental data. They deduced a value 9.2 ± 3.0 mb. Auchampaugh (Au 68) investigated nine transitions and also concluded that only the ground state has a nonzero value for potential direct capture. He found $\sigma_{\text{dir}} = 5.5 \pm 1.5$ mb.

Both claimed that the direct component could be simulated by a $J^{\pi} = 4^{-}$ bound state resonance at -1000 eV. However since the other lines did not require the existence of this bound state to fit the interference patterns this possibility was ruled out. That only the ground state contains a direct component implies that it is the only level with sufficient strength (i.e. large enough matrix element) to be measurable.

In manganese the search for direct capture effects was started by Wasson et al (Wa 64) who first showed that

the (n, γ) and (d, p) transition energies were closely matched. As in cobalt the first attempt to measure a direct capture component in the ground state was made by looking for asymmetry in the partial radiative cross-section due to direct-resonance interference (Wa 65). The result was not conclusive since both types of interference, level-level and direct-resonance, could explain the observed asymmetry. An upper limit of 160 mb on the direct capture cross-section at 1 eV was deduced.

A second attempt to measure σ_{direct} using time-of-flight techniques and a high resolution Ge(Li) counter was made recently by Auchampaugh (Au 68). He analyzed a total of 11 lines and found no conclusive evidence for a direct component in any of them. The level-level interference was sufficient to explain the variation of $R(E_n)$. Where an upper limit on σ_{direct} was deduced, the theoretical prediction was 20-30 times larger.

Thus except for the cobalt ground state, no direct capture component in the low-lying levels of Co^{60} and Mn^{56} could be found contrary to the prediction of the direct capture model.

Flux Model Calculations and Measured Activity

In the following discussions the experimental data are interpreted in terms of theoretical results based on the flux model calculations discussed in Chapter III (Boron Filter Technique).

To check the adequacy of the assumptions which were made and the expected accuracy of the results, a comparison is made between the measured and calculated activities of the cobalt samples.

The sample activity is given by the expression $A = k \int_E C_n(E) dE$ where $C_n(E)$ is the total neutron capture which is dependent on the boron filter thickness, sample size and geometry. (See Chapter III for Quantitative Definition.) The results are shown in Table 7.3. The agreement between the calculated and the measured values is excellent thus proving the validity of the flux model used.

3. Statistical and Nuclear Structure Effects

In cobalt the (d,p) results of Enge (^{En 60}) show a good correspondence with the low-lying levels populated in the (n, γ) reaction except for a few above 1.5 MeV which are not seen in the radiative capture. In manganese, Hughes et al (^{Hu 66}) observed that of 96 levels seen in thermal neutron capture 46 lines are common with the (d,p)

TABLE 7.3Activity of the Cobalt Samples

Nominal Filter Thickness (inch)	Measured Activity (arb units)	Calculated Activity (arb units)
1/8	23.2	26.5
3/16	10.6	9.4
1/4	10.8	9.6
3/8	5.6	4.5
1/2	3.7	3.8
5/8	3.0	3.1

results (Da 61). The fact that both reactions favor de-excitation to identical levels is suggestive of some similarity between them.

A gross measure of this similarity is quantitatively indicated by the correlation coefficient given by the expression

$$\rho = \frac{\sum (x_i - \bar{x})(y_i - \bar{y})}{\left[\sum (x_i - \bar{x})^2 \sum (y_i - \bar{y})^2 \right]^{1/2}}$$

where x and y are the (n,γ) and (d,p) strengths respectively.

This quantity was determined for thermal and resonance captures (Pr 66, Pr 67) in cobalt but yielded insignificant values. For manganese a significant correlation coefficient of 84% was calculated by Hughes et al (Hu 66) using thermal neutron capture results. Resonance capture studies (Pr 67) also showed correlation coefficients greater than 70% for each of the thermal, 1098 eV and 2355 eV captures. It was observed that the high correlation was due to the strong transition to the level at 207 keV which is believed to contain the largest fraction of single particle p -states.

Comfort (Co 68) also looked at these correlations using his measured (d,p) strengths and found $\rho = 44\%$ for the thermal spectrum. Contrary to the previous results (Pr 67) he observed no significant correlation with the resonance capture data. This contradiction stems from the difference

in the (d,p) strengths calculated by Comfort^(Co 68) and Dalton et al^(Da 61). Comfort used the DWBA method in his analysis whereas Dalton used the plane wave approximation which is now believed to be inaccurate.

From the viewpoint of the direct capture model it is possible to find no correlation between thermal or resonance capture data with the (d,p) intensities if the proper conditions are not met. According to the results shown in Appendix 4, correlation between (n, γ) and (d,p) intensities can only be significant when the ratio of the fractional contribution of the intermediate states is $r = f_{J_1}/f_{J_2} = (2J_1 + 1)/(2J_2 + 1)$. For cobalt and manganese the proper values of r are 0.78 and 0.71 respectively.

The present work attempts to attain this ratio by shaping the neutron flux. It is expected that as the filter thickness was changed to approach the proper value of r, the correlation coefficient would become more and more significant.

Using Enge's (d,p) data for cobalt^(En 60) correlation coefficients were calculated for each filter. The observed correlation was not only insignificant but also showed hardly any change from one run to another.

It is possible that because the angular distributions and (d,p) intensities were calculated using the plane wave approximation, the quoted values may be inaccurate. Taylor^(Ta 73) re-analyzed Enge's data using the distorted-wave-Born-approximation and when his results were used to

calculate ρ , the conclusion was still negative. Δ

More recently the $\text{Co}^{59}(\text{d},\text{p})\text{Co}^{60}$ experiment was repeated with superior resolution (Ta 73). Using preliminary results up to 1 MeV, a similar conclusion was arrived

For manganese, the correlation coefficient was calculated for each filter thickness for 24 lines up to an excitation energy of 2.390 MeV using the (d,p) results of Comfort (Co 68). The results are shown in Table 7.4. At 0 filter the correlation coefficient is close to the value using thermal neutron capture data. No maximum value of ρ is found.

The ratio of the average reduced intensities $\langle I_{\gamma}/E^3 \rangle$ for transitions to levels populated by angular momentum transfer $l_n = 1$ to $l_n = 3$ has been measured to be ≈ 8 (Pr 66) for cobalt. This was taken to be a manifestation of the direct capture process in (n, γ) reactions. The results of the present measurements showed this ratio to be about 5 for the thin filter. It dropped to 2.9 for the thickest filter.

Since no conclusive gross evidence was found for the direct capture model it was decided to consider the data in the context of the statistical model. If the radiative capture were strictly a compound nucleus mechanism, then there should be no preference of decay to any excited neutron or proton configuration. A consequence of this

TABLE 7.4

Effective Degree of Freedom for Co⁶⁰

Nominal Filter Thickness (Inch)	ν_{eff} Wilets	ν_{eff} Case (1)	ν_{eff} Case (2)
0	1.30 ± .10	1.05	1.33
1/8	1.06 ± .10	0.88	1.11
3/16	1.09 ± .06	1.03	1.28
1/4	1.12 ± .10	1.24	1.51
3/8	1.06 ± .12	1.66	1.95
1/2	1.59 ± .14	2.59	2.82
5/8	1.74 ± .50	4.30	4.24

model is that the distribution of the reduced intensities following capture from one particular resonance should follow the Porter-Thomas distribution for the primary gamma rays.

However since several resonances contribute to each transition, the distribution will be that of a weighted average of four Porter-Thomas distributions corresponding to E1 decay to the different final state spins. A quantitative comparison with the experimental data can be made by considering an effective degree of freedom which is defined by $\frac{2}{\nu_c} = \frac{\sigma^2}{\langle X \rangle^2}$ where σ is the standard deviation, $\langle X \rangle$ is the mean and ν_c the effective degree of freedom. For the experimental data a biased estimate is given by Willetts formula (Ly 69)

$$\frac{\sigma^2}{\langle X \rangle^2} = \frac{\langle X^2 \rangle - \langle X \rangle^2}{\langle X \rangle^2} = \frac{2}{\nu_{\text{exp}}}$$

$$\nu_{\text{exp}} = \frac{2\langle X \rangle^2}{\langle X^2 \rangle - \langle X \rangle^2} \quad \text{where } X = I\sqrt{E^3}$$

A theoretical calculation of the effective degree of freedom assuming the statistical model is shown in Appendix 4. The resulting relationship is given by

$$v_{th} = 2 \left[w_2 \left(\frac{2}{v_2} + 1 \right) f_3 g^2 + w_3 \left(\frac{2}{v_3} + 1 \right) g^2 + \right.$$

$$\left. w_4 \left(\frac{2}{v_4} + 1 \right) g^2 + w_5 \left(\frac{2}{v_5} + 1 \right) f_4 g^2 - 1 \right]^{-1}$$

w_i is the weighting due to the level density of the possible final states

v_i is the degree of freedom of the distribution of the reduced intensities of transitions to the i^{th} final state

g is equal to $(w_2 f_3 + w_3 + w_4 + w_5 f_4)^{-1}$

Comparison of the theoretical and experimental effective degree of freedom is shown in Table 7.4 for cobalt. Two cases are considered: 1. The level density of the final states is assumed to follow the statistical model so that $\rho(J) \propto e^{-J(J+1)/2\sigma^2}$. 2. The level density is assumed weighted as follows: $w_2 = w_5 = 0.1$ and $w_3 = w_4 = 0.4$. This weighting is based on the known level spins.

The results show a fair agreement for the thin filter data (i.e. $v_c < 2$). However there is a big discrepancy for the thick filter data.

There are two possible explanation for this deviation:

1. the weighting used due to differences in densities of levels of different spins is wrong,
2. a non-statistical effect is being observed.

The sensitivity of the results to the weighting used can be seen by comparing the two cases considered. The

spin dependence of the level density is obtained by using a spin cut-off factor of 3.5, a value suggested by Gilbert et al^(Gi 65) for mass numbers in the region $A \approx 60$. This results in $w_2 = 0.293$, $w_3 = 0.294$, $w_4 = 0.243$ and $w_5 = 0.170$. Looking at the actual data however there are at most two levels of spins 2 and 5. From the data $w_2 = w_5 = .06$. Therefore it is very unlikely that the weighting using the spin dependence of the level densities is representative of the actual situation. This is reflected in the slightly better agreement between ν_{exp} and ν_{th} (case 2) at least for the thin filters.

A more qualitative comparison between the distribution of the reduced intensities with ψ -distribution with one two, and three degrees of freedom is shown in Fig. 7.1. The experimental data show $1 < \nu_{exp} < 3.0$.

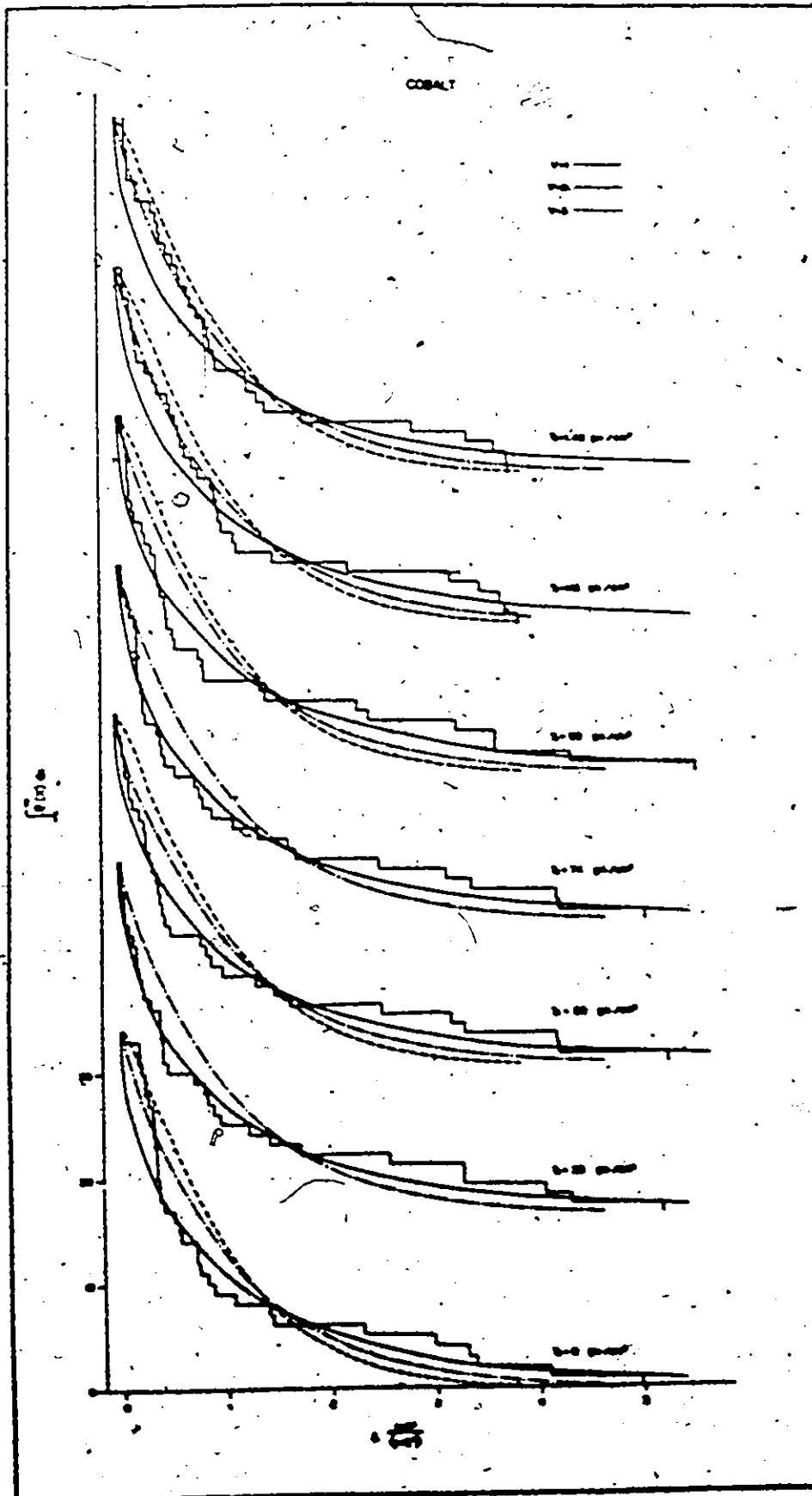
For manganese the effective degree of freedom is given by

$$\nu_{th} = 2 \left[w_1 \left(\frac{2}{\nu_1} + 1 \right) f_1^2 g^2 + w_2 \left(\frac{2}{\nu_2} + 1 \right) g^2 + w_3 \left(\frac{2}{\nu_3} + 1 \right) g^2 + w_4 \left(\frac{2}{\nu_4} + 1 \right) f_3^2 g^2 - 1 \right]^{-1}$$

where the different parameters are defined as in the case of cobalt. Assuming the same spin cut-off factor of 3.5

Figure 7.1

Integral Probability Distribution of the Reduced Intensities
of the Cobalt Lines



then $w_1 = 0.209$, $w_2 = 0.279$, $w_3 = 0.280$ and $w_4 = 0.232$.

The theoretical v_{th} was calculated assuming the above dependence of level density on spin and also uniform weighting, the latter probably being one representative of the data. The results are also given in Table 7.5. The uniform weighting agrees better with the values deduced from the experimental data.

The integral probability of the reduced intensities i.e. $\int_x P(X)dx$ where $X = (I/E^3)/\langle I/E^3 \rangle$ plotted against X , is shown in Fig. 7.2. These pictures are consistent with the v calculated from the data.

In the context of the statistical model it is interesting to consider the ratio of the average intensity of the levels with spins 2 and 5 to the average intensity of levels with 3 and 4 for cobalt. In the limit of equal contribution for the intermediate states to the four possible final state spins this ratio would be 0.5. Using the intensities of the assigned (spin) levels for the 5/8 inch filter, this ratio is 0.6. For manganese the corresponding ratio (i.e. $I_{1,4} / I_{2,3}$) is 0.4 for the thermal capture, 0.76 for the 1/8 inch filter and 0.5 for the 1/4 inch filter.

4. Resonance Partial Widths and Direct Amplitude

The deduced energies of the Mn⁵⁶ levels (see Chapter III Experimental Results) are in good agreement with other results (Mn 67, Mn 70) with the exception of three lines

Figure 7.2

Integral Probability Distribution of the Reduced Intensities
of the Mn⁵⁶ Lines

MANGANESE

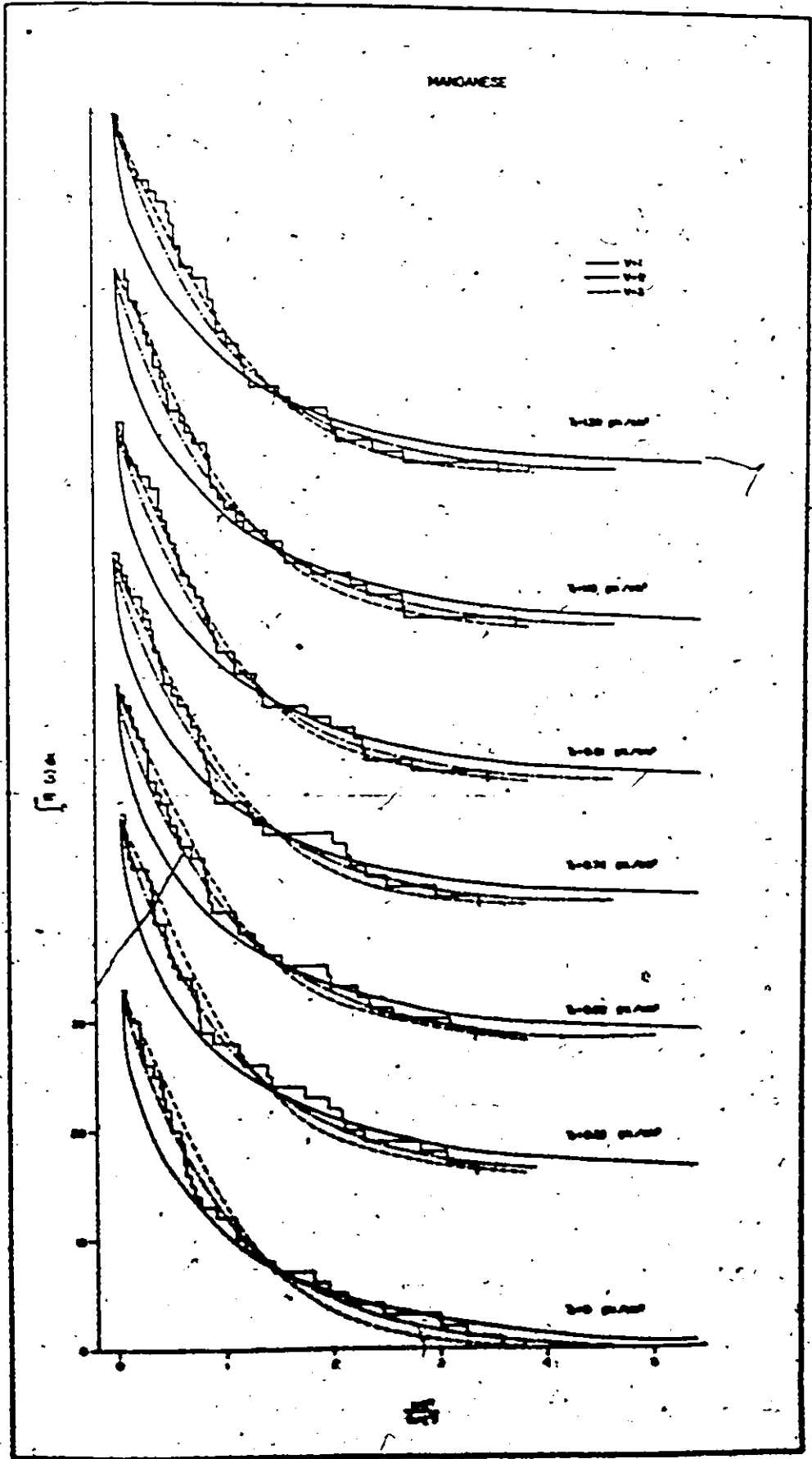


TABLE 7.5

Statistical Properties Deduced from the Mn⁵⁶ Lines

B ¹⁰ Filter Thickness	v_{eff} Wilets	v_{eff} Theory (a)	v_{eff} Theory (b)	Correlation Coef
0	2.22 ± .22	1.73	2.28	44.1
1/8	2.40 ± .30	1.42	1.93	31.6
3/16	2.58 ± .32	1.72	2.27	30.7
1/4	2.72 ± .39	1.87	2.44	34.7
5/16	2.94 ± .40	2.10	2.68	37.1
7/16	2.75 ± .38	2.47	3.03	40.2
1/2	3.09 ± .55	2.67	3.20	43.2

Notes:

1. (a) statistical spin dependence is assumed.
2. (b) uniform weighting is used.

at energies 5134, 4935, and 4709 keV which were observed by Meffema (Me 70) but are not seen in this work.

A thermal neutron capture spectrum also obtained using the through-tube facility differed slightly with the o-filter data (cadmium filter used but no B^{10}). In particular the ground state intensity has increased from 3.9% to 5.0% with the cadmium filter surrounding the sample. Since it has $J_f = 3^+$, any of the resonances can deexcite to this final state. The lower intensity of the ground state at thermal capture compared to the o-filter data may be due to destructive level-level interference.

Although the ground state intensities of the different filter thicknesses are considerably different from the thermal intensity, the variation observed from one filter thickness to another is not as dramatic. The maximum value of 9.5% is observed when the filter thickness is 3/16 inch. This decreased to 8.1% for the 1/2 inch filter. Relative to the o-filter data, a centroid shift of 1.27 keV is measured for the 1/8 inch filter. As in the intensity variation the centroid shifts for the different filter thicknesses are not too different.

A line which is not seen in the thermal capture spectrum but which is observed with increasing intensity with filter thickness has an energy 6818.6 keV. Its

intensity is 0.15% for the 0-filter data. For the 1/8 inch filter its intensity is 1.7% and for the thickest filter 3.98%. A centroid shift of 2.0 keV is also measured and is almost constant from one filter thickness to another.

The centroid shifts of several strong lines were determined. Most of them show a shift of about one keV. There is no appreciable change in the observed value from one filter thickness to another. On the other hand lines 9 and 23 show negligible shifts.

For cobalt the present data on the high energy gamma ray lines are in good agreement with the recent measurements (Sh 66, Wa 68). The energies and intensities for the 0-filter data compares favorably with the thermal capture results. The similarity of these two results may be due to the dominance of the 132 eV resonance. In manganese no such dominant resonance exists so that the observed difference between the thermal and 0-filter results is not surprising.

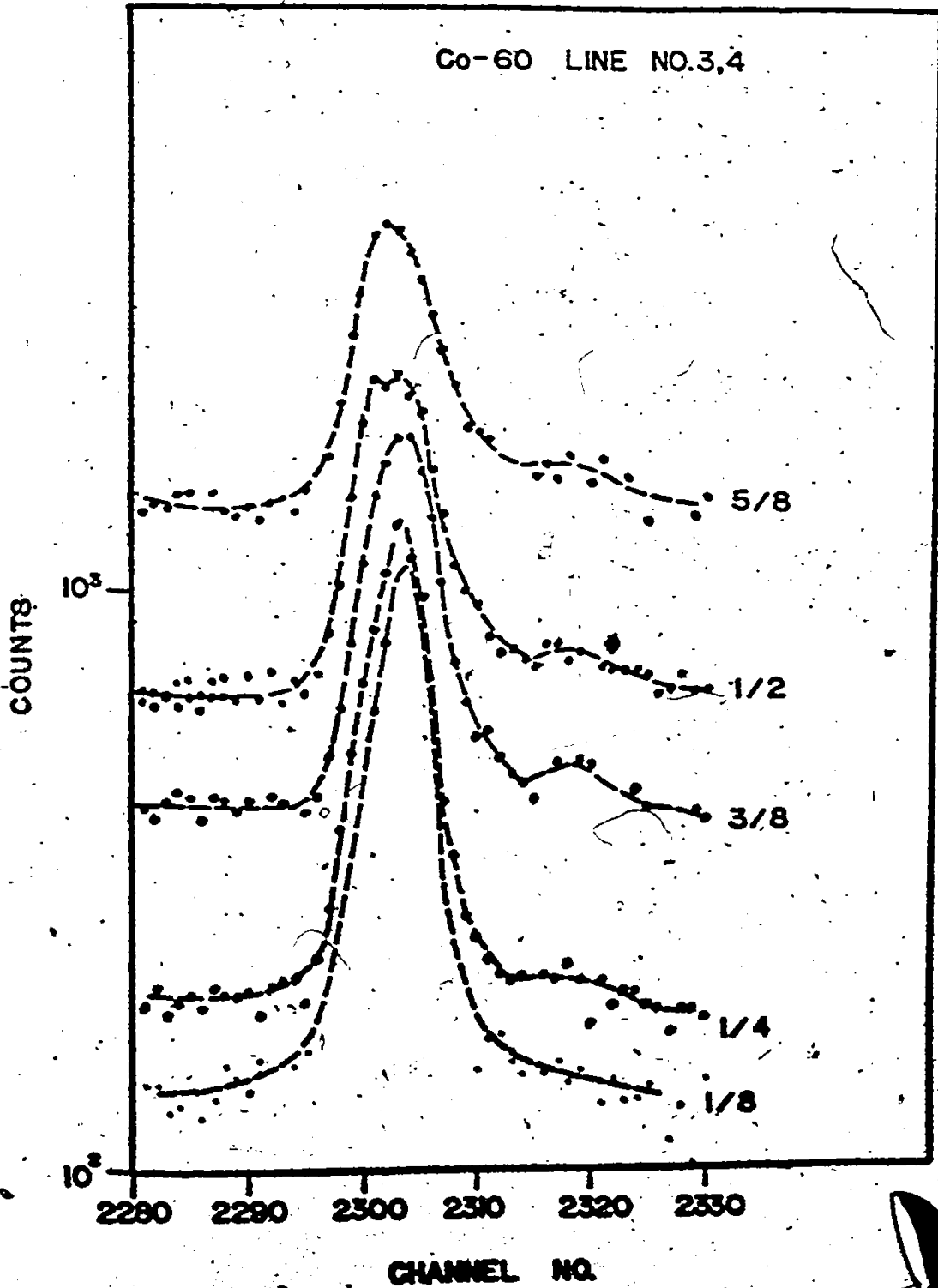
The complex lines nos. 3 and 4 although not well-resolved clearly show a change in relative intensities with filter thickness. This is shown in Fig. 7.3. The other complex lines 11^c and 25^c are difficult to resolve and the total intensities are quoted.

Several strong lines of Co⁶⁰ were also monitored for centroid shifts. Although most of them show shifts of the order of a few keV, two of these lines (e.g. 15, 18)

Figure 7.3

Relative Intensity Variation of the Cobalt Doublet Lines
#3, 4 with Filter Thickness

Co-60 LINE NO.3,4



show very small shifts indicating the strong influence of a low energy resonance. On examination of their intensity patterns, it is found that they follow the 132 eV contribution. These observations prove that the observed shifts are not artificial and also support the reasonableness of the calculated fractional contributions of the different resonances.

One line that shows a very dramatic change in intensities and centroid shifts with filter thickness is the first excited state. This line is hardly observed in thermal capture. For the 1/8 inch filter it has an intensity of .08%. For the 5/8 inch filter its intensity increases to 2.3%. The observed centroid shifts start from 3.51 keV to 6.85 keV for the 1/8 inch and 5/8 inch filter respectively. Both parameters are monotonically increasing with filter thickness.

The behavior of the first excited state can be easily explained qualitatively. Since it has $J_f = 2^+$, only capture states of $J = 3^-$ can contribute by E1 deexcitation. The first capture state of this spin is a bound state at -268 eV. This is followed by a positive energy resonance at 5015 eV.

The fractional contribution of the bound state when there is no boron filter is 19.6%. This drops to 5% for the 1/8 inch filter. On the other hand, the 5015 eV resonance contributes 1.8% for the 0 filter and increases

to 3.4% for the 1/8 inch filter. For the 3/16 inch filter, the latter is higher by a factor of 1.6, and for the 5/8 inch filter, a factor of 8. In fact the total contributions of all positive $J = 3^-$ resonances is 13 times larger than that of the negative energy resonance.

It is plain that the considerable change in intensities and centroid shifts can only be due to the high contribution of the $J = 3^-$ positive resonances. A contribution from high energy resonances is also evident from the centroid shifts and skewness of the line shapes of other lines with thick filters.

The energy level at 543 keV (line #7) is interesting since there seems to be a discrepancy as to its spin. Mellema et al^(Me69) considered a spin of $J_f = 2$ but this assignment was later ruled out^(St 72) on the basis of the resonance capture results at 132 eV^(Pr 67) which assigned a nonzero intensity for this transition. The more recent experiment of Wasson et al^(Wa 68) however show that this line is undetectable. This is possible if the transition from the 132 eV state ($J = 4^-$) is not allowed or is weak because of the Porter-Thomas fluctuation which favors small width. Hence it is not very conclusive that this level can only have spin 3 or 4.

The intensity of this line is seen to follow the increase in the fractional contribution of the $J = 3^-$ resonances. The centroid shift measured for the 1/8 inch filter is 2.82 keV which indicates a significant capture from high-

energy resonances. For the 5/8 inch filter the shift is 5.10 keV. The shifts are smaller compared to the first excited state but greater than the ground state. These observations are consistent with neutron capture by 3^- resonances making transitions to a 2^+ final state. However the possibility of $J = 4^-$ intermediate states cannot be ruled out since similar observations may result if the partial width of the higher energy $J = 4^-$ resonances are much bigger than that of the 132 eV resonance.

The ground state has $J_g = 5^+$. Therefore only intermediate states of spin 4^- can populate it by E1 decay. The nearest resonances are the 132 eV, the 4322 eV, 10600 eV and 16900 eV. The 132 eV is the strongest resonance. At filter thickness of 1/8 inch its fractional contribution is calculated to be 88%. This decreases to 41% with a 5/8 inch filter. Thus it dominates over all the other resonances. This implies that the intensity and the energy shift which are sensitive to the contribution of the different resonances will be mainly determined by this resonance for the thin filter measurements. As the neutron flux is peaked towards the kilovolt region, the 4322 eV and the higher resonances could play a significant role depending on their widths, resulting in centroid shifts of the order of kilovolts. This picture is consistent with the observed data.

A rough estimate of the intensity contribution of the resonances above 132 eV to the ground state can be made

by considering the 1/8 and 5/8 inch filter line intensities. For the 5/8 inch filter the fractional contribution of the 132 eV resonance, the high energy $J = 4^-$ resonances, and the $J = 3^-$ resonances are 41%, 20% and 39% respectively. The total intensity of the lines considered is 64.2%. Therefore the contribution of the higher $J = 4^-$ resonances to the total is 12.8%. The intensity contribution of the 132 eV resonance (based on the 1/8 inch filter data) to the ground state is 2.9%. Thus its contribution for the 5/8 inch filter is 1.2%. The remaining 1.7% intensity of the ground state for the 5/8 inch filter must be from the high resonances. Hence $(I_{ij}/I_{Total})_{high} = 13%$, which is the weighted contribution of these resonances.

This rough estimate gives a value which seems to be in discrepancy with the chopper data which assigned a very small amplitude for the 4322 eV resonance (Wa 68). Wasson et al deduced $\Gamma_{ij}^{1/2}(4 \text{ keV}) = -.092 \text{ eV}^{1/2}$ while Auchampaugh calculated $\Gamma_{ij}^{1/2}(4 \text{ keV}) = +.037 \text{ eV}^{1/2}$. Because of this disagreement it was decided to analyze the ground state data using the method of non-linear least squares fit to find the best values of the resonance partial widths and possible direct capture amplitude.

One weakness in their result is that high energy resonances were ignored in their interpretation of the intensities. Consider the case of no direct component.

Then the partial cross-section at low energy (eV region) can be written as

$$\sigma_{\gamma j} = \left[\sum_{r=1}^{\infty} \frac{(\Gamma_{nr}^0 \Gamma_{\gamma r j})^{\frac{1}{2}}}{E - E_r - i \frac{\Gamma_r}{2}} \right]^2$$

$$= \left[\frac{(\Gamma_{n1}^0 \Gamma_{\gamma 1 j})^{\frac{1}{2}}}{E - E_1 - i \frac{\Gamma_1}{2}} + \sum_{r=2}^{\infty} \frac{(\Gamma_{nr}^0 \Gamma_{\gamma r j})^{\frac{1}{2}}}{-E_r} \right]^2$$

where $E_1 \approx 132$ eV, and $E_r \gg E$, $r \geq 2$ since E_r is much bigger than either E or Γ_r . The second term is a constant and could easily simulate the direct component. These authors did not consider resonances above 4322 eV. The partial widths for the first two $J = 4^-$ resonances obtained by them not only disagreed in magnitude but also in sign.

The present experiment offers an independent determination of the direct component. Since only the ground state seems to show this effect, careful attention was focused on it. There was no reason to investigate the other lines since this component is not discernible in previous measurements.

The experimental data yield two significant pieces of information for a given filter thickness - the line intensity and the centroid shift of a particular radiative transition to a given level. The calculation of the corresponding theoretical line intensity and centroid shift yields the parameters of interest i.e. partial

radiative widths and direct capture amplitude. These are calculated from the two equations:

$$I_{\gamma j} = \frac{\int C_{nj}(E) dE}{\int C_n(E) dE}$$

$$\Delta E_j = \frac{\int EC_{nj}(E) dE}{\int C_{nj}(E) dE} - \frac{\int EC_{no}(E) dE}{\int C_{no}(E) dE}$$

where $C_{nj}(E)$ is the capture from all contributing resonances resulting in decay to the j^{th} state (i.e. ground state); $C_n(E)$ is the total number of captures from all resonances as defined previously and C_{no} refers to the 0-filter data.

The parameters of interest are contained in C_{nj} through the partial cross-section $\sigma_{\gamma j}(E)$. More explicitly

$$C_{nj}(E) = C_n(E) \frac{\Gamma_{\gamma j}(E)}{\Gamma_{\gamma}(E)}$$

$$\Gamma_{\gamma j}(E) = \gamma \lambda \lambda_1 g(S) \left[A_1 + \sum \frac{\Gamma_{ni}^{0 \frac{1}{2}} \Gamma_{\gamma j}^{\frac{1}{2}}}{E_i - E - i\Gamma_{\frac{1}{2}}} \right]^2$$

where the subscript 1 refers to evaluation of that parameter at 1 eV.

The unknown parameters were determined by the non-linear least squares method. A computer code based on a direct search technique (Po 62) was used to locate the minimum chi-square.

In the initial calculations the amplitudes were deduced by considering the line intensity variation only. It was also assumed on the basis of the chopper data

that resonances above 4322 eV could be ignored. Then assuming a negative sign for the 4322 eV, the best fit parameters were as follows: $A_1 = 1.52 \times 10^{-4} \text{ eV}^{\frac{1}{2}}$, $\Gamma_{ij}^{\frac{1}{2}}(132) = .077 \text{ eV}^{\frac{1}{2}}$, $\Gamma_{ij}^{\frac{1}{2}}(4322 \text{ eV}) = -0.249 \text{ eV}^{\frac{1}{2}}$. When a positive amplitude was tried for the 4322 eV a negligible direct capture amplitude ($10^{-6} \text{ eV}^{\frac{1}{2}}$) was found while the 4322 eV amplitude increased to $+0.31 \text{ eV}^{\frac{1}{2}}$. The 132 eV amplitude was $.079 \text{ eV}^{\frac{1}{2}}$. This preliminary result gave partial widths which are of the right order of magnitude compared to the initial estimates based on the 1/8 inch and 5/8 inch filter data. These results show that the 4322 eV resonance is not so small as suggested by the time-of-flight data and also indicate that the direct amplitude could be explained with resonance interference.

Following these preliminary results it was decided to consider resonances up to 21 keV and to deduce the resonance widths using both intensity and centroid shift information. The additional constraint due to the measured line shifts should yield more accurate results.

The best fit parameters are shown in Table 7.6 together with the parameters deduced by Wasson et al (Wa 68) and Auchampaugh (Au 68). Two sets of parameters were found which could reproduce the experimental data. In case (a) the 16.9 keV resonance amplitude is negative. In case (b) the 10.7 keV amplitude is negative. In either case the 132 eV amplitude is hardly affected.

TABLE 7.6

Comparison of the Deduced Resonance Parameters with
the Time-of-Flight Data

	Direct Capture (mb)	Resonance Energies (eV)		
		4322	10700	16920
Wasson et al (Wa 68)	9.2 ± 3.0	+0.92	0	0
Anchutepaugh (An 68)	5.5 ± 1.5	$+0.112 \pm .011$	$+0.037 \pm .043$	0
Present Work (a)	0	$+0.109 \pm .001$	$+0.323 \pm .012$	$+0.228 \pm .018$
Present Work (b)	0	$+0.109 \pm .001$	$+0.232 \pm .020$	$-0.001 \pm .102$

Note: (a) and (b) are two possible combinations which can reproduce the data.

Both calculations include geometry and multiple scattering effects as discussed in text. The quoted uncertainties do not include errors in the resonance parameters used.

to fit the data with a direct capture component resulted in a negligible amplitude.

The sensitivity of these calculations to geometry considerations has been considered. Three possible cases were studied. In each case the signs of the 10700 eV and 16920 eV resonance amplitudes were alternated. These cases are (1) the flux was assumed to be normally incident on the filter and sample, (2) the actual geometry of each sample and filter was considered; (3) the effects of multiple scattering was included. The results are tabulated in Table 7.7.

Although the best fit parameters are not too different the best chi-square was obtained from assumption (1). The reduced chi-square for this case is 1.1 and is mainly due to the centroid shifts. For the other cases the reduced chi-square is 1.3. These slightly higher values may be due to some systematic errors which could not be accounted for. For example, the measured shift for line #15 is in fact slightly negative indicating possible underestimation of the quoted values.

So for different cases (a) and (b) have been considered on the basis of the measured intensities and shifts. It is possible to differentiate between the two by analyzing the line width as a function of filter thickness. Because of asymmetry in the line shape the determination of this parameter is not straightforward. The method used was

TABLE 7.7

Sensitivity of Deduced Amplitudes to Different Geometrical Considerations

	Resonance Energies (eV)		χ^2		
	4322	10700	16920		
Simple geometry and Multiple Scattering Included - Normal	0.109 ± .001	0.314 ± .017	-.066 ± .078	.277 ± .024	1.1
Geometry Included - No Multiple Scattering (a)	0.110 ± .001	0.292 ± .016	0.215 ± .021	-.060 ± .081	1.3
Geometry Included - No Multiple Scattering (b)	0.110 ± 0.01	0.313 ± .016	-.089 ± .067	+ .200 ± .031	1.3
Geometry and Multiple Scattering Included (a)	0.109 ± .001	0.323 ± .012	0	+ .228 ± .018	1.3
Geometry and Multiple Scattering Included (b)	0.109 ± .001	0.293 ± .017	0.232 ± .020	-.061 ± .102	1.3

$\chi^2 = \frac{1}{N-p} \sum (y_i - y_t)^2 / \sigma_i^2$ where y_i is a data point, y_t is the corresponding calculated value, N is the no. of data points, p is the no. of parameters in the fit.

to calculate the auto correlation function $C(\tau) = \int y(t)y(t+\tau)dt$ for each filter thickness. This function is symmetric and the measurement of its width is much simpler. The width calculated on this basis and the calculated width using the best fit parameters deduced for the two cases are shown in Table 7.8. Case (a) predicts widths which are much larger than the measured values. That the case (b) parameters predict widths which are in fair agreement with the measured values lends further support to their validity. Using these resonance amplitudes the calculated shifts and intensities are shown in Fig. 7.4 together with the measured data for comparison.

These results, although independent of the chopper data should be able to simulate the ratio $R = \frac{\sigma_{n\gamma}}{\sigma_{n\gamma}}$ derived from the time-of-flight data. When the above parameters were used to calculate R, a good agreement was found. This is shown in Fig. 7.5. Furthermore at the low energy where the sum of the high energy resonances is expected to be constant

$$\left(\text{i.e. } \sum_i \frac{(\Gamma_0 \Gamma_{ij})^2}{E_i} \approx \text{constant} \right)$$

the sum is equal within error to the potential direct capture. This is shown in Table 7.9.

In summary the present experimental data which is sensitive to the low and high energy neutrons show that (1) the correlation between (n,γ) and (d,p) strengths as expected from the predictions of the direct capture

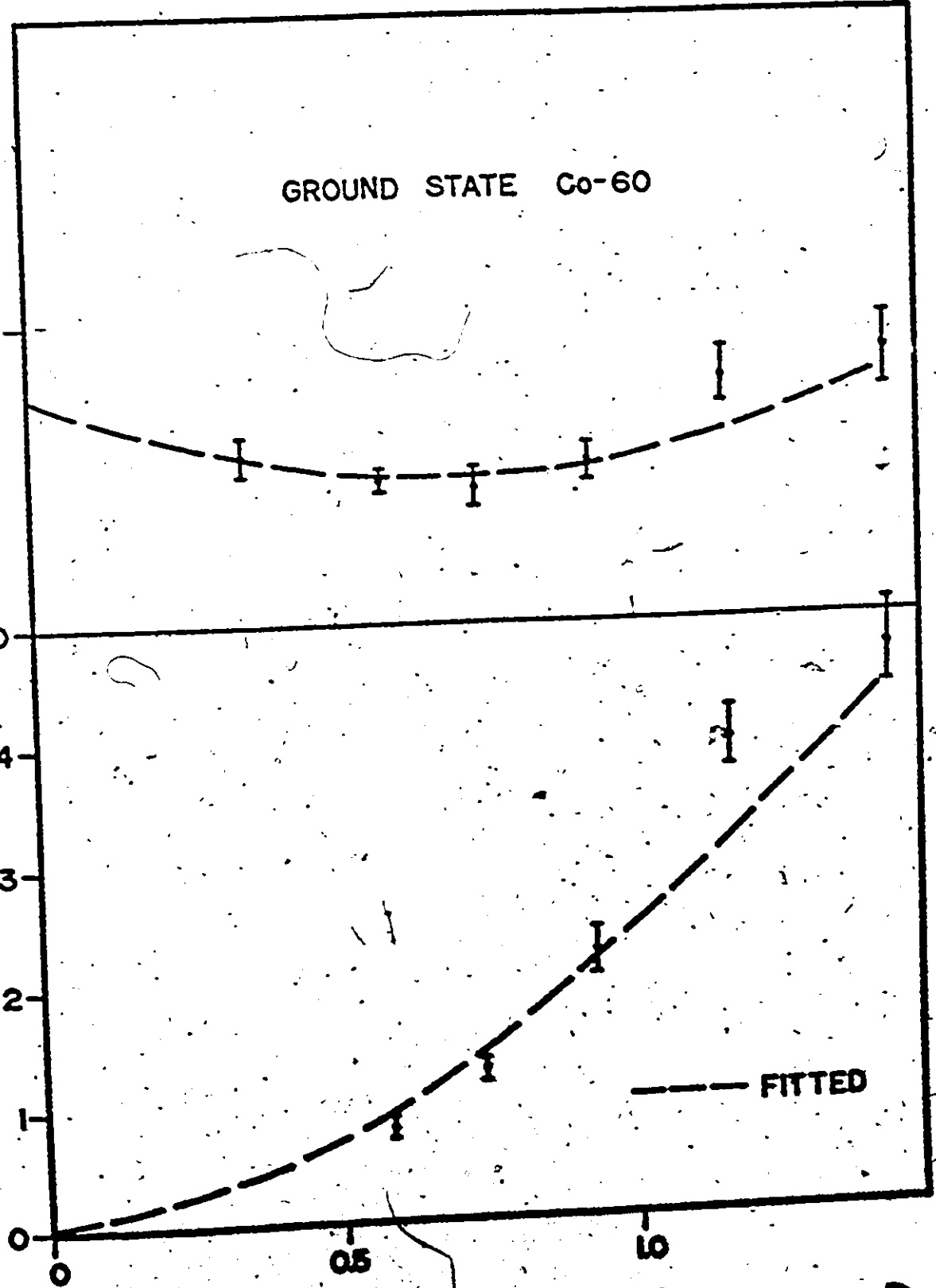
Figure 7.4

Intensity and Centroid Shift - Co^{60} Ground State Line

INTENSITY ($\gamma/10000n$)

GROUND STATE Co-60

PEAK SHIFT (keV)



B² THICKNESS (g/cm²)

--- FITTED

Figure 7.5

Comparison of the ratio $R = \sigma_{nyf} / \sigma_{ny}$ Using the Best Fit
Parameters with the Results of Wasson (Wa 68) and Auchampaugh (Au 68)

5/110

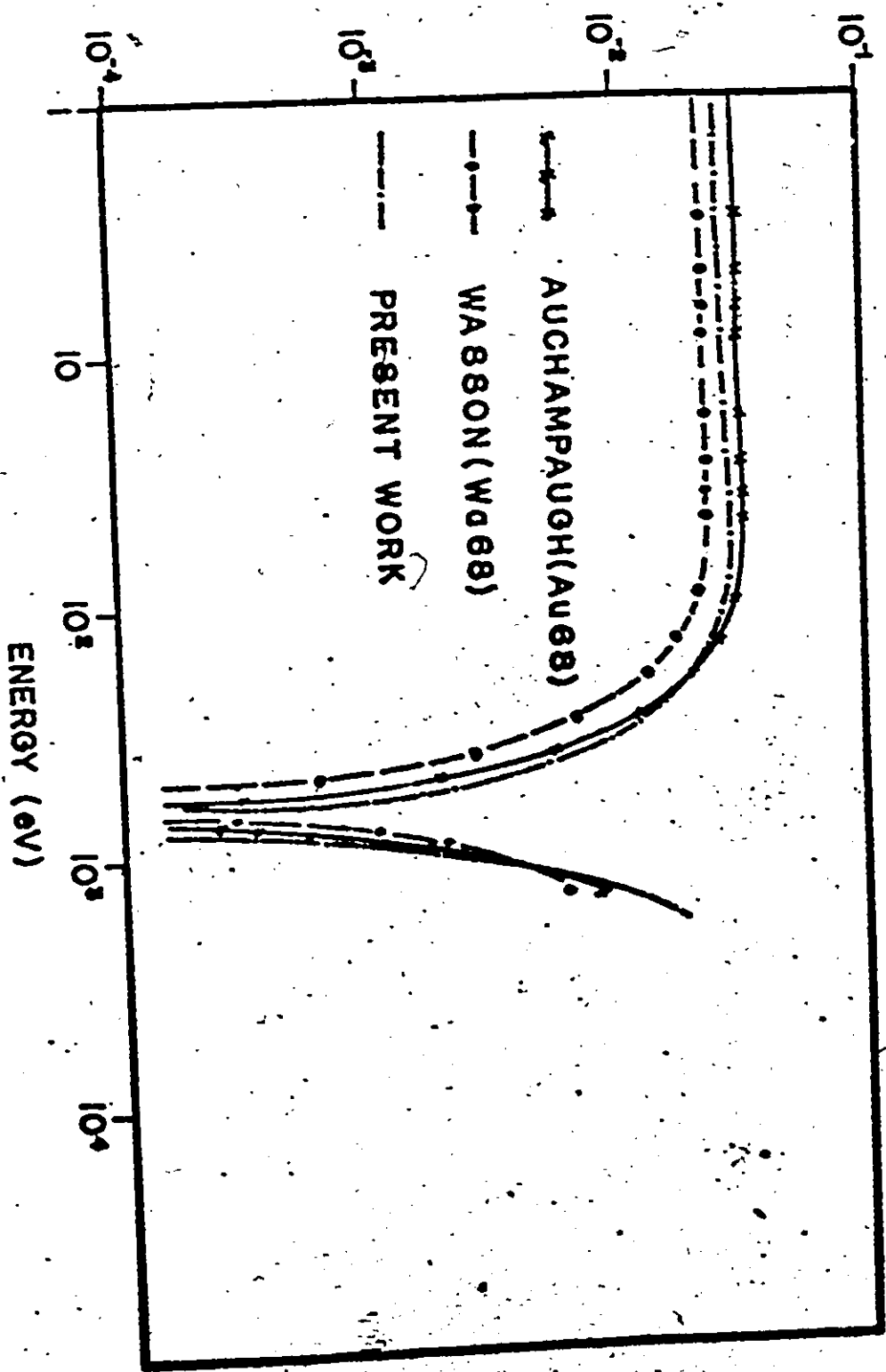


TABLE 7.8

Variation of the Cobalt Ground State Line Widths with
Filter Thickness

Filter Thickness	Increase in Width Relative to 0-Filter		
	Measured (keV)	Case (a) (keV)	Case (b) (keV)
1/8	1.55	2.08	1.60
3/16	1.12	3.06	2.32
1/4	2.83	3.72	2.82
3/8	2.83	4.40	3.30
1/2	4.31	5.01	3.68
5/8	4.05	5.40	3.85

TABLE 7.9

Comparison of the Direct Amplitude with the Contribution
of the High Energy Resonances at 1 eV

Case	A_0	High Energy [*] Resonance Amplitude
Wasson et al (Wa 68)	$1.60 \pm .22 \times 10^{-4}$	-
Auchampaugh (Au 68)	$1.24 \pm .24 \times 10^{-4}$	-
Present Work - Multiple Scattering and Geometry Included (a)	-	$1.00 \pm 0.15 \times 10^{-4}$

$$* \sum_i \frac{\Gamma_0^{1/2} \Gamma_i^{1/2}}{E_i \Gamma_i}$$

High Resonances

model do not exist and (2) no direct capture cross-section or a bound state resonance with $J^\pi = 4^-$ is necessary to explain the cobalt ground state data. The failure of the other investigators to fit their data at low energy with no direct component is due to neglect of the contribution of the higher resonances.

Appendix 1

E1 Transitions in Direct Capture and (d,p) Strengths

1. Fundamental Recoupling Transformation

Consider a state $|j'\rangle$ formed by coupling $|j_1'\rangle$ and $|j_2\rangle$. If $|j_2\rangle$ is inert then a transition through $S^{(k)}$ to a new coupled state $|j\rangle$ formed by coupling $|j_1\rangle$ and $|j_2\rangle$ can be written as (Pa 59).

$$\langle j_1 j_2 j || S^{(k)} || j_1' j_2 j' \rangle = (-)^{j_1 + j_2 + j' + k} \langle j_1 || S^{(k)} || j_1' \rangle \times$$

$$\left[(2j+1)(2j'+1) \right]^{-1/2} \begin{Bmatrix} j & j' & k \\ j_1 & j_1 & j_2 \end{Bmatrix}$$

where $\left\{ \right\}$ is the Wigner 6-j symbol which has the symmetry property

$$\begin{Bmatrix} j & j' & k \\ j_1 & j_1 & j_2 \end{Bmatrix} = \begin{Bmatrix} j_1 & j_1 & k \\ j' & j & j_2 \end{Bmatrix}$$

2. E1 Reduced Matrix Element

The initial state is taken to be an s-wave neutron coupled to the target. $|i\rangle = |j_1 J_t J_i\rangle$ where $J_i = j_1 + J_t$ where $j_1 = 1/2$. The final state is expanded in single particle Neutron states coupled to the target i.e.

$$|f\rangle = \sum_{l_2 j_2} A_{l_2 j_2} |l_2 j_2 J_t J_f\rangle$$

The state $|l_f; j_f J_t J_f\rangle$ is a single particle state $|l_f j_f\rangle$ coupled to give $j_f + J_t = J_f$. Writing the expansion coefficient as $\alpha_{l_f j_f}$, then for a transition E^λ , the reduced matrix element is

$$\begin{aligned} \langle f || E^\lambda || i \rangle &= \sum_{l_f, j_f} \alpha_{l_f j_f} \langle l_f; j_f J_t J_f || E^\lambda || j_i J_t J_f \rangle \\ &= (-)^{j_f + J_t + J_f + \lambda} (2j_f + 1) (2J_f + 1) \times \\ &\quad \sum_{l_f j_f} \alpha_{l_f j_f} \left\{ \begin{matrix} j_f & j_t & \lambda \\ J_f & J_t & J_t \end{matrix} \right\} \langle l_f j_f || E^\lambda || j_i \rangle \end{aligned}$$

3. Single Particle Reduced Matrix Elements

The states $|l s j\rangle$ are formed by $j = l + s$. For inert spin the largest electric moment is

$$\begin{aligned} \langle l_f s j_f || E^\lambda || l_i s j_i \rangle &= (-)^{l_f + s + j_i + \lambda} \sqrt{(2j_f + 1)(2j_i + 1)} \times \\ &\quad \left\{ \begin{matrix} l_f & l_i & \lambda \\ j_i & j_f & s \end{matrix} \right\} \langle l_f || E^\lambda || l_i \rangle \end{aligned}$$

4. Phase Factor

Outside the sum, $(-)^{j_f + J_t + J_f + 2\lambda}$ is not important since it will be squared. Inside the sum, the phase factor is $(-)^{j_f + (l_f + s) + j_i} = (-)^{(l_f + s)} (-)^{j_f + j_i}$.

The j_f, j_i phase factor can be retained in the sum over j and $(-)^{j_f + l_f + s}$ used to keep integral phase.

5. Final Expression

$$\langle f || E^\lambda || i \rangle = \sqrt{(2J_f+1)(2J_r+1)} \sum_{l_f} (-1)^{J_t+l_f+s} \langle l_f || E^\lambda || l_i \rangle \times$$

$$\sum_{j_f} \alpha_{l_f j_f} (-1)^{j_f+j_i} \sqrt{(2J_f+1)(2j_i+1)} \times$$

$$\begin{Bmatrix} l_f & l_i & \lambda \\ j_i & j_f & s \end{Bmatrix} \begin{Bmatrix} j_f & j_i & \lambda \\ J_r & J_f & J_t \end{Bmatrix}$$

6. Reduction for E1 Radiation with $l_i = 0$

$$\langle f || E1 || i \rangle = \sqrt{(2J_f+1)(2J_r+1)} \sum_{l_f} (-1)^{J_t+l_f+s} \langle l_f || E1 || 0 \rangle \times$$

$$\sqrt{2j_i+1} \sum_{j_f} \alpha_{l_f j_f} (-1)^{j_f+j_i} \sqrt{2j_f+1} \times$$

$$\begin{Bmatrix} l_f & 0 & 1 \\ j_i & j_f & s \end{Bmatrix} \begin{Bmatrix} j_f & j_i & 1 \\ J_r & J_f & J_t \end{Bmatrix}$$

$$\langle l_f || E1 || 0 \rangle = \langle p || E1 || s \rangle \delta_{l_f,1} j_i = 1/2$$

$$\langle f || E1 || i \rangle = \sqrt{2(2J_f+1)(2J_r+1)} (-1)^{J_t+3/2} \langle p || E1 || s \rangle \times$$

$$\sum_{j_f} \alpha_{l_f j_f} (-1)^{j_f+1/2} \sqrt{2j_f+1} \begin{Bmatrix} 1 & 0 & 1 \\ j_i & j_f & s \end{Bmatrix} \begin{Bmatrix} j_f & j_i & 1 \\ J_r & J_f & J_t \end{Bmatrix}$$

Using the relationship

$$\begin{Bmatrix} j_1 & j_2 & j_3 \\ 0 & j_3 & j_2 \end{Bmatrix} = (-)^{j_1+j_2+j_3} \left[(2j_2+1)(2j_3+1) \right]^{-\frac{1}{2}} \quad \text{then}$$

$$\langle f || E1 || i \rangle = \sqrt{\frac{2(2J_f+1)(2J_r+1)}{3}} (-)^{J_r+3/2} \langle p || E1 || s \rangle \quad \times$$

$$\sum_{J_f} a_{1j_f} (-)^{j_f+k} \begin{Bmatrix} j_f & k & 1 \\ J_r & J_f & J_t \end{Bmatrix} \sqrt{2j_f+1}$$

$$\langle f || E1 || i \rangle^2 = 2/3 (2J_f+1)(2J_r+1) \langle p || E1 || s \rangle^2 \quad \times$$

$$\left[\begin{Bmatrix} 3/2 & 1/2 & 1 \\ 2 & & \\ J_r & J_f & J_t \end{Bmatrix} a_{1, 3/2} - \sqrt{2} \begin{Bmatrix} k & k & 1 \\ J_r & J_f & J_t \end{Bmatrix} a_{1, k} \right]$$

where $a_{1j} = \langle J_f | 1; j J_t J_f \rangle$ is the overlap between an $l = 1, j = 1 + s$ neutron coupled to the target and the final state

7. Reduced Transition Probability

$$\langle j' m' | T_q^{(k)} | j m \rangle = (-)^{j'-m'} \begin{Bmatrix} j' & k & j \\ -m' & q & m \end{Bmatrix} \langle j' || T^{(k)} || j \rangle$$

$$\sum_{\substack{m, m' \\ q}} \langle j' m' | T_q^{(k)} | j m \rangle^2 = \langle j' || T^{(k)} || j \rangle^2 \sum_{\substack{m, m' \\ q}} \left[(-)^{j'-m'} \begin{Bmatrix} j' & k & j \\ -m' & q & m \end{Bmatrix} \right]^2$$

$$\sum_{\substack{m' q \\ m}} \begin{Bmatrix} j' & k & j \\ -m' & q & m \end{Bmatrix}^2 = \frac{1}{2j+1} \sum_{\substack{m' \\ q}} = \langle j' || T^{(k)} || j \rangle^2$$

$$B(E1) = \frac{1}{2J_f + 1} \sum_{M_f \lambda M_i} \langle J_f M_f | E_\lambda^{(1)} | J_i M_i \rangle = \frac{\langle J_f || E1 || J_i \rangle^2}{2J_f + 1}$$

8. Partial Radiative Cross-Section

$\sigma_{nyf} = \pi \lambda^2 g_J \frac{\Gamma_n \Gamma_{yf}}{(E - E_n)^2 + \frac{\Gamma^2}{4}}$. The resonance area is given

by $A_f = 4\pi \lambda^2 g_{J_f} \frac{\Gamma_n}{\Gamma} \Gamma_{yf}$ where $\Gamma_{yf} = \frac{16h^2}{9} k^3 B(E1)$; $g_{J_f} = \frac{2J_f + 1}{2(2J_t + 1)}$

$$\sigma_{nyf} = \left(\frac{64 \pi^2}{9}\right) \left(\frac{k}{k^2}\right)^3 \frac{1}{2(2J_t + 1)} \left(\frac{\Gamma_n}{\Gamma}\right) \langle J_f || E^{(1)} || J_i \rangle^2$$

where the $2J_f + 1$ factor has been taken out of the statistical factor.

Let $\lambda_f = \frac{\Gamma_n}{\Gamma}$ without initial statistical factor of $2J_f + 1$, then

$$\sigma_{nyf} = \lambda_f (2J_f + 1) (2J_t + 1) \left[2 \begin{Bmatrix} 3/2 & 1/2 & 1 \\ J_f & J_f & J_t \end{Bmatrix} \right]^{6_{3/2}}$$

$$\sqrt{2} \begin{Bmatrix} 3/2 & 1/2 & 1 \\ J_f & J_f & J_t \end{Bmatrix} S_3 \text{ where}$$

$$S_3 = \langle J_f || 1 || J_t J_f \rangle$$

For cobalt $\lambda_3 = \lambda_4$ when the ratio of the fractional contributions is 7/9.

APPENDIX 2Correction for Multiple Collision using Response

Consider an initial spectrum $A_0 \delta(E_0 - E)$. The result of scattering is then given by

$$R(E_0, E) = \sum_{n=0}^{\infty} F^n A_0 \delta(E_n - E) = \sum_{n=0}^{\infty} A_n \delta(E_n - E) \quad (1)$$

where F is the probability of scattering and E_n is the resulting energy following the n^{th} scattering. Thus $E_n = E_0 (1-C)^n$ where $C = \Delta E/E_0$ and ΔE is the energy loss after the collision.

From the above equations we derived the following relationships

$$\ln A_n = \ln A_0 + n \ln F \quad (2)$$

$$\ln E_n = \ln E_0 + n \ln (1-C) \quad (3)$$

Hence

$$n = \frac{1}{\ln(1-C)} \ln \left(\frac{E_n}{E_0} \right)$$

Substituting this in Eq. (2)

$$\ln A_n = \ln A_0 + \frac{\ln F}{\ln(1-C)} \ln \frac{E_n}{E_0}$$

$$\ln A_n = \ln A_0 + \gamma \ln \frac{E_n}{E_0} \text{ where } \gamma = \frac{\ln F}{\ln(1-C)}$$

$$A(E) = A_0 \left(\frac{E}{E_0} \right)^{\gamma} \quad (4)$$

$$R(E_0, E) = A_0 \left(\frac{E}{E_0}\right)^\gamma / \int_0^{E_0} A_0 \left(\frac{E}{E_0}\right)^\gamma dE \quad (5)$$

$$= \frac{(\gamma+1)}{E_0} \left(\frac{E}{E_0}\right)^\gamma \quad \text{for } 0 < E < E_0$$

$$= 0 \quad \text{for } E > E_0$$

Appendix 3Dependence of Error in CentroidCalculation on Resolution and Background Spectrum

Let $N(X)$ = total counts in channel X

$P(X)$ = actual peak height in channel X

$B(X)$ = background contribution in channel X

$$N(X) = P(X) + B(X)$$

$$\langle X \rangle = \frac{\int X[N(X) - B(X)] dx}{\int [N(X) - B(X)] dx} = \frac{C}{A} \quad (1)$$

By the propagation of errors method

$$\sigma_{\langle X \rangle}^2 = \frac{\sigma_C^2}{A^2} + \frac{C^2 \sigma_A^2}{A^4} = \frac{\sigma_C^2}{A^2} + \langle X \rangle^2 \frac{\sigma_A^2}{A^2} \quad \text{from (1)}$$

Substituting $\sigma_A^2 = A$

$$\sigma_{\langle X \rangle}^2 = \frac{\sigma_C^2}{A^2} + \frac{\langle X \rangle^2}{A}$$

Assume $P(X) = P_0 e^{-X^2/2\sigma^2}$ so that $\langle X \rangle = 0$. Then $\sigma_{\langle X \rangle}^2 = \frac{\sigma_C^2}{A^2}$

Consider the expression for C .

$$C = \int X[N(X) - B(X)] dx$$

$$\sigma_C^2 = \int X^2 [\sigma_A^2 + \sigma_B^2] dx$$

$$\text{But } \sigma_n^2 = \sigma_p^2 + \sigma_B^2$$

$$\sigma_c^2 = \int x^2 \left[\sigma_p^2 + 2\sigma_B^2 \right] dx$$

$$\text{Since } \sigma_p^2 = P(x) = P_0 e^{-x^2/2\sigma^2}$$

$$\sigma_c^2 = \int x^2 P_0 e^{-x^2/2\sigma^2} dx + 2 \int x^2 B(x) dx$$

Physically the Gaussian peak limits can be taken from $-\infty$ to $+\infty$ because its contribution should approach 0 after a few σ . However, the background contribution should be over the width of the peak only. Hence

$$\sigma_c^2 = P_0 \sigma \sqrt{2\pi} \sigma^2 + 2 \int x^2 B(x) dx$$

$$\langle x^2 \rangle = \frac{\sigma_c^2}{A^2} = \frac{\sigma^2}{A} + \frac{2 \int x^2 B(x) dx}{A^2}$$

If $B(x) = B_0 = \text{constant}$, then

$$\langle x^2 \rangle = \frac{\sigma^2}{A} \left[1 + \frac{36 B_0 \sigma}{A} \right]$$

Appendix 4

Effective Degree of Freedom

Consider neutron captures in some initial states $\{|i\rangle\}$ which result in radiative transitions to a final state $|j\rangle$. Then according to the compound nucleus theory, the distribution of the reduced intensities $\{I_{ij}\}$ would follow a Porter-Thomas fluctuation, where I_{ij} is the intensity of a gamma ray emission from an initial state $|i\rangle$ to the final state $|j\rangle$. In the case of resonance capture experiments where the initial states may be well-defined by considering particular neutron energies a plot of the $\{I_{ij}\}$ would show a chi-square distribution with one degree of freedom. For the B^{10} filter experiments done in this research, the strength of the transition to any given final state would be the sum of contributions from several initial states. Therefore the distribution of intensities to different final states would be a chi-square distribution with an effective degree of freedom greater than one.

Let $I_{\cdot j}$ be the transition strength to a final state $|j\rangle$ following neutron radiative capture in several initial states $\{|i\rangle\}$. Then for a particular B^{10} filter

$$I_{\rightarrow j} = \frac{\int_E C_n(E) \frac{\sigma_{\rightarrow j}(E)}{\sigma_T(E)} dE}{\int_E C_n(E) \frac{\sigma_Y(E)}{\sigma_T(E)} dE}$$

where $\sigma_{\rightarrow j}(E)$ is the

capture cross-section from all contributing resonances.

Ignoring interference terms $\sigma_{\rightarrow j}(E)$ and substituting the expressions

$$\sigma_{Yij}(E) = \pi k^2 g(s) \frac{\Gamma_{ni} \Gamma_{Yij}}{(E-E_i)^2 + \Gamma_i^2/4}$$

$$\sigma_{Yi}(E) = \pi k^2 g(s) \frac{\Gamma_{ni} \Gamma_{Yi}}{(E-E_i)^2 + \Gamma_i^2/4}$$

$$\frac{\Gamma_{Yij}}{\Gamma_i} = \frac{\sigma_{Yij}}{\sigma_{Yi}} \quad I_{ij} \text{ the above equation}$$

reduces to $I_{\rightarrow j} = \sum_i f_i I_{ij}$ where

$$f_i = \frac{\int C_n(E) \frac{\sigma_{Yi}(E)}{\sigma_Y(E)} dE}{\int C_n(E) \frac{\sigma_Y(E)}{\sigma_Y(E)} dE}$$

Hence f_i is the total fractional contribution of each contributing initial state. The variance of $I_{\rightarrow j}$ is approximated by $\sigma_{I_{\rightarrow j}}^2 = \sum f_i^2 \sigma_{I_{ij}}^2$. In analogy to the Porter-Thomas distribution for I_{ij} , define an effective degree of freedom such that

$$\frac{\sigma_{I_{\rightarrow j}}^2}{\langle I_{\rightarrow j} \rangle^2} = \frac{1}{\nu_{eff}} \text{ then we have}$$

$$\begin{aligned} \frac{2}{v_{\text{eff}}} &= \frac{1}{\langle I \rightarrow j \rangle} \sum_i f_i^2 \quad 2\langle I_{ij} \rangle \\ &= \frac{1}{\sum_i f_i} 2 \sum_i f_i^2 = 2 \sum_i f_i^2 \quad \text{since } \sum_i f_i = 1 \\ v_{\text{eff}} &= \left[\sum_i f_i^2 \right]^{-1} \end{aligned}$$

For s-wave capture, the initial states have two spin states namely $I \pm \frac{1}{2}$ where I is the target spin. For clarity consider the cobalt case. The target spin is $I^\pi = 7/2^-$. Hence the possible capture states for s-wave neutrons are $J_i^\pi = 3^-, 4^-$. For dipole transitions the final states can have spins of $2^+, 3^+, 4^+, 5^+$. Therefore in general, the overall intensity is a composite of four possible distributions corresponding to transitions to the four possible final states.

Let $P_i(X)$ represent any one of the possible distributions. Then because of the spin dependence of the level density the overall intensity distribution $P_T(X)$ must be a weighted error of all the possible distributions. Hence

$$P_T(X) = \sum_{f=2}^{4^+} w_f P_f(X)$$

where

$$w_f = \frac{(2J_f+1)e^{-J_f(J_f+1)/2\sigma^2}}{\sum_f (2J_f+1)e^{-J_f(J_f+1)/2\sigma^2}}$$

and σ is the spin cut-off parameter. It has been shown (Gi 65) that for intermediate nuclei such as cobalt and manganese, $\sigma = 3.5$.

The overall average intensity is then $\langle X_T \rangle = \int X P_T(X) dx = \sum_4 w_f \langle X_f \rangle$ where $\langle X_f \rangle$ is the average intensity corresponding to distribution f .

Because of the dipole selection rule the average intensity of transitions to the different spin states will vary. Let f_3 be the overall fractional contribution of 3^- capture states and f_4 that of 4^- capture states. Then we may assume that the average intensity of transitions to 2^+ states will be approximately proportional to f_3 and that to 5^+ states f_4 . Furthermore since both capture states can populate final states with spins 3^+ and 4^+ , then the average intensity of transitions to these states will be proportional to $f_3 + f_4 = 1$. These imply the following relationships between the average intensities:

$$\langle X_2 \rangle = f_3 \langle X_3 \rangle, \langle X_3 \rangle = \langle X_4 \rangle, \langle X_5 \rangle = f_4 \langle X_4 \rangle$$

Substituting these equations in the expression for the average overall intensity we have

$$\langle X_T \rangle = (w_2 f_3 + w_3 + w_4 + w_5 f_4) \langle X_3 \rangle = \frac{1}{g} \langle X_3 \rangle \text{ where } g = w_2 f_3 + w_3 + w_4 + w_5 f_4$$

The variance of the overall distribution is

$$\begin{aligned} \sigma_T^2 &= \int (X - \langle X_T \rangle)^2 P_T(X) dx = \int X^2 P_T(X) dx - \langle X_T \rangle^2 \\ &= \sum_f w_f \int X^2 P_f(X) dx - \langle X_T \rangle^2 \\ &= \sum_f w_f \left(\int X^2 P_f(X) dx - \langle X_f \rangle^2 \right) + \langle X_T \rangle^2 \\ &= \sum_f w_f \sigma_f^2 + \langle X_T \rangle^2 \end{aligned}$$

If we now make the assumption that each individual distribution $P_f(X)$ is a chi-square distribution with ν degrees of freedom then $\sigma^2 / \langle X \rangle^2 = 2/\nu$. Furthermore since $\sigma^2 = \langle X^2 \rangle - \langle X \rangle^2$ we deduce that $\langle X_f^2 \rangle = (2/\nu_f + 1) \langle X_f \rangle^2$. The expression for σ_T^2 can therefore be rewritten as

$$\begin{aligned} \sigma_T^2 &= \sum_f w_f (2/\nu_f + 1) \langle X_f \rangle^2 - \langle X_T \rangle^2 \\ &= \left[w_2 (2/\nu_2 + 1) f_3^2 g^2 + w_3 (2/\nu_3 + 1) g^2 + w_4 (2/\nu_4 + 1) g^2 \right. \\ &\quad \left. + w_5 (2/\nu_5 + 1) f_4^2 g^2 - 1 \right] \langle X_T \rangle^2 \end{aligned}$$

Finally $\frac{\sigma_T^2}{\langle X_T \rangle^2} = \left[w_2 (2/\nu_2 + 1) f_3^2 g^2 + w_3 (2/\nu_3 + 1) g^2 + w_4 (2/\nu_4 + 1) g^2 + w_5 (2/\nu_5 + 1) f_4^2 g^2 - 1 \right]$

In analogy with the chi-square distribution we may define an effective degree of freedom expressed in terms of the overall variance and average intensity. Then

$$\frac{\sigma_T^2}{\langle X_T \rangle^2} = \frac{2}{\nu_{\text{eff}}}$$

From the previous equation we then have

$$\begin{aligned} \nu_{\text{eff}} &= 2 \left[w_2 (2/\nu_2 + 1) f_3^2 g^2 + w_3 (2/\nu_3 + 1) g^2 \right. \\ &\quad \left. + w_4 (2/\nu_4 + 1) g^2 + w_5 (2/\nu_5 + 1) f_4^2 g^2 - 1 \right]^{-1}. \end{aligned}$$

To compare the above results with the experimental data Wilets formula (Ly 69) is used. This is expressed as

$$(\nu_{\text{eff}})_{\text{WLT}} = \frac{2\langle I \rangle^2}{\langle I^2 \rangle - \langle I \rangle^2}$$

where I is a primary gamma ray reduced intensity.

REFERENCES

- As 71 Assche, P. H. M., et al, Nucl. Phys. A160 (1971) 367.
- Au 68 Auchampaugh, G. F., Ph.D. Thesis, 1968, University of California.
- Ba 53 Bartholomew, G. A., Kinsey, B. B., Phys. Rev. 89 (1953) 386.
- Be 35 Bethe, H. A., Phys. Rev. 47 (1935) 747.
- Be 62 Bergvist, I., Starfelt, N., Nucl. Phys. 39 (1962) 529.
- Bl 52 Blatt, J. M., Weiskopf, V. F., Theoretical Nuclear Physics, (1952), Wiley, New York.
- Bl 65 Blair, A. G., Armstrong, D. D., Phys. Rev. 140 (1965) B1567.
- Bn 66 BNL 325, Brookhaven National Laboratory, Neutron Cross-Section, 11A (1966).
- Bo 36 Bohr, N., Nature, Lond. 137 (1936) 344.
- Bo 59 Bockelman, C. K., Nucl. Phys. 13 (1959) 205.
- Ca 62 Carpenter, T. R., ANL 6589 (1962).
- Ch 61 Childs, W. J., Goodman, L. S., Kieffer, L. J., Phys. Rev. 122 (1961) 891.
- Co 62 Cohen, B. L., Fulmer, R. H., McCarthy, A. L., Phys. Rev. 126 (1962) 698.
- Co 64 Cohen, B. L., Fulmer, R. H., McCarthy, A. L., Phys. Rev. 133 (1964) B955.
- Co 64a Cote, R. E., Bollinger, L. M., Thomas, G. E., Phys. Rev. 134 (1964) B1047.
- Co 68 Comfort, J. R., Phys. Rev. Lett. 20 (1968) 941.
- Co 68a Comfort, J. R., Ph.D. Thesis (1968) Yale University, U.S.A.
- Da 61 Dalton, A. W., Parry, G., Scott, H. D., Swierszczewski, Proc. Phys. Soc. 78 (1961) 404.

- Do 56 Dobrowolski, W., Jones, R. V., ~~Jeffries~~, C. D.,
Phys. Rev. 101 (1956) 1001.
- En 60 Enge, H. A., Jarrell, D. L., Angleman, C. C.,
Phys. Rev. 119 (1960) 737.
- En 66 Enge, H. A., Introduction to Nuclear Physics, (1966)
Addison-Wesley, Reading, Mass., U.S.A.
- Fa 59 Fano U., Racah G., Academic Press Inc., N. Y.
(1959) 84.
- Fa 65 Fairsten, E., Hahn, J., Nuclear Pulse Amplifier -
Fundamentals & Design Practice (1965), Tennaec,
Inc., U. A. A.
- Pi 63 Fisk, G. W. K., Lynn, J. E., Moxon, M. C., Proc.
Phys. Soc. 82 (1963) 477.
- Gi 65 Gilbert, A., Chen, F. S., Cameron, A. G. W., CJP
43 (1965) 1248.
- Gr 58a Groshev L. V., Demidov, A. M., Lutsenko, V. N.,
Pelekhov, V. I., Soviet J. At. Energy 8 (1958)
127.
- Gr 58 Groshev, L. V., Demidov, A. M., Lutsenko, V. N.,
Pelekhov, V. I., J. Nucl. Energ. 8 (1958) 127.
- Hu 66 Hughes, L. B., Kennett, T. J., Prestwich, W. V.,
Nucl. Phys. 80 (1966) 131.
- Hu 67 Hughes, L. B., Ph.D. Thesis, (1967) McMaster Univ-
ersity, Hamilton, Ontario.
- Ia 70 IAEA Technical Report Series #107, (1970) Vienna.
- Ke 58 Kennett, T. J., Bollinger, L. M., Carpenter, R. T.,
Phys. Rev. Lett. 1 (1958) 77.
- Ke 72 Kallater, H., Bachner, D., Schmidt, D., Seliger,
W., Nucl. Phys. A183 (1972) 509.
- Ki 54 Kinsey, B. B., Bartholomew, G. A., Phys. Rev.
93 (1954) 1260.
- Kr 55 Krothov, R., CJP 33 (1955) 622.
- La 60 Lane, J. M., Lynn, J. E., Nucl. Phys. 17 (1960) 563.
- Lu 65 Luthy, R., Starfelt, N. Nucl. Phys. 67 (1965)
221.

- Ly 68 Lynn, J. E., The Theory of Neutron Resonance Reactions, Oxford University Press (1968).
- Ly 69 Lycklama, H., Kennett, T. J., Hughes, L. B., CJP 47 (1969) 665.
- Ma 68 Marion, J. B., Nucl. Data A4 (1968) 301.
- Ma 69 Malmstadt, H. V., Enke, G. G., Digital Electronics for Scientist, Benjamin, W. A., Inc. (1969).
- Me 69 Mellema, J. Postma, H., Nucl. Phys. A130 (1969) 161.
- Me 70 Mallama, J., Postma, H., Nucl. Phys. A154 (1970) 385
- Mo 36 Moon, P. B., Tillman, R., Proc. R. Soc. 153 (1936) 421.
- Ni 70 Nichol, L., Lopez, A. M., Robertson, A., Prestwich, W. V., Kennett, T. J., Nucl. Inst. & Method 81 (1970) 263.
- Po 56 Porter, C. E., Thomas, R. G., Phys. Rev. 104 (1956) 483.
- Po 62 Powell, M. J. D., Computer Journal 5 (1962) 147.
- Pr 62 Preston, M. A., Physics of the Nucleus (1962) Addison-Wesley.
- Pr 66 Prestwich, W. V., Kennett, T. J., Hughes, L. B., Nucl. Phys. 88 (1966) 548.
- Pr 67 Prestwich, W. V., Cote, R. E., Phys. Rev. 155 (1967) 1223.
- Ra 36 Rasetti, F., Segre, E., Firk, G., Dunning, G. R., Fegran, G. B., Phys. Rev. 49 (1936) 104.
- Ra 67 Rasmussen, N. C., Orphan, V. J., Hukai, Y., Inouye, T., Nucl. Data A3 (1967) 490.
- Ro 71 Robertson, R. G. H., Ph.D. Thesis (1971) McMaster University, Hamilton, Ontario.
- Ro 72 Robertson, A., Prestwich, W. V., Kennett, T. J., Nucl. Inst. & Method 60 (1972) 317.

- Se 71 Seliger, W., Bachner, D., Kelleter, H., Schmidt, B., Nucl. Phys. A184 (1971) 599.
- Sh 56 Shutko, A. V., Zaretskii, D. P., Soviet Physics, JETP 2 (1956) 769.
- Sh 66 Shera, E. B., Kafmeister, D. W., Phys. Rev. 150 (1966) 894.
- St 68 Strauss, M. G., Sifter, L. V., Lenkszres, F. R., Brenner, R., 11th Scintillation & Semi-conductor Symposium (1968).
- St. 72 Stecher-Rasmussen, F., Abrahams, K., Kopecky, J., Nucl. Phys. A181 (1972) 241.
- Ta 73 Taylor, T., (1973) Private Communication, McMaster University, Hamilton, Ont.
- Vo 58 Vogt, E., Phys. Rev. 112 (1958) 203.
- Wa 64 Wasson, O. A., Wetzel, K. J., Bockelman, C. K., Phys. Rev. 136 (1964) B1640.
- Wa 65 Wasson, O. A., Draper, J. E., Nucl. Phys. 73 (1965) 499.
- Wa 66 Wasson, O. A., Bhat, M., R., Chrien, R. E., Lone, M. A., Beer, M., Phys. Rev. Lett-17 (1966) 1220.
- Wa 68 Wasson, O. A., Chrien, R. E., Bhat, M. R., Lone, M. A., Beer, M., Phys. Rev. 176 (1968) 1314.